

**I. A VACUUM X-RAY DIFFRACTOMETER FOR
HIGH TEMPERATURE STUDIES**

**II. AN INVESTIGATION OF THE ALLOTROPIC
TRANSFORMATION OF TITANIUM**

Thesis by

Ronald H. Willens

In Partial Fulfillment of the Requirements
For the Degree of
Doctor of Philosophy

California Institute of Technology
Pasadena, California
1961

ACKNOWLEDGMENTS

The author wishes to express his gratitude to Professor Pol Duwez for the advice and encouragement given to him during this investigation and to Professor Francis Buffington for his many helpful suggestions. The author also wishes to thank Professor Jesse DuMond whose advice simplified many of the design aspects of the x-ray diffractometer. He also acknowledges the assistance of Messrs. W. Klement, D. Saund, R. Curtis, M. Krone, C. Yates, M. Malcolm, F. Linton, R. Harrington, J. Marin and F. Youngkin for their contributions to the design, construction and assembly of the instrument and Mr. R. Bloom for preparing most of the tracings. Thanks are also given the Central Shop Facilities where most of the parts were machined. The author is grateful to the Office of Scientific Research and the United States Steel Foundation for their financial support.

ABSTRACT

A vacuum high temperature x-ray diffractometer has been designed and constructed to study metals, sensitive to oxygen and nitrogen contamination, up to 1200°C . The factors which affect the accuracy of the diffractometer method and the proper choice of extrapolation functions are discussed. It is shown that this instrument can determine lattice parameters with an accuracy of one part in forty thousand. The thermal expansion of titanium has been investigated to 650°C and the c/a parameter is found to increase rapidly above 400°C . This variation of c/a is correlated with other properties of titanium to formulate a band model. On the basis of this model it is shown that the electrons can give an appreciable positive contribution to the free energy as the transformation temperature is approached and it is proposed that this is the main factor causing the instability of the low temperature modification of titanium.

TABLE OF CONTENTS

<u>CHAPTER</u>	<u>TITLE</u>	<u>PAGE</u>
1.	Introduction	1
	PART I. A Vacuum X-ray Diffractometer for High Temperature Studies	4
2.	Design and Construction of High Temperature X-ray Diffractometer	5
	2.1 The Vacuum System and Its Associated Electronics	8
	2.2 The Diffractometer	11
	2.3 The Monochromator	19
	2.4 The Goniometer	31
	2.5 The Drive	42
3.	Evaluation of Errors Limiting the Accuracy of the Diffractometer	48
4.	Extrapolation Functions for the Diffractometer Method	66
5.	Experimental Procedure and Results	84
	PART II. An Investigation of the Allotropic Transformation of Titanium	91
6.	Discussion	92
7.	Conclusions	119
	References	120
	Appendix Worm Gear Calibration	126

1. INTRODUCTION

Prior to the utilization of high temperature x-ray diffraction techniques, the procedures for determining the high temperature state of a material consisted of thermal analysis, metallographic examination after quenching and measurement of electrical, magnetic, optical, mechanical and thermal properties. These measurements gave no direct crystallographic information and many times led to erroneous results. The first application of high temperature x-ray diffraction was made by Westgren⁽¹⁾ in 1921. Westgren made the astounding discovery that α and β iron are isomorphic and the $\alpha \rightarrow \gamma$ transformation is a change from body-centered cubic to face-centered cubic. Westgren's high temperature x-ray diffraction camera⁽²⁾ consisted of a wire specimen located along the axis of a cylindrical water cooled camera. The camera was filled with hydrogen and the wire specimen was heated by an electric current. The x-ray diffraction pattern was recorded by a film placed around the camera.

Since Westgren's experiment, the use of high temperature x-ray diffraction has grown to encompass many metallurgical and solid state problems such as phase equilibria, allotropy, order-disorder phenomena, kinetics of solid state changes, thermal expansion and thermal diffuse scattering with its application to nuclear motion and elastic constants. There have been numerous designs of high temperature x-ray cameras to study these problems. Basically these cameras can be classified into five different categories of design -- the Debye-

Scherrer type⁽³⁻²⁴⁾, the Seemann-Bohlin type⁽²⁵⁾, the flat-plate type⁽²⁶⁾, the single crystal type⁽²⁷⁻²⁹⁾, and the counter-diffractometer type⁽³⁰⁻³⁷⁾. The first four types of x-ray cameras usually have used film for a detector which makes detection and interpretation of transient phases very difficult. Lattice parameters that continually change during a transformation appear as broad lines on the film which can erroneously be interpreted as strain broadening. The radiation counter technique is not subject to these objections but there is the possibility that the radiation counter is not on a diffraction peak of a transient phase and will never detect its existence.

The specimen in a Debye-Scherrer camera is usually in powder or wire form. If it is a powder, it must have an auxiliary support such as a quartz tube or fiber which can cause contamination of the specimen at high temperatures. A wire can be supported outside of the hot zone of the camera, but this leads to thermal gradients in the wire. There are other problems associated with temperature measurement, orientation, texture and grain size in this type of camera. Usually, to avoid spottiness of the diffraction patterns, the specimen is required to rotate and to oscillate vertically.

Many of the disadvantages of the Debye-Scherrer type of camera are eliminated by the Seemann-Bohlin camera. In cameras of this design the specimen can be fairly large and supported in the hot zone of the camera and temperature measurements can be facilitated with thermocouples attached to the specimen. However, there is the disadvantage that a complete x-ray diffraction pattern cannot be obtained

on a single exposure.

Single crystal cameras have all the deficiencies of the Debye-Scherrer type camera at high temperatures; however, some studies require the use of a single crystal.

In recent years the counter-diffractometer has come into prominence and has been adapted to both high and low temperatures. This method combines both the advantages of high precision and rapid detection of transforming phases. The procedure for measuring the intensity of diffraction peaks has simplified kinetics studies. The first part of this thesis is concerned with the design and construction of this type of instrument.

The application of this instrument to measure the thermal expansion of titanium is presented next. Prior attempts^(38, 39) to measure this property have not been satisfactory due to contamination of the sample by oxygen and nitrogen at elevated temperatures. The purpose for determining the thermal expansion coefficients is to further understand the allotropic behavior of titanium, for an anomalous behavior of these coefficients can be interpreted in terms of a change in the electronic binding.

PART I

**A VACUUM X-RAY DIFFRACTOMETER
FOR HIGH TEMPERATURE STUDIES**

2. DESIGN AND CONSTRUCTION OF HIGH TEMPERATURE X-RAY DIFFRACTOMETER

Precision x-ray diffraction studies at elevated temperatures are hampered by three main factors - specimen contamination, thermal diffuse scattering and excessive grain growth. Metals such as titanium, zirconium and hafnium cannot be heated in an ordinary dynamically evacuated vacuum system, in which the pressure is of the order of 10^{-6} mm, without rapid deterioration of the specimen surface by oxygen and nitrogen. The specimen also may be heated in a highly purified gas; however, considerably more power is required because of convection losses and the subsequent transfer of heat to other parts of the x-ray camera causes expansion which can reduce the accuracy of most x-ray cameras. The thermal diffuse scattering of the x-rays and the decrease of the intensity of diffraction peaks as the specimen is heated could result in the complete loss of the important back-reflection peaks in the background. The grain growth at elevated temperatures prevents the statistical averaging necessary for a powder x-ray diffraction technique. A single crystal method cannot be used in many metallurgical investigations because, even if a single crystal could be obtained, it would become polycrystalline when any transformation occurred.

With these factors in mind a high temperature, high vacuum x-ray diffractometer was designed and constructed. Figure 1 shows a general view of the apparatus. Figure 2 is a schematic view of the instrument and its associated electronics. For the purpose of discussion it is



Figure 1. The high temperature x-ray diffractometer installation.

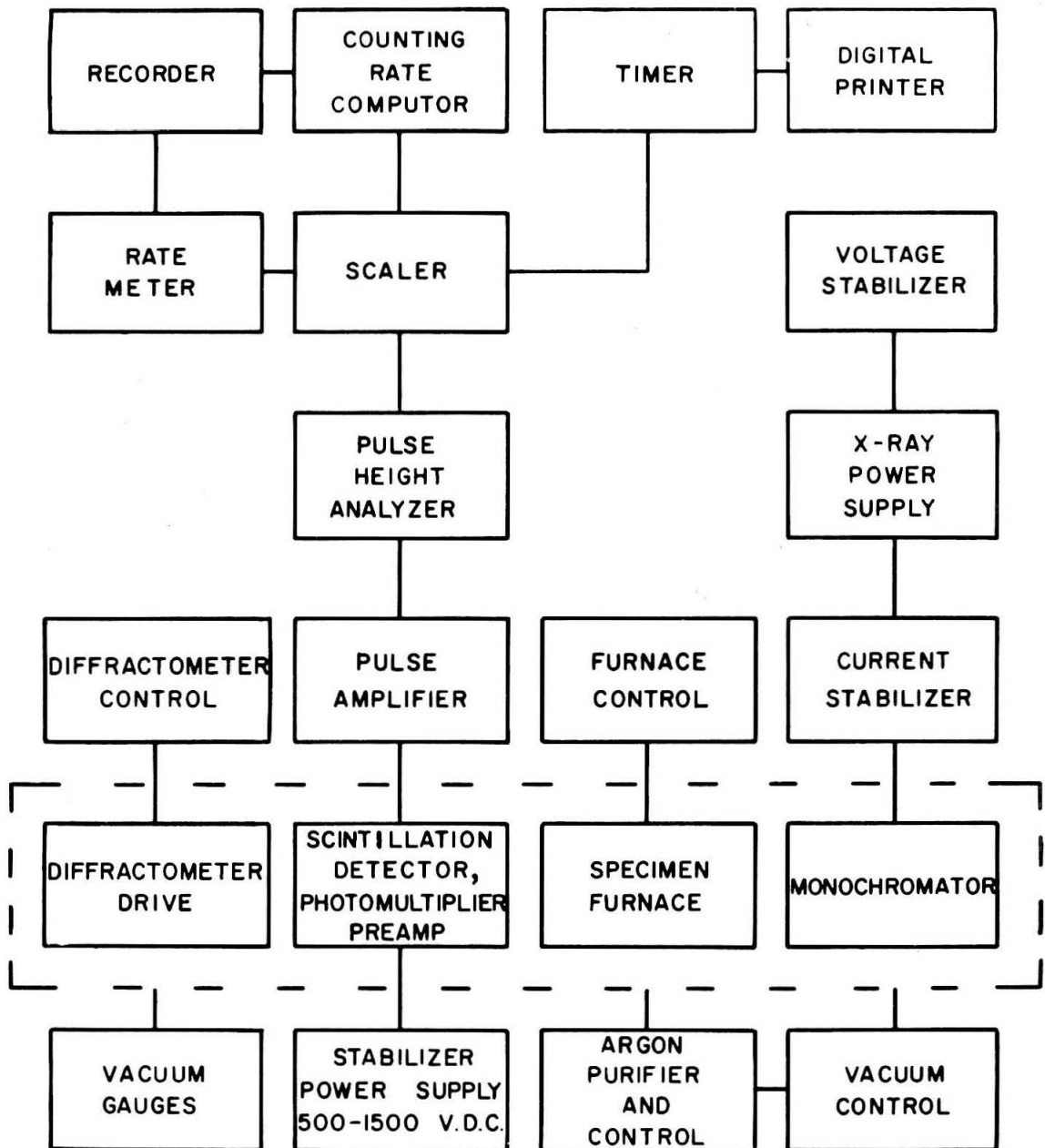


Figure 2. Schematic of the high temperature x-ray diffractometer installation.

convenient to discuss separately the vacuum system and its associated electronics, the diffractometer and its components, the monochromator, the goniometer and the drive.

2.1 The Vacuum System and Its Associated Electronics

The vacuum system is shown in Figure 3 and schematically in Figure 4. The vacuum chamber, which is constructed of 3/8 inch stainless steel, is six feet in diameter and four feet high. The three electrode ports are designed so that glass-to-metal seals can be installed on each port and then bolted to a mating flange located on the bottom half of the vacuum chamber. The diffractometer sets upon a ledge inside the chamber so that no misaligning strains will be transmitted to the instrument when the chamber is under atmospheric loading.

The pumping system consists of a Kinney KS-47 mechanical pump, a Consolidated Vacuum MGH-900 3-stage mercury diffusion pump and a cold trap. The cold trap is divided into two sections; adjacent to the diffusion pump is a Freon cooled baffle operated at -25°C and after the baffle is a liquid nitrogen cold trap with a capacity of 22 liters. Between the liquid nitrogen cold trap and the vacuum chamber is a Consolidated Vacuum QSV-8 quarter swing, straight-through valve.

This system, after two days of pumping, attains a pressure of 2×10^{-6} mm of mercury. The vacuum pressure is measured by a Pirani Gauge for the high pressure region and an Ionization Gauge for pressures down to 10^{-7} mm. The circuit for the Ionization Gauge is basically the one designed by Elmore and Sands⁽⁴⁰⁾.

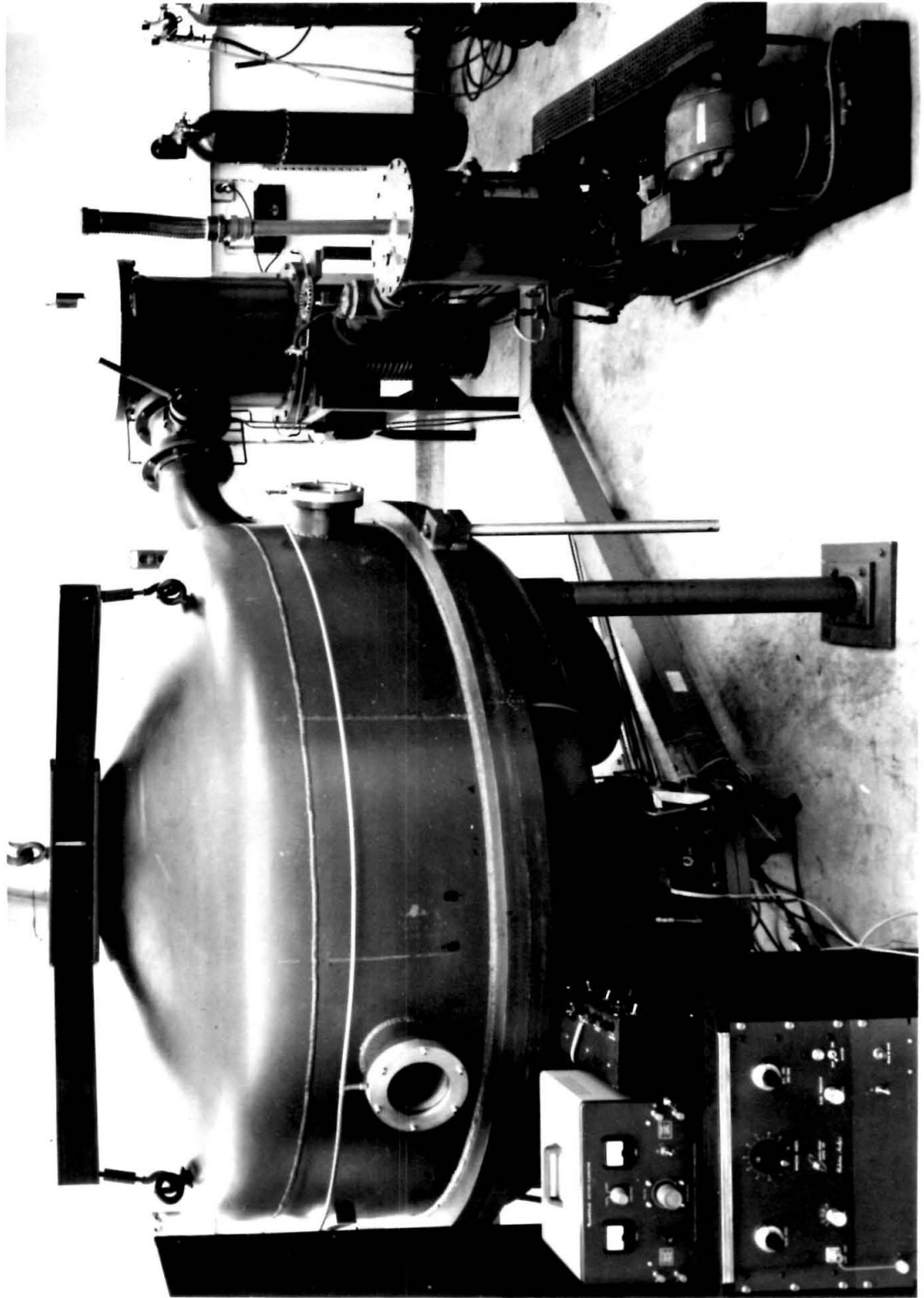


Figure 3. The vacuum system.

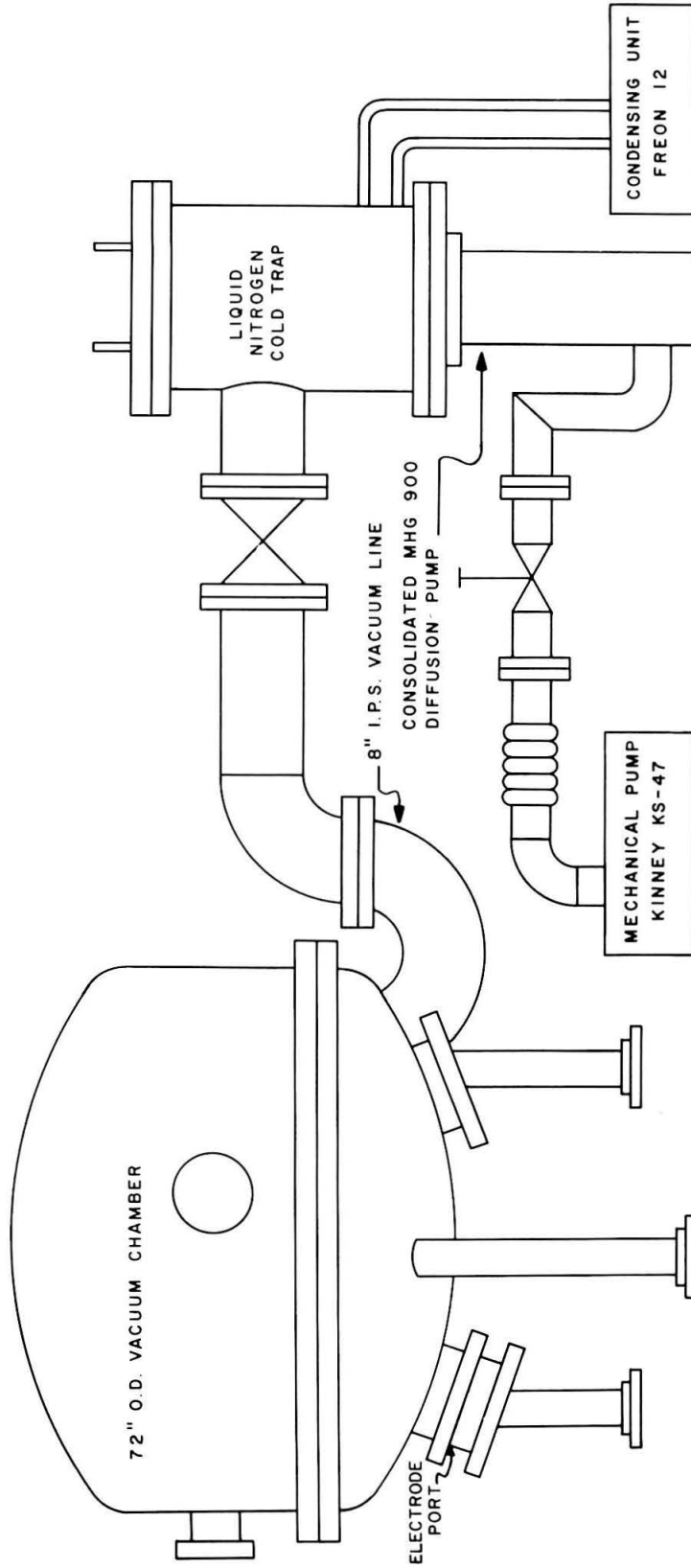


Figure 4. Schematic of the vacuum system.

As stated previously, a pressure of 10^{-6} mm of air is not low enough to prevent rapid contamination of a metal like titanium. To eliminate this problem, all possible places where air could leak into the vacuum system are surrounded by highly purified argon. Every O-ring seal on the high vacuum side of the diffusion pumps is a double O-ring seal with a space between the O-rings for pumping out and filling the region with purified argon. All electrodes and water lines that go into the vacuum chamber first pass through a chamber filled with purified argon. The regions where argon is required are automatically flushed, filled and maintained at a pressure slightly higher than one atmosphere. After the initial pump down, the chamber is flushed several times with argon and, as a last measure, a titanium wire is heated to "getter" the remaining oxygen and nitrogen. In this way, it is possible to obtain a partial pressure of oxygen and nitrogen several orders of magnitude less than the pressure in the vacuum chamber. The schematic circuits for the vacuum controls and argon purifying system are shown in Figures 5 and 6.

The diffusion of mercury through the cold trap into the chamber can be troublesome in two ways; the possible contamination of the specimen and corrosion of the metal parts subject to amalgamation. To reduce the possibility of back diffusion of mercury, a baffle with indium inserts is placed between the cold trap and vacuum chamber.

2.2 The Diffractometer

The diffractometer is shown from two opposite sides in Figure 7 and a simplified plan view in Figure 8. Referring to Figure 8, the

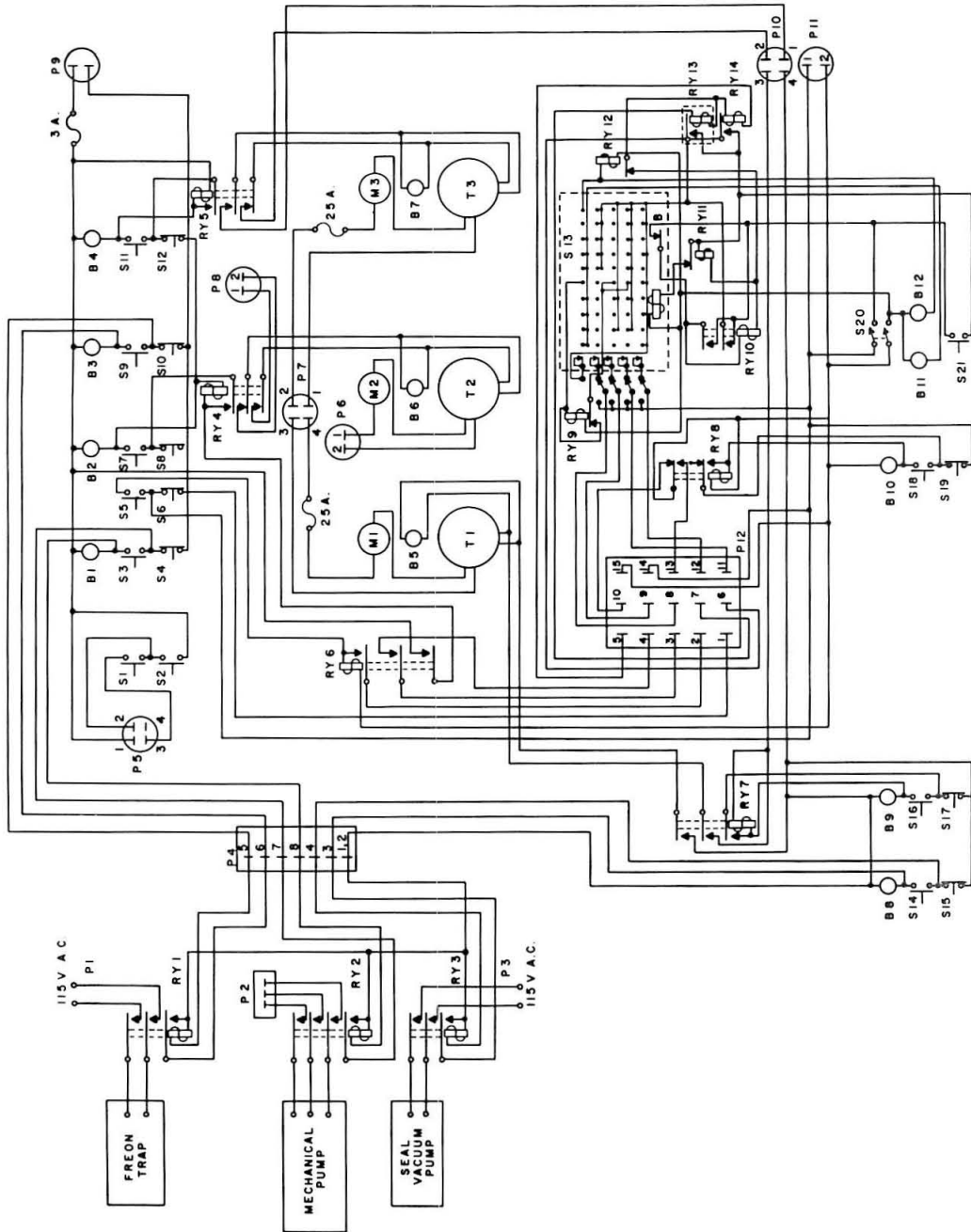


Figure 5. Schematic of vacuum control circuit.

Key to Figure 5

S1, S2, S3, S5, S7, S9, S11, S14, S16, S18, S21 -- Push Button Switch, NO

S4, S6, S8, S10, S12, S15, S17, S19 -- Push Button Switch, NC

S13 -- Stepping Switch, 10 position, 5 banks

S20 -- DPST Toggle Switch

B1-B12 -- NE-51 Lamps

M₁, M₃ -- A.C. Ammeter 0-25 A

M₂ -- A.C. Ammeter 0-15 A

T 1 -- Variac, 115 V.A.C.; Purifying Furnace

T 2 -- Variac, 230 V.A.C.; Diffusion Pump

T 3 -- Variac, 115 V.A.C.; Getter

P 1, P 3 -- 115 V.A.C.

P 2 -- 230 V.A.C. 3 Phase

P 4 -- Jones Plug

P 5 -- Jones Plug; to Hoist

P 6 -- Cannon Plug; to Diffusion Pump

P 7 -- Cannon Plug; 1 and 2 to Getter, 3 and 4 to Purifying Furnace

P 8 -- 230 V.A.C., 1 phase

P 9 -- 115 V.A.C.

P 10 -- Cannon Plug; 1 and 2 to 115 V.A.C., 3 and 4 to 115 V.A.C.

P 11 -- 115 V.D.C.

P 12 -- Amphenol Plug; to Argon Purifying Cabinet

Ry 1 - Ry 14 -- Relays

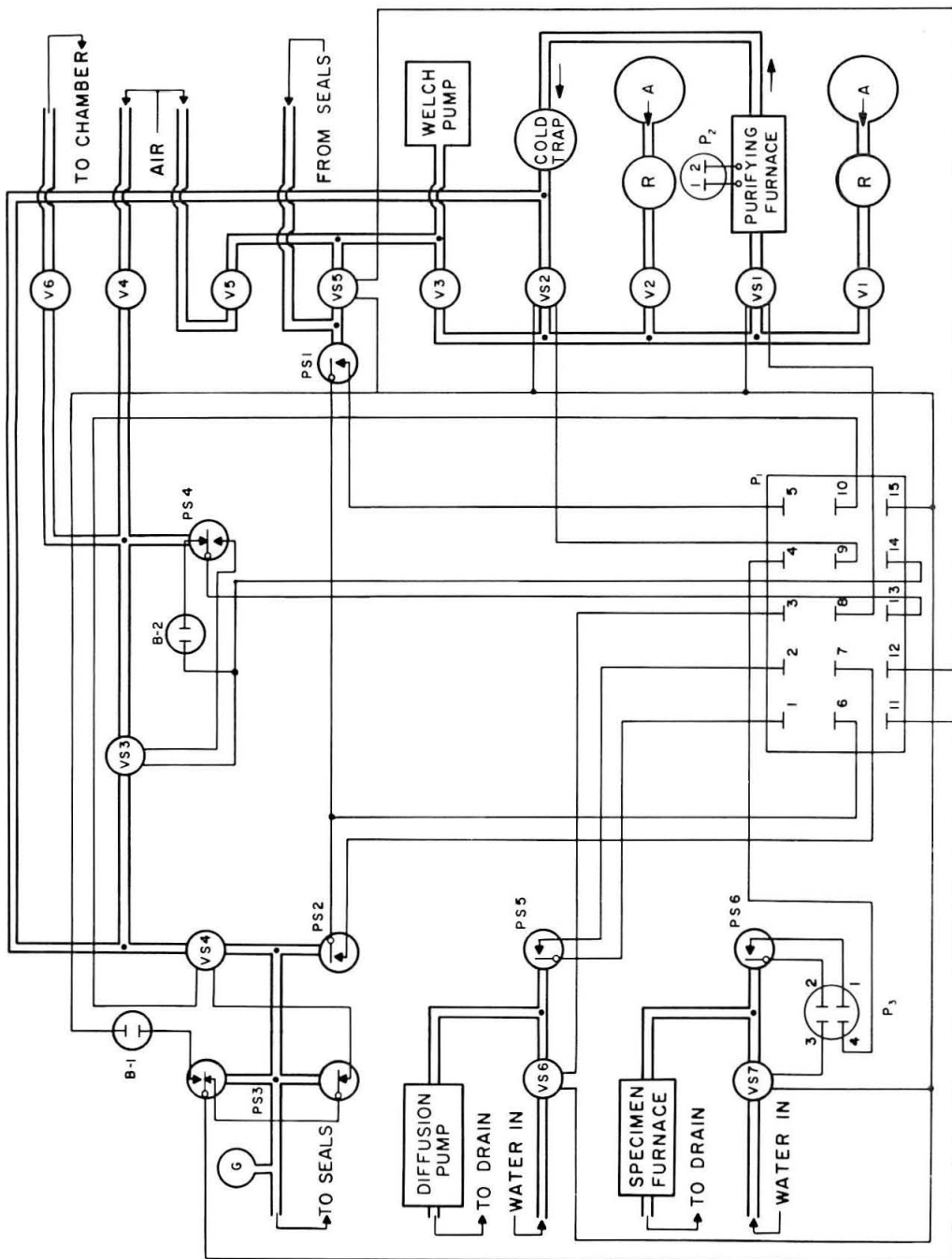


Figure 6. Schematic of Argon purifying system.

Key to Figure 6

V1 - V6 -- Hand Operated Valves

V S1 - V S7 -- Solenoid Operated Valves, N.C.

PS 1, PS 5, PS 6 -- Pressure Switch, N.O.

PS 2 -- Vacuum Switch, N.O.

PS 3 -- Pressure Switch, D.P.D.T.

PS 4 -- Pressure Switch, S.P.D.T.

A -- Argon Storage Cylinders

R -- Gas Regulator

G -- Pressure Gauge

B1, B2 -- NE-51 Lamps

P1 -- Amphenol Plug; to Vacuum Control Cabinet

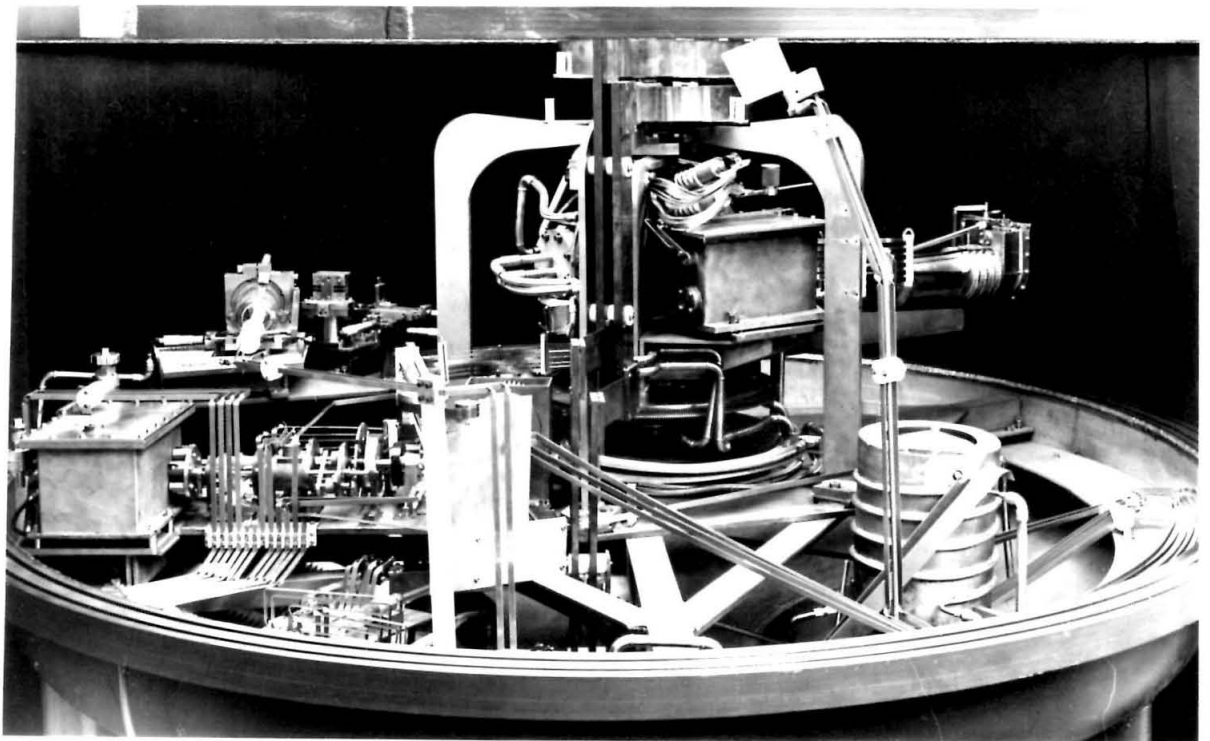
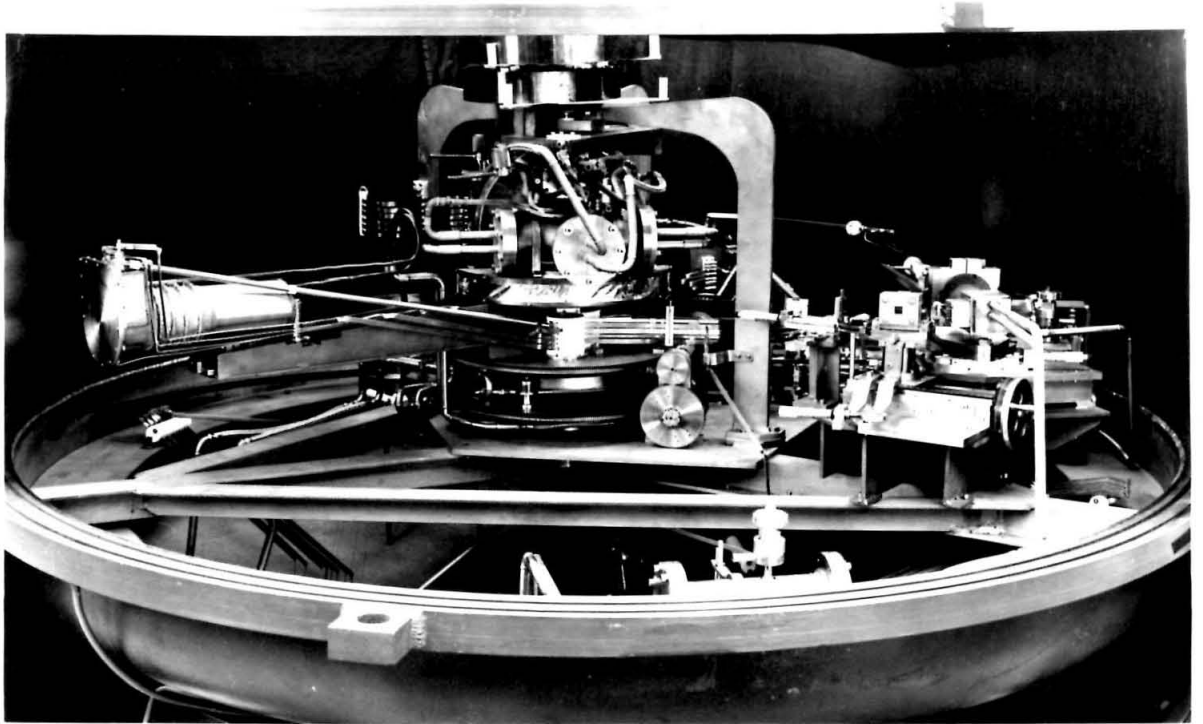


Figure 7. Front and back views of diffractometer.

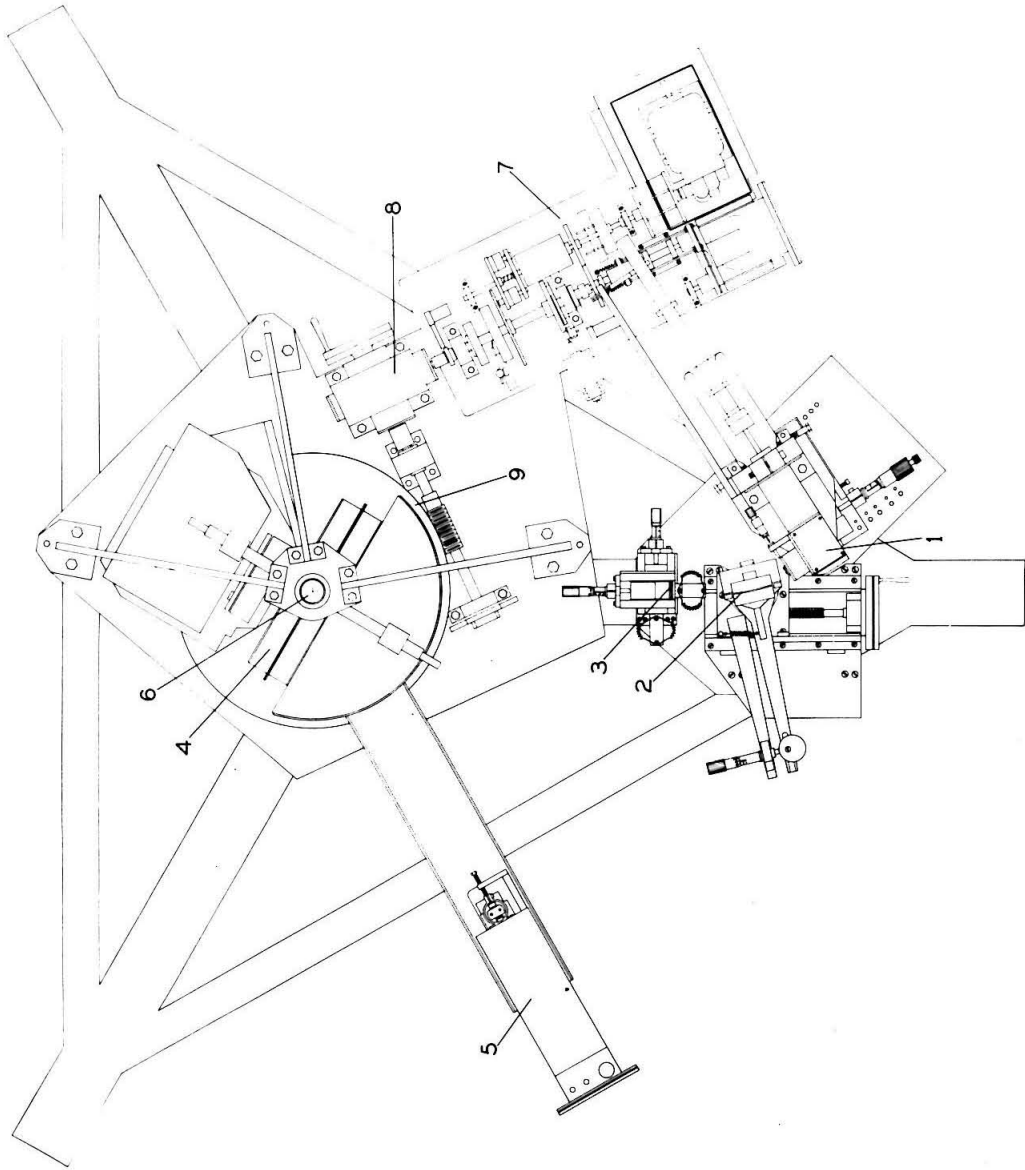


Figure 8. Plan view of diffractometer.

diffractometer operates as follows: the x-ray beam originates at a line focus General Electric CA-7 x-ray diffraction tube (1) and is directed towards a curved quartz crystal (2), which serves to monochromate and focus the beam at the slit (3). The monochromatic beam leaving the slit is wedge-shaped with an angle 1° and a height of just over one centimeter. The beam is then directed towards the furnace (4) which contains the material to be investigated. The diffracted x-rays are picked up by a scintillation detector (5), which rotates about the axis (6) at twice the angular speed with which the plane of the specimen rotates about this same axis. This speed ratio is the necessary and sufficient condition for a Bragg or Brentano type focusing spectrometer. The motions that are required by the instrument are produced by the drive (7), operating through a 50/1 gear reduction box (8), and then to a set of worm gears (9).

The instrument is almost entirely constructed of stainless steel. Teflon and glass are the only two non-metallic materials used in the chamber because of their non-degassing properties⁽⁴¹⁾. During final assembly, with surgical gloves, all traces of oil are removed from the instrument. The instrument is heated in high vacuum by infrared heaters as a final precaution against contaminating vapors.

Ball bearings, sleeve and thrust bearings have to be used in many of the mechanisms involved in the diffractometer drive. The requirement for a very clean atmosphere in the vacuum chamber prohibits the use of hydrocarbon lubricants. The vacuum system for the diffractometer does not have an oil diffusion pump; therefore any lubrication

which might be obtained by backstreaming oil vapor is absent. Barium cannot be used as a lubricant because the instrument must be frequently exposed to air.

Under such conditions of non-lubrication, the bearings do not have any appreciable life. As a typical example, a stainless steel ball bearing, 26 mm outside diameter, rotating at 100 rpm with a very small load is completely frozen after about 5000 revolutions. Apparently, as the oxide coating on the balls and the race is broken, small welds occur between the balls and the race which leads to a rapid deterioration of the bearing surfaces. Molybdenum-disulfide was tried as a possible solid lubricant without success. Possibly the reason for the molybdenum-disulfide failure is as the ball rolls in the race it pushes a small amount of molybdenum-disulfide ahead of it and every so often the ball jumps over this mound causing indentations in the ball race.

The use of teflon as a lubricant proved to be a satisfactory solution to this problem. Lubrication by teflon is achieved by continually rubbing a bearing surface against a solid piece of teflon, thus coating it with a thin layer of teflon. The procedures used depended upon the type of bearing. For instance, in ball bearings the steel cage is replaced by a teflon cage; in sleeve bearings small teflon inserts are placed between the housing and the shaft. Several different and special designs are used for thrust bearings depending upon the application.

2.3 The Monochromator

The only possibility of coping with the thermal diffuse scattering problem is to make the diffraction peaks as sharp as possible, have a

very high signal to background ratio, and have a very monochromatic beam. These factors necessitate the use of a line focusing monochromator⁽⁴²⁾. There are two possible positions where the monochromator can be located: either between the x-ray tube and the specimen, as in this instrument, or between the specimen and the detector as illustrated in Figure 9. The advantage claimed by the proponents^(43, 44) of the latter method is elimination of incoherent radiation, i. e., fluorescent and Compton scattering by the specimen. These two objections are unfounded in most x-ray diffraction studies on metals. Fluorescent scattering can usually be eliminated by choice of the proper radiation or pulse height discrimination and the Compton scattering is usually nil since the atomic numbers are high and x-ray photon energies are low (the order of 10 kev.). Also, this latter method has one large disadvantage. The prerequisite of a sharp diffraction peak requires a sharply focused x-ray source. This requires that the focal spot or projected focal spot on the x-ray tube be very sharp which results in a large loss of intensity in the x-ray beam. The direct beam monochromatization technique does not have this objection.

The intensity diffracted and focused by a monochromator is directly proportional to the incident intensity striking it at the correct Bragg angle. Since the focusing process is caused by diffraction and not reflection, as in a mirror, the focused image is virtually independent of the size and position of the source. The dependence of position on intensity can be derived as follows. Referring to Figure 10, consider an infinitesimal area on the surface located at P_0 . All radiation

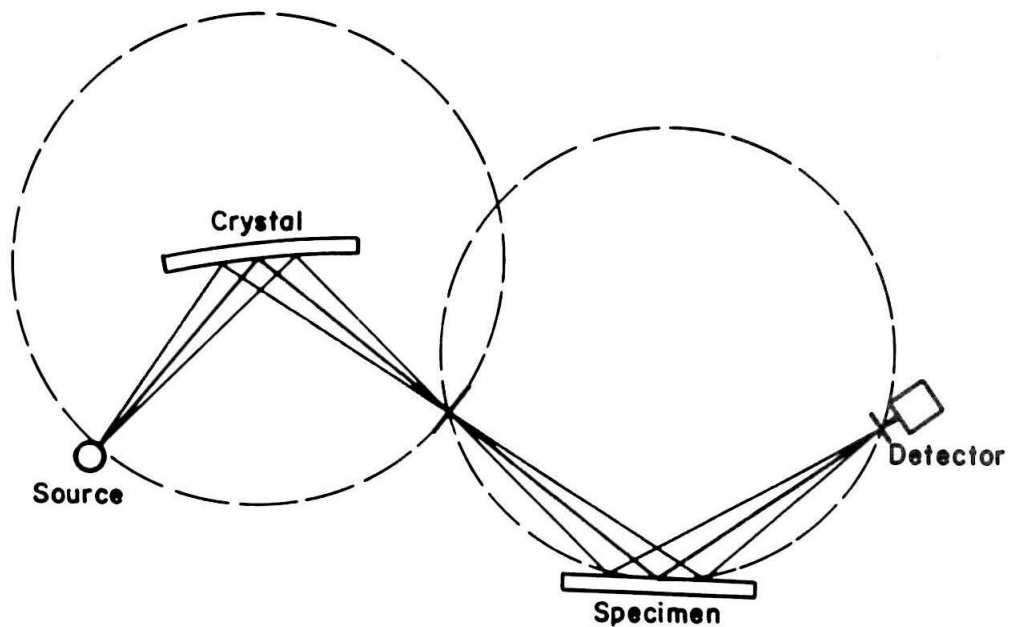
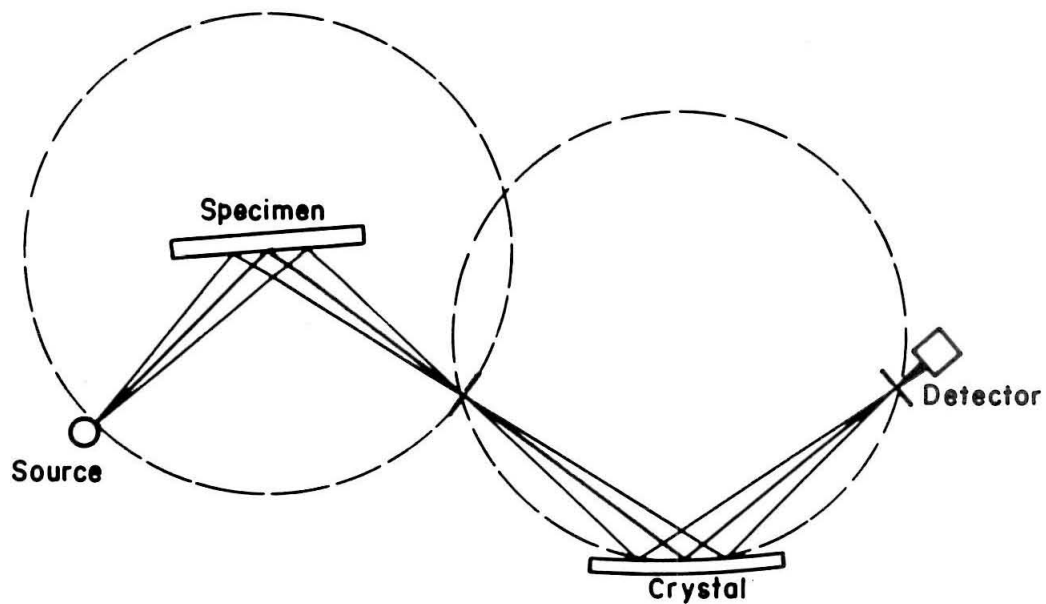


Figure 9. Direct and diffracted beam monochromatization.

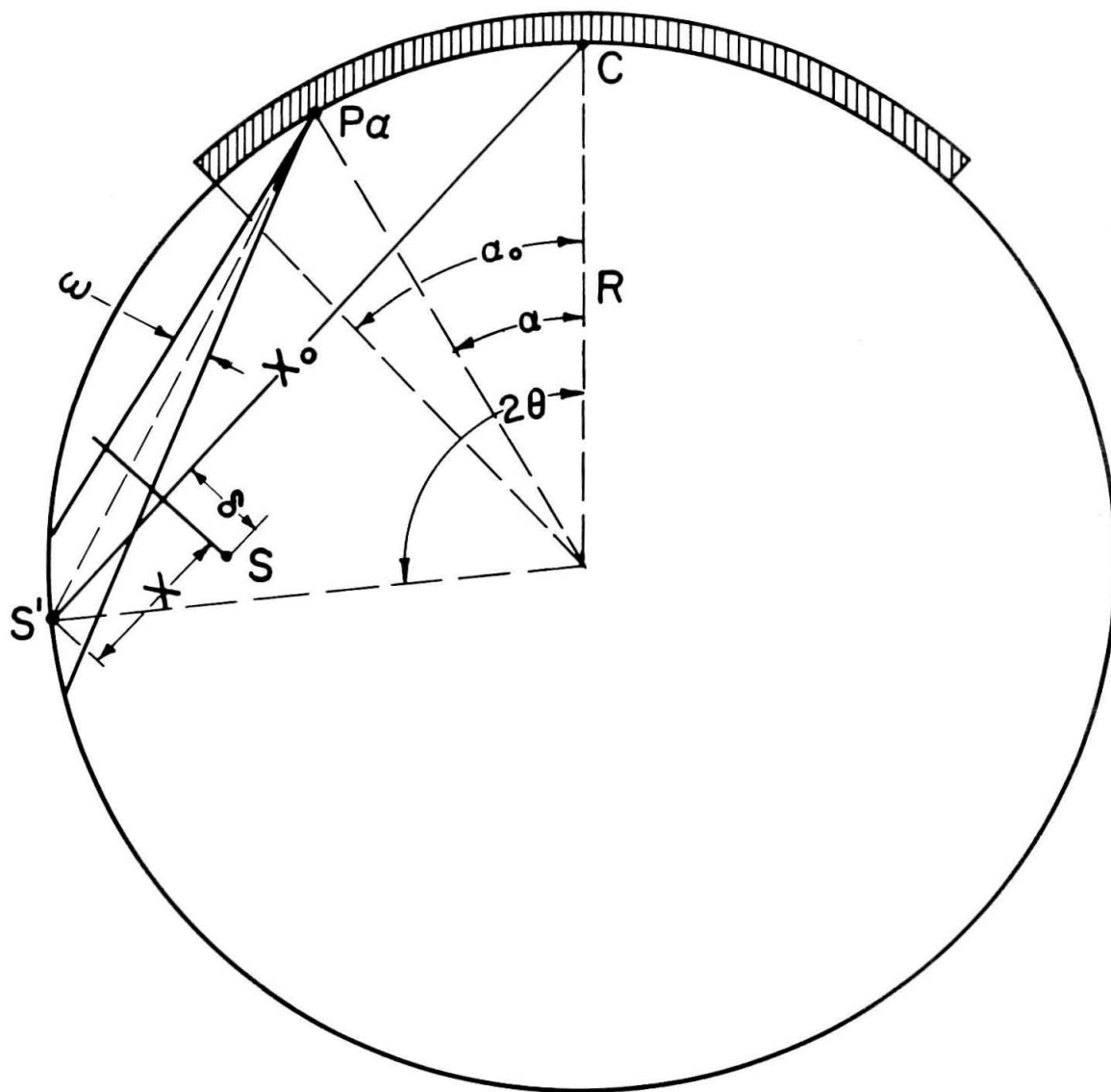


Figure 10.

emanating from the source S, of length of 2δ , and within the angle ω satisfies the conditions for Bragg diffraction. The source S is assumed to emit a uniform intensity in the direction of the crystal and the angle ω is assumed to be the same over the entire crystal. The line joining the virtual source, S', with any point of the monochromating crystal whose surface lies on the focusing circle makes the correct Bragg angle with the crystallographic planes. The distance from S' to S is x and the angles α_0 and ω are small. By simple geometrical considerations the intensity I_α , striking the crystal at P_α and satisfying the Bragg conditions for diffraction is,

$$I_\alpha \approx k\omega \left[2R \sin \left(\theta - \frac{\alpha}{2} \right) - x \right] \quad (2.1)$$

where the proportionality constant k represents the intensity of x-rays per unit area of the source in the direction of the crystal. The line $P_\alpha S'$ must intersect S as x is varied, otherwise $I_\alpha = 0$. This condition can be expressed as

$$|x| \leq \delta \cot \frac{\alpha_0}{2}, \quad (2.2)$$

or for small α

$$|x| \leq \frac{2\delta}{\alpha_0}. \quad (2.3)$$

Integrating along the surface of the crystal, the total intensity I, which can be diffracted and focused is

$$I = 2 \int_0^{\alpha_0} k\omega \left[2R \sin \left(\theta - \frac{\alpha}{2} \right) - x \right] R d\alpha \quad |x| \leq \frac{2\delta}{\alpha_0} \quad (2.4)$$

and

$$I = 2 \int_0^{\frac{2\delta}{|x|}} k\omega \left[2R \sin\left(\theta - \frac{\alpha}{2}\right) - x \right] R da \quad |x| \geq \frac{2\delta}{a_0} \quad (2.5)$$

Integrating equations 2.4 and 2.5, and simplifying

$$I = 2k\omega R a_0 (x_0 - x) \quad |x| \leq \frac{2\delta}{a_0} \quad (2.6)$$

$$I = 4k\omega R \frac{\delta}{|x|} (x_0 - x) \quad |x| \geq \frac{2\delta}{a_0} \quad (2.7)$$

where x_0 is the distance from S' to C . If $I_{S'}$ is the intensity when the source is located at the virtual position S' , then equations 2.6 and 2.7 can be simplified to

$$I = I_{S'} \left(1 - \frac{x}{x_0} \right) \quad |x| \leq \frac{2\delta}{a_0} \quad (2.8)$$

$$I = I_{S'} \left(\frac{2\delta}{a_0 |x|} \right) \left(1 - \frac{x}{x_0} \right) \quad |x| \geq \frac{2\delta}{a_0} \quad (2.9)$$

Figure 11 schematically shows the dependence of intensity on source position. It can be seen that I_{\max} occurs when $x = -\frac{2\delta}{a_0}$, that is, when the source just fills the total angular divergence of the beam behind the source image.

The monochromator is shown in perspective in Figure 12. It is designed to be used with six different characteristic radiations -- tungsten L, nickel K, cobalt K, iron K, manganese K and chromium K. This includes a characteristic wavelength spectrum from 1.48 Å to 2.29 Å. The approximate focusing conditions⁽⁴⁵⁾, rather than the exact

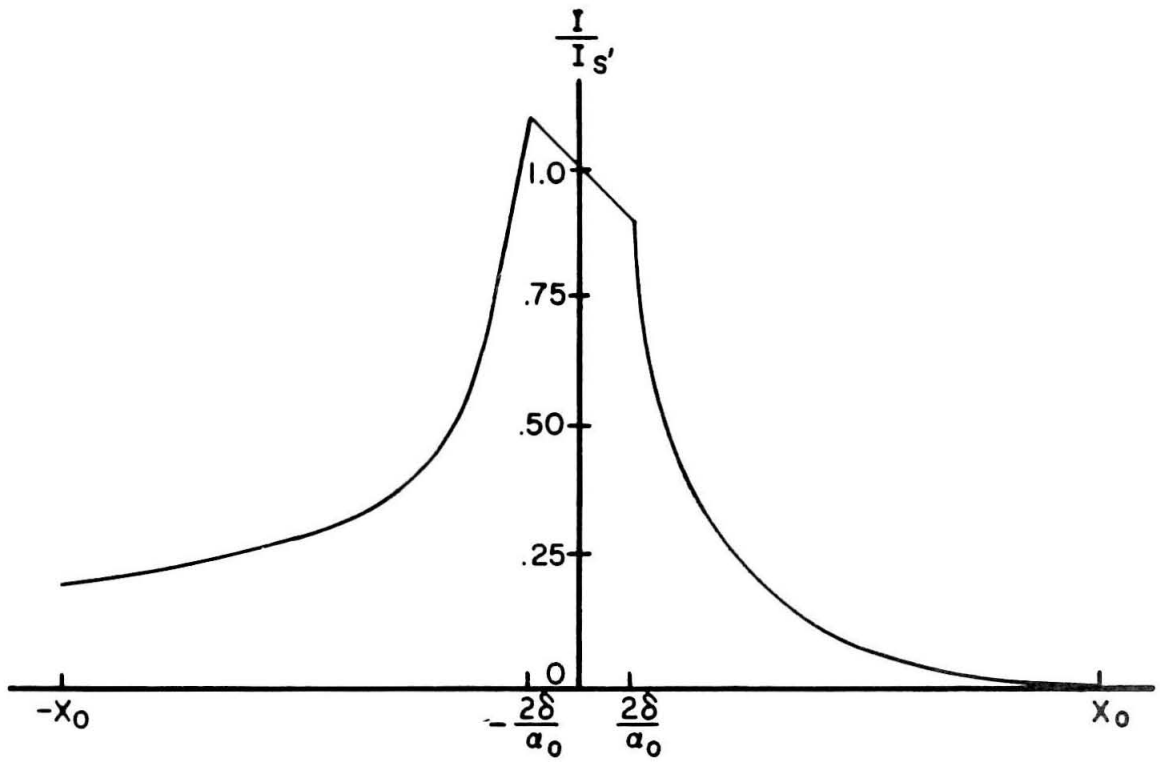


Figure 11. Dependence of diffracted intensity upon source position.

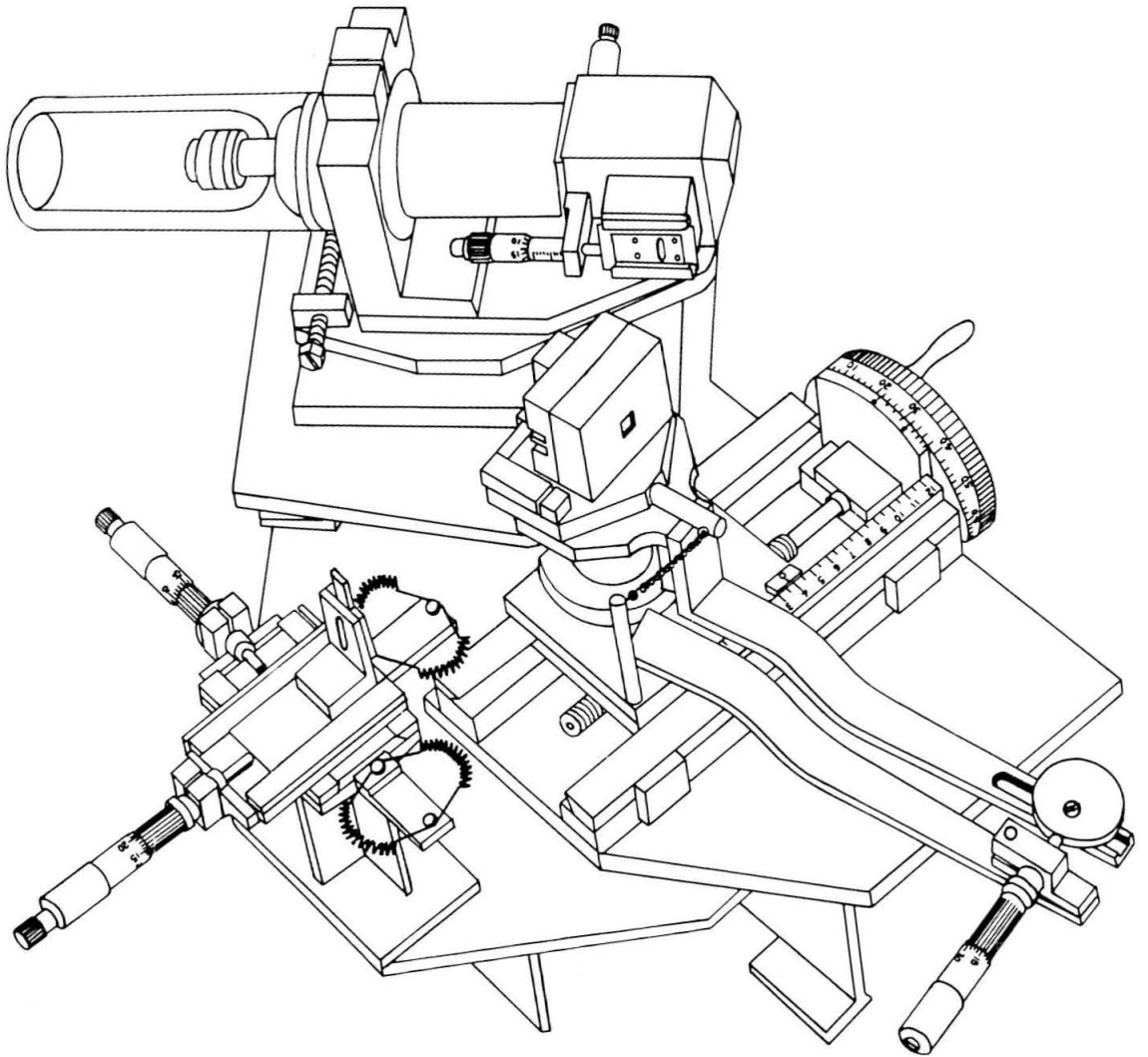


Figure 12. The monochromator.

focusing conditions are used. In this case an optically flat single crystal of quartz, with the (10 $\bar{1}$ 1) plane parallel to the surface, is bent to a radius of $2R$, where R is the radius of the focusing circle. The monochromator in this instrument has $R = 25$ cm. The (10 $\bar{1}$ 1) planes of quartz were chosen because of their high reflecting power and sharp focusing properties⁽⁴⁶⁾.

The distance from the slit to the center of the crystal is proportional to the wavelength which is to be focused at the slit. This distance is adjusted by a screw-driven carriage. The orientation of the crystal relative to the slit is adjusted by a long micrometer driven lever arm which rotates the crystal about an axis coincident with the center of the crystal face. The supports of the crystal block have six degrees of freedom for final alignment. The x-ray tube mount can assume six different positions relative to the slit depending upon the characteristic radiation desired. These positions are determined by six sets of locating holes on the tube mounting plate. The tube mount has a translational degree of freedom for final adjustment of the tube focal line and a rotational degree of freedom to vary the "take-off-angle" from the target.

The crystal and its clamping blocks are shown in Figure 13. The clamping blocks were turned to a 50 cm radius on a lathe. The final profiling of the clamping blocks to a uniform radius was accomplished by a lapping procedure recommended by J. W. M. DuMond⁽⁴⁷⁾. The quartz crystal was cut from a large crystal free from mechanical and electrical twinning. The initial size of the crystal was one inch square

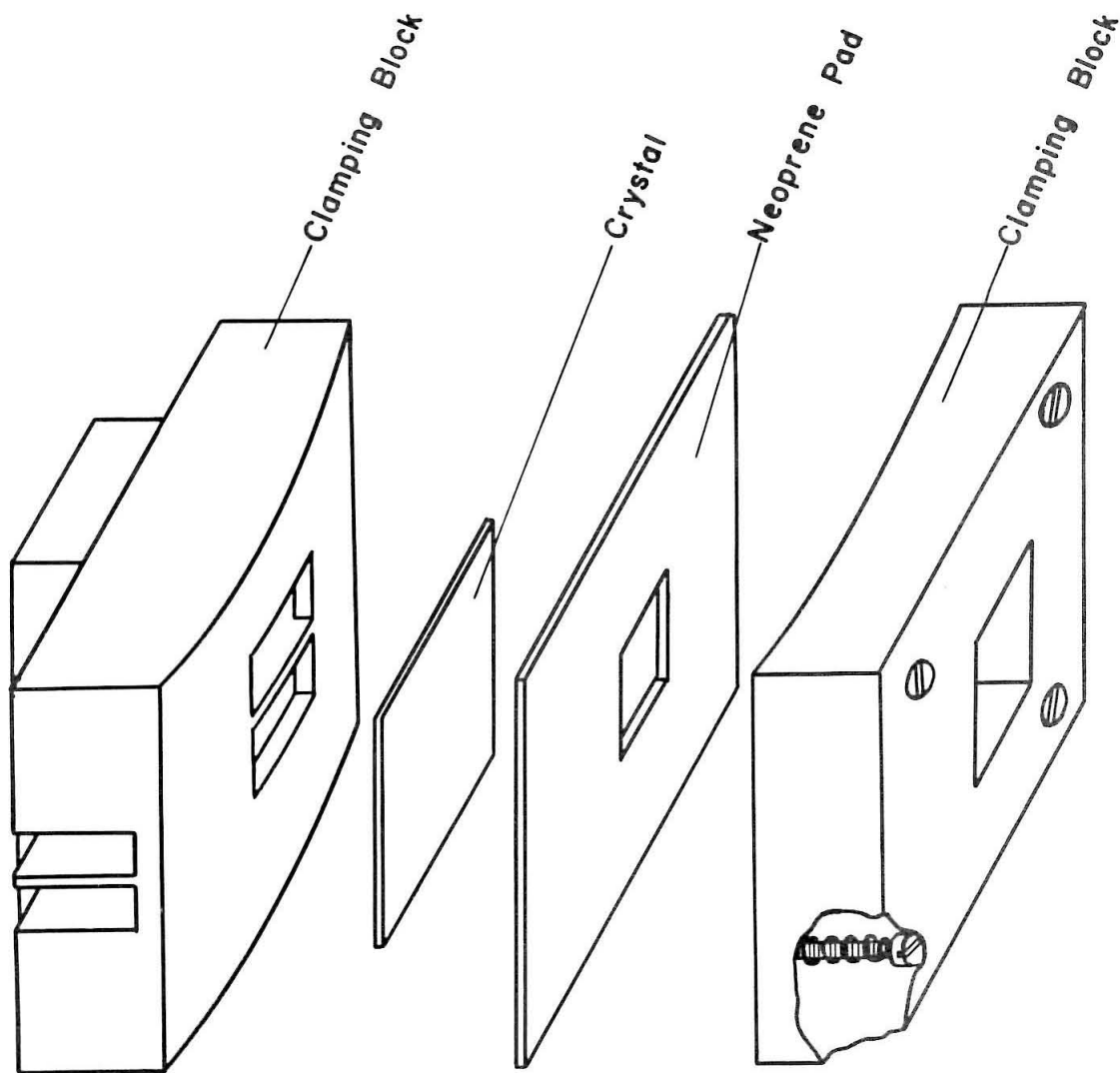


Figure 13. The crystal and clamping blocks.

by 1/8 of an inch thick. The orientation of the $(10\bar{1}1)$ planes relative to the surface was determined to $\pm 0.01^\circ$ by using a special goniometer attachment on a Norelco diffractometer. The orientation error was corrected and then the crystal was ground to a thickness of 0.5 mm and polished optically flat to about 1/4 of a fringe. The crystal was clamped in the blocks over 84% of its area. The web in the center of the front block suppressed any anticlastic curvature in the crystal. Pressure was brought to bear on the crystal by a neoprene pad and four compression springs located at the corners of the crystal block.

There are five sources which can cause aberration of the focused image from the monochromator. These are (1) departure of the crystal surface from the focusing circle as prescribed by the approximate focusing conditions, (2) penetration of the x-rays into the crystal, (3) "crossfire" which results from radiation striking the crystal at an angle not perpendicular to a cylinder generator, (4) the mosaic characteristic of the crystal combined with the Darwin intrinsic width of diffraction and (5) the natural breadth of the characteristic x-ray line being focused. The aberration from the last two of these sources are intrinsic and with a given crystal nothing can be done except to carefully select the natural quartz from which the crystal is cut. The intrinsic diffraction width is very small and might lead to an aberration of the order of 0.001 mm at the focus. However, the natural breadth of tungsten $L\alpha_1$, $\Delta\lambda/\lambda = 8.4 \times 10^{-4}$ (48), leads to an aberration of 0.021 mm at the focus.

The first three sources of aberration are termed geometrical since they depend on how the crystal is bent. For all intents and purposes the "crossfire" aberration is extremely small and can be neglected. The aberration measured tangentially to the focusing circle due to departure of the crystal surface from the focusing circle is $\frac{1}{4} \alpha^2 R \cot \theta$ ^(43, 45), where R is the radius of the focusing circle, α is the angular divergence of the beam ($\alpha = 1^\circ$) and θ is the Bragg angle for diffraction. This aberration measured normal to the direction of propagation of the x-ray beam is $\frac{1}{4} \alpha^2 R \cos \theta$. The aberration measured normal to the direction of propagation due to the finite depth of penetration of x-rays into the crystal is $\frac{1}{2} e \sin 2\theta$ ⁽⁴³⁾, where e is the distance the x-rays travel in the crystal. A typical value for e is the distance traveled so that the beam intensity is reduced by a factor of 100, i. e., $e = 4.6/\mu$. μ must include both the normal attenuation of the x-ray beam and extinction. For quartz the normal absorption coefficient, μ_l , for tungsten L_α radiation is 83.7 cm^{-1} , while the primary extinction absorption coefficient, μ_e , for tungsten L_α radiation diffracted from the (10 $\bar{1}$ 1) planes of quartz is 989 cm^{-1} . Therefore, the total attenuation coefficient is 1073 cm^{-1} . This value overestimates the true attenuation coefficient since it neglects the mosaic structure of the quartz. The sum of these two aberrations for tungsten L_α radiation is 0.028 mm.

There is one compensating factor which tends to improve the geometrical aberration. The elastic strains in the crystal change the lattice spacing of the reflecting planes in such a way as to reduce the

aberration due to the depth of penetration. The depth of penetration aberration is toward a lower Bragg angle. However, the stress in the crystal changes from a state of compression on the front face of the crystal to a state of tension on the back face. This leads to a continually decreasing lattice spacing from the front to back face, which tends to cause an aberration toward a higher Bragg angle as the x-ray beam penetrates the crystal.

The geometrical aberration of the crystal is measured by a method equivalent to the Hartmann test applied to mirrors and lenses. A fine line of x-rays is directed to several different positions on the crystal and the center of the diffracted trace from each position is determined. Where the traces cross to a minimum cross-section is the location of the best focus and the cross-section represents the line of least confusion. Figure 14 shows the examined regions on the crystal and their corresponding traces. The aberration is 0.016 mm. This is less than the aberrations which cannot be eliminated, i. e., the source and the crystal diffraction. A film placed near the best focus shows a complete resolution of tungsten La_2 from tungsten La_1 ($\frac{\Delta\lambda}{\lambda} = 7.5 \times 10^{-3}$).

2.4 The Goniometer

The section of the instrument referred to as the goniometer measures the angular location and intensities of diffraction peaks. It basically consists of a furnace which contains a specimen and an x-ray detector. Both the specimen and detector must maintain the correct angular relationship with the primary beam to insure Bragg or Bretano

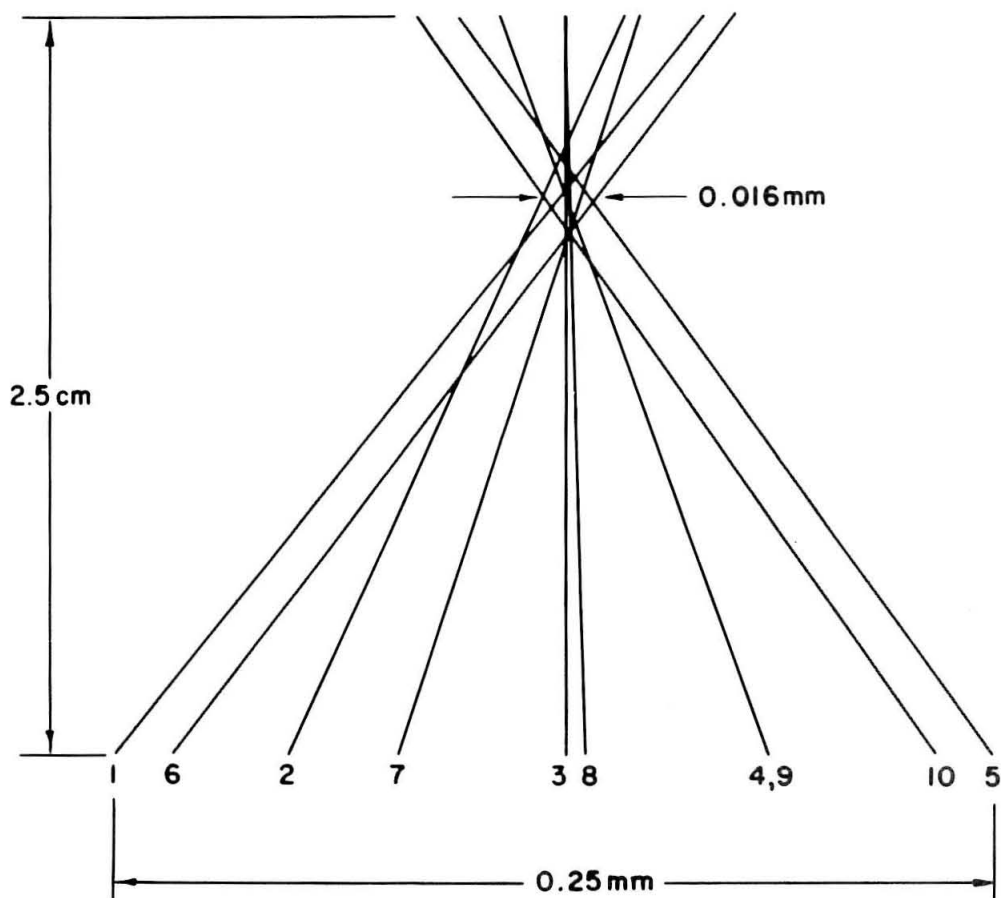
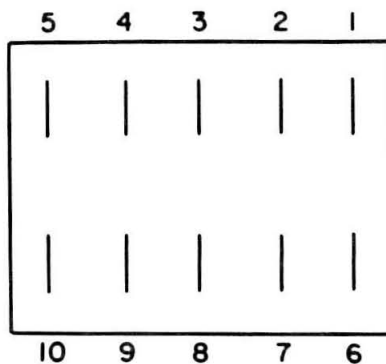


Figure 14. X-ray Hartman tests of the monochromator.

type focusing. The furnace and the detector are each rotated about a common axis by two bronze worm gears which have a pitch diameter of 15 inches. The 2 to 1 angular relationship between the detector and the specimen is maintained by two antibacklash spur gears which couple the two driving worms which have a pitch diameter of one inch. One revolution of the worm corresponds to a 1° rotation of the detector. The backlash is eliminated by opposing torques of 15 inch-pounds on the worm gears applied by a constant force coil spring. The success of this type of instrument necessitates that an axis of rotation be precisely defined. This is accomplished by two sets of precision angular contact bearings mounted in the "DB" position. Tolerances were imposed on the machining and bearings so that the total composite rotational error should not exceed 2.4×10^{-3} degrees. This corresponds to a relative error in interplanar spacings of less than one part in 50,000 for Bragg angles greater than 45° .

The solution to the problem of excessive grain growth at elevated temperatures is to make the x-ray beam scan over many grains or, since the grains are assumed to be large, a large surface area. This is accomplished by the form of the specimen as shown in Figure 16. Fifteen trapezoidal segments are riveted to a spoked wheel. The outside diameter of the wheel is 22.5 centimeters and the thickness of each segment is approximately 3 millimeters. After riveting, steps are taken to insure that the front faces of the specimen segments are coplanar. The rivets and spoked wheel are made of basically the same material as the specimen or a material that will not appreciably diffuse

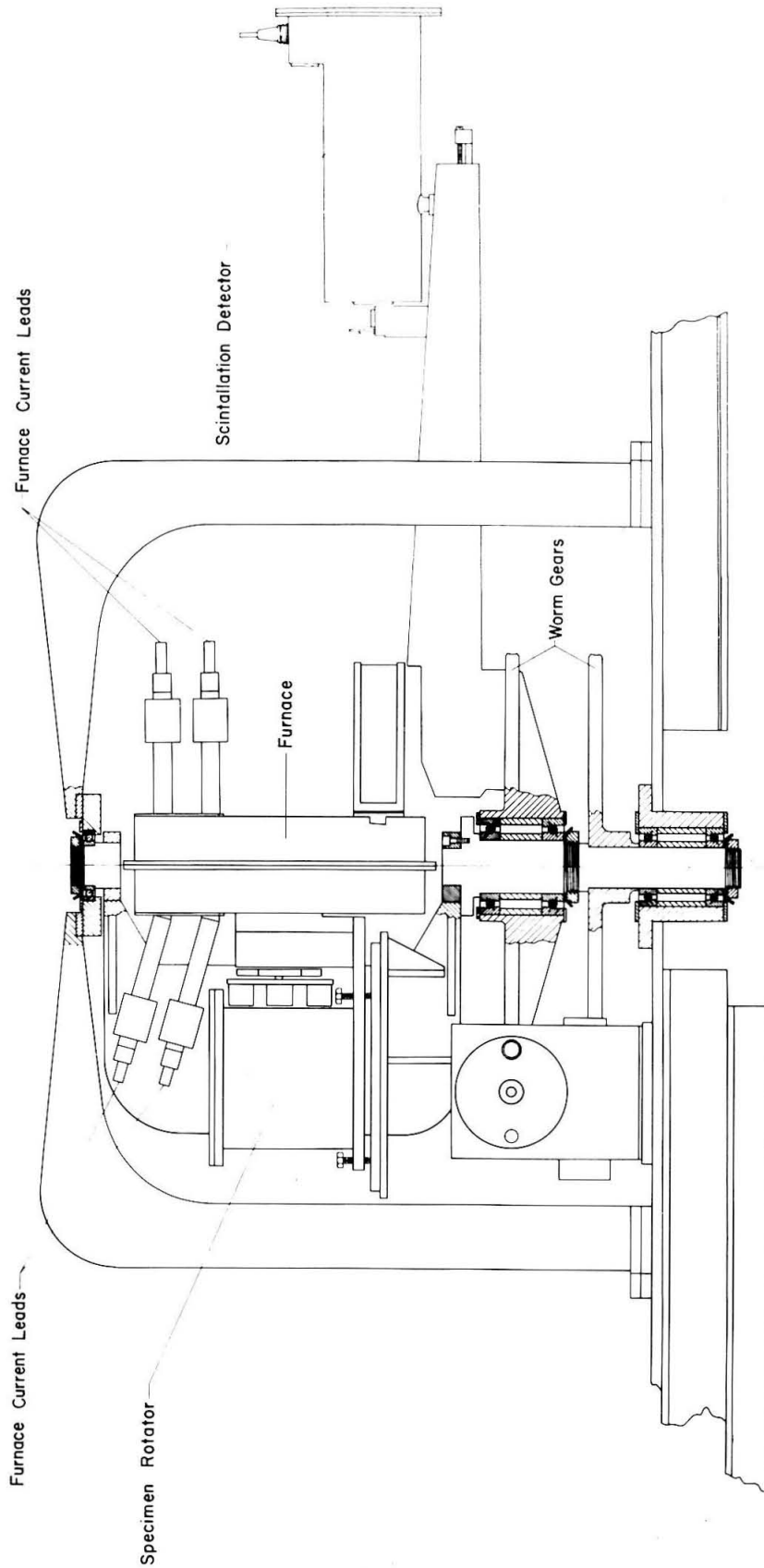


Figure 15. Vertical section through axis of rotation of goniometer.

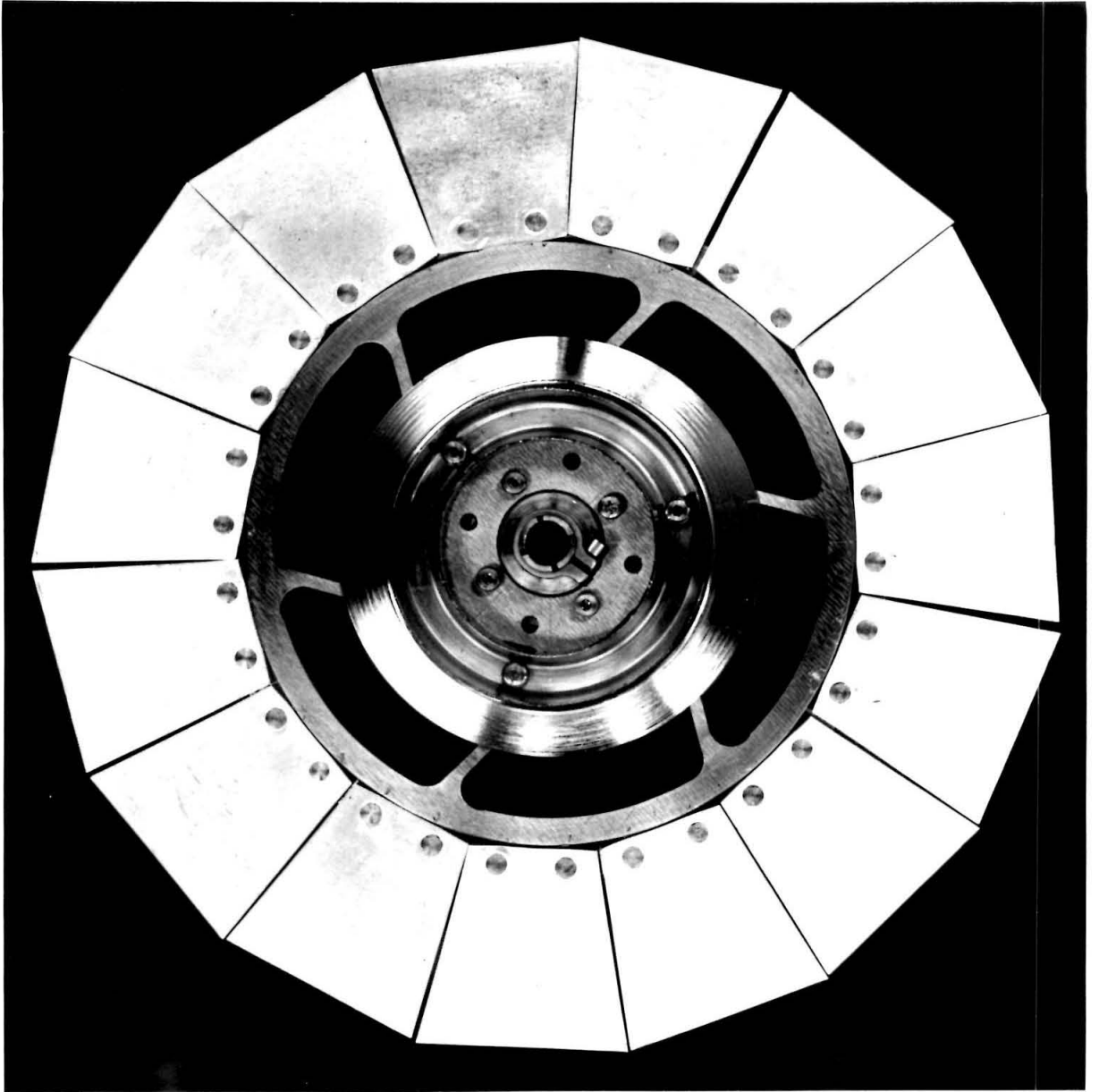


Figure 16. Specimen.

or vaporize on the specimen. The spokes of the specimen wheel are inclined to reduce the induced thermal stresses in the spokes. This annular shaped specimen wheel is then rotated in a toroidal shaped furnace. A slot is cut in the bottom of the furnace which permits the x-ray beam to enter and leave. The x-ray beam strikes the specimen nine centimeters from the axis of rotation which means that the x-ray beam scans over an area of 55 square centimeters. In this way an attempt is made to scan a large number of grains, as required by the powder method.

The furnace is designed to heat the specimen to 1200°C by radiation from an electrically heated element. A cross-section of the furnace is shown in Figure 17. The outer shell (1) is a water cooled nickel plated copper shield. This is to eliminate the possibility of heat being transferred to the instrument. A 15 micron aluminum foil (2), which covers the furnace opening for the x-ray beam, serves as a heat reflector. There are two sets of monel radiation shields (3) between the heater elements (4) and the water cooled shield. The heater elements are designed so that no ceramics are exposed to the vacuum system. This is achieved by winding the heater wire (5) in a spiral, insulating the turns from each other by alundum fish-spline insulators (6) and sealing the winding in a welded nickel case (7). The electrical connections are brought out through glass to metal seals (8). Provision is made to pump out the region that contains the heater coil, refill it with argon and then seal it off from the vacuum chamber. Two vaporization shields (9) are inserted between the specimen (10) and the heater

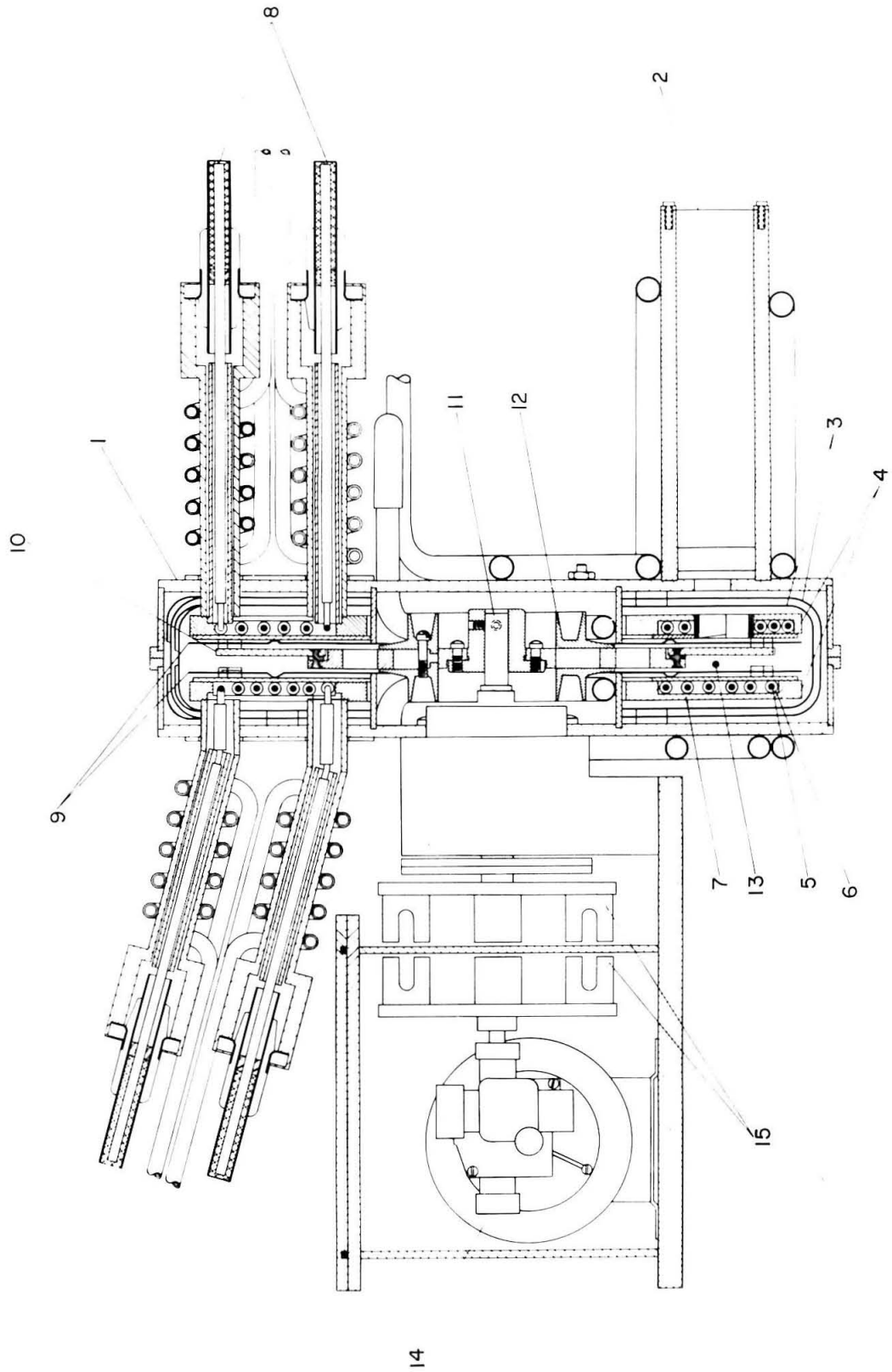


Figure 17. Cross-section through furnace.

elements. These shields are of the same material as the specimen to prevent the nickel heater case from vaporizing on the specimen. Heat transfer to the rotating shaft (11) by radiation from the furnace or conduction along the spokes of the specimen wheel is reduced by a set of cooling fins (12) which rotate in close proximity to a copper cooling coil. A platinum-platinum + 10% rhodium thermocouple is located in an approximate black body position (13). The motor (14) which rotates the specimen is inclosed in a stainless steel box filled with inert argon. The motor is coupled to the specimen by a set of magnets (15). The uniformity of the temperature within the furnace is not very critical for as the specimen rotates it averages out the temperature variations in the furnace. The furnace is allowed to go to thermal equilibrium by maintaining a constant power input.

Due to the use of the monochromator, the diffraction peaks are relatively low in intensity. Accurate intensity measurements in the least amount of time require a high detector efficiency and a high peak to background ratio. The best radiation detector suited for these conditions is a scintillation counter^(49, 50, 51). Its superiority to the Geiger and proportional counters with respect to quantum counting efficiency has been previously discussed⁽⁵²⁾. There is the added advantage over the Geiger counter of virtual elimination of the counter "dead time". High peak to background ratios and elimination of the $\lambda/2$ contribution to the diffraction peak can be obtained with the use of a pulse height discriminator. However, the energies of the x-ray photons used in x-ray diffraction studies are fairly low (from about 5.5 to 10 kev). In this low energy range, it is necessary that the electronics be capable of

producing a signal which is completely isolated from the photomultiplier and the amplifier noise.

The detector instrumentation can be described as follows. A single crystal of Na I(Tl) 1.5 cm square and 0.5 mm thick is hermetically sealed in a container. The attenuation coefficient for x-rays is so high for Na I ($\mu \approx 990 \text{ cm}^{-1}$ for tungsten L_{α} radiation) that the surface on which x-rays impinge must be extremely clear and free from cracks or scratches. To reduce the possibility of "light trapping" the crystal is cleaved. The crystal is thin to reduce the cosmic ray background. The x-ray beam enters the crystal container through a 0.005 inch beryllium foil coated with a 1 micron aluminum reflector on the side adjacent to the crystal. The crystal is optically coupled to a glass window through which the scintillation light pulses pass. This window is then optically coupled to the photomultiplier face with Dow Corning silicone stopcock grease. With this configuration, most of the light produced by the absorption of an x-ray photon by the Na I (Tl) crystal reaches the photocathode of the photomultiplier. The photomultiplier must be carefully selected both for low noise and high gain. The high gain is necessary to reduce the "noise-in-signal". A DuMont K1234 was found to be very successful with regard to the two previously mentioned prerequisites. (A K1234 is a 6292 specially selected for high gain.) The pulses from the photomultiplier are amplified with a gain of 4 by an adjacent preamplifier and then are sent out of the vacuum chamber by a cathode follower. The pulses are then amplified and pass through a pulse height discriminator

in a modified Nuclear-Chicago 1810 Radiation Analyzer. The modifications incorporated in the analyzer were changing the filament heater supply in the amplifier section to regulated DC and changing the discriminator window so that it can be adjusted between 0 and 20 volts. The pulses that can pass the pulse height discriminator are then sent to a rate-meter or scaler.

The performance characteristics of the scintillation detector were determined with tungsten L_{α_1} radiation. The photomultiplier was operated with 68 volts per stage except that first and second stages which were operated at 204 and 136 volts per stage, respectively. The total gain of the preamplifier and amplifier was 2500. The pulse height distribution curve, made with a 2 volt window, and the integral curve is shown in Figure 18. This is the first time, to the writer's knowledge, that the noise from a scintillation detector was reduced to a low enough value to show the escape peak for an x-ray photon of this low an energy without cooling the photomultiplier.

A comparison was made between a scintillation detector and a Geiger counter with regard to detection efficiency and peak to background ratio, when the sample was moderately fluorescing. A sample of titanium was mounted in a Norelco diffractometer and irradiated with copper radiation. The region about the $(10 \bar{1} 1)$ peak of titanium was scanned with (1) a Geiger counter (argon filled with a halogen quench and an active length of 10 centimeters), (2) a Geiger counter with a nickel filter and (3) a scintillation detector. Several scans were made with the scintillation detector, each using a different setting of the base

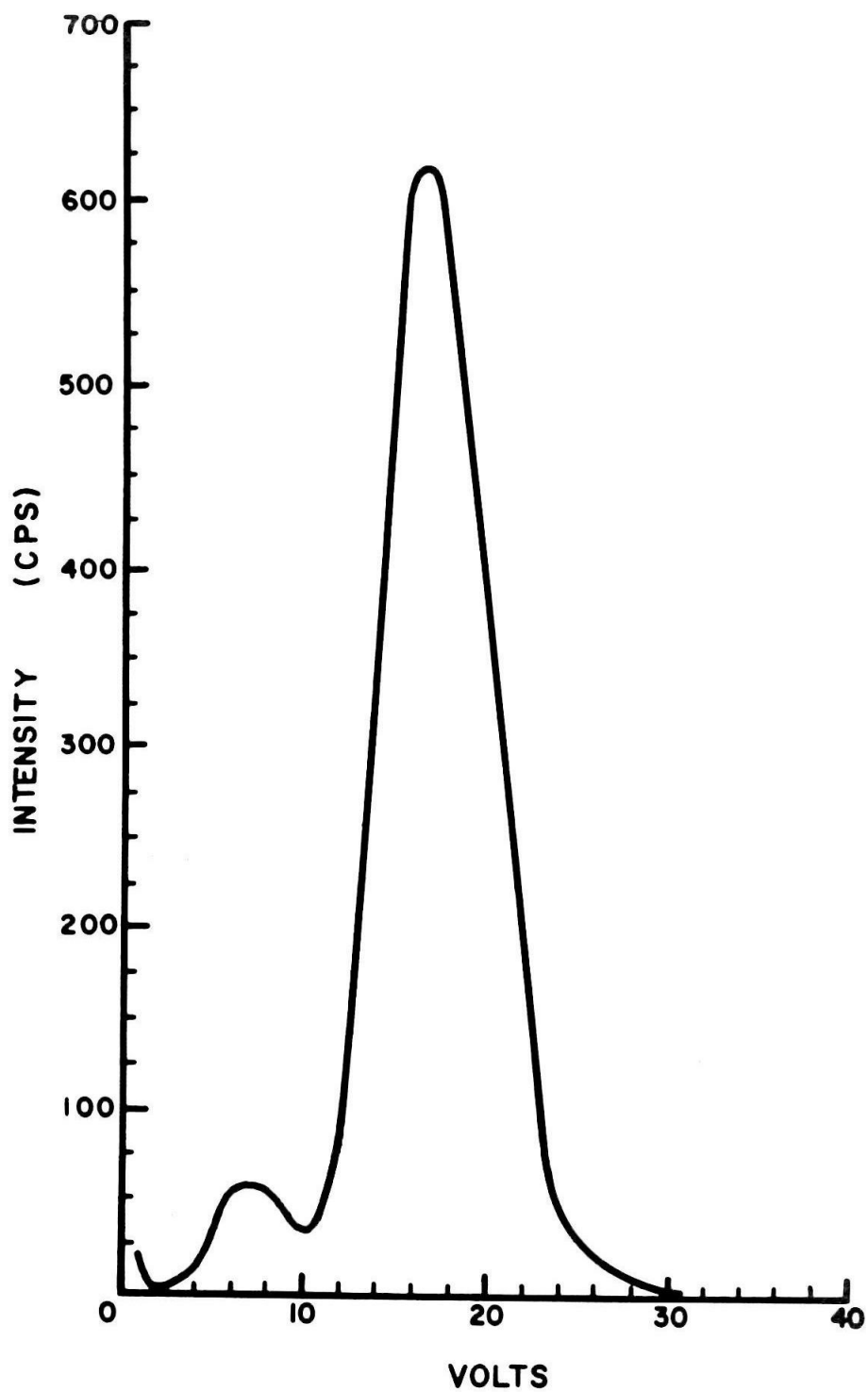


Figure 18. The pulse-height distribution of tungsten La_1 radiation.

level discriminator and a constant value for the upper level discriminator (16 volts). As the base was moved up, the fluorescent contribution to the peak and background was reduced. The results are compiled in Figure 19. It is interesting to note that for equal detection efficiencies the peak-to-background ratio for the scintillation detector is 8.6 times better than the Geiger counter or 2.4 times better than the Geiger counter with the nickel filter. For equal peak-to-background ratios the detection efficiency of the scintillation counter is 2 times better than the Geiger counter or 2.8 times better than the Geiger counter with the nickel filter.

2.5 The Drive

The drive was designed for continuous scanning and step scanning. When scanning continuously, the detector moves with a slow constant angular velocity and sends the x-ray pulses it receives to a rate meter whose output is connected to a chart recorder. This type of scanning is suitable for the approximate location and intensity of diffraction peaks, but the response time of the rate meter and recorder and the non-uniform statistics of the counting procedure limit the accuracy. The most accurate way to locate the center of gravity and intensity of a diffraction peak, with a given statistical error, is by the step scanning technique. In this type of scanning, the detector stays at a given angular position and accumulates a given fixed count. The time required for the fixed count is recorded digitally by a Berkeley printer working in conjunction with a Berkeley timer, or the intensity can be recorded

- ① - Dect. Eff. (%) - G.M. Counter
- ① - P/B - G.M. Counter
- ② - Dect. Eff. (%) - G.M. Counter - Filter
- ② - P/B - G.M. Counter - Filter
- ③ - Dect. Eff. (%) - S.C.
- ③ - P/B - S.C.

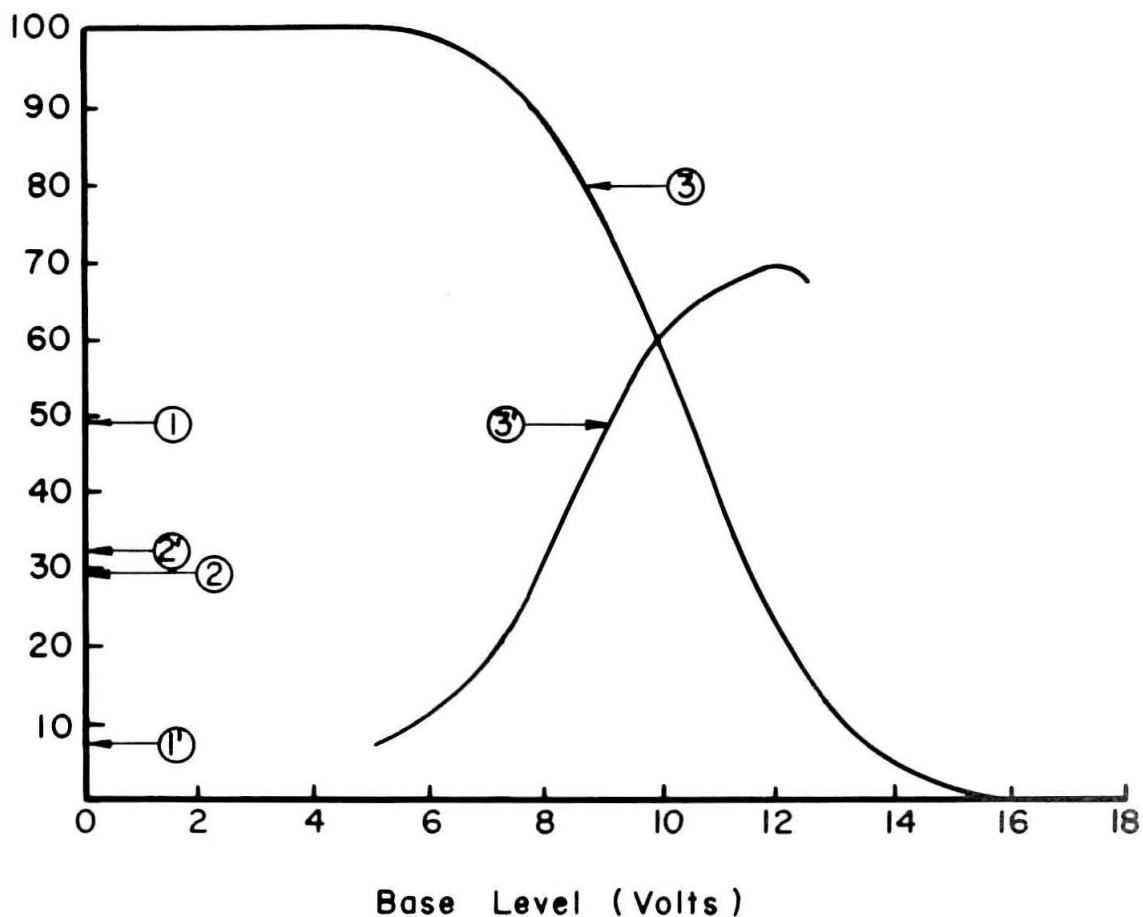


Figure 19. Comparison between a scintillation and a Geiger counter.

on a chart recorder using a Norelco Counting-Rate-Computer. The digital printer has a precision of an order of magnitude greater than the Counting-Rate-Computer and is preferred. After the data are recorded the detector moves a small angular increment and the fixed count process is repeated. The disadvantage with step scanning is that an enormous amount of time is required to scan between peaks. To eliminate this problem a diffractometer control circuit was designed to work in conjunction with the drive so that the detector would step scan in the region where a diffraction peak is located and then move continuously until it reaches the next diffraction peak. The drive is shown in Figure 20 and the schematic for the diffractometer control in Figure 21.

The drive may be briefly described as follows. A reversing synchronous motor (1) is enclosed in an argon filled stainless steel box (2) and coupled to a drive shaft (3) by a set of magnets (4). The motion is transmitted to the goniometer through a set of spur gears (5) and a multijaw coupling (6). An electromagnet (7) sealed in an argon filled box serves to uncouple the multijaw coupling and disengage the main drive shaft (8) from the motor drive. When the multijaw coupling is uncoupled, motion can be transmitted to the main shaft in distinct rotational steps by a geneva wheel (9). The geneva pin (10) is activated by a solenoid (11) which is designed so that the coil remains stationary and the plunger rotates inside of the coil. Another solenoid (12) acts as a brake on the main shaft to make sure that the geneva wheel is engaged by the geneva pin when the drive switches over from continuous

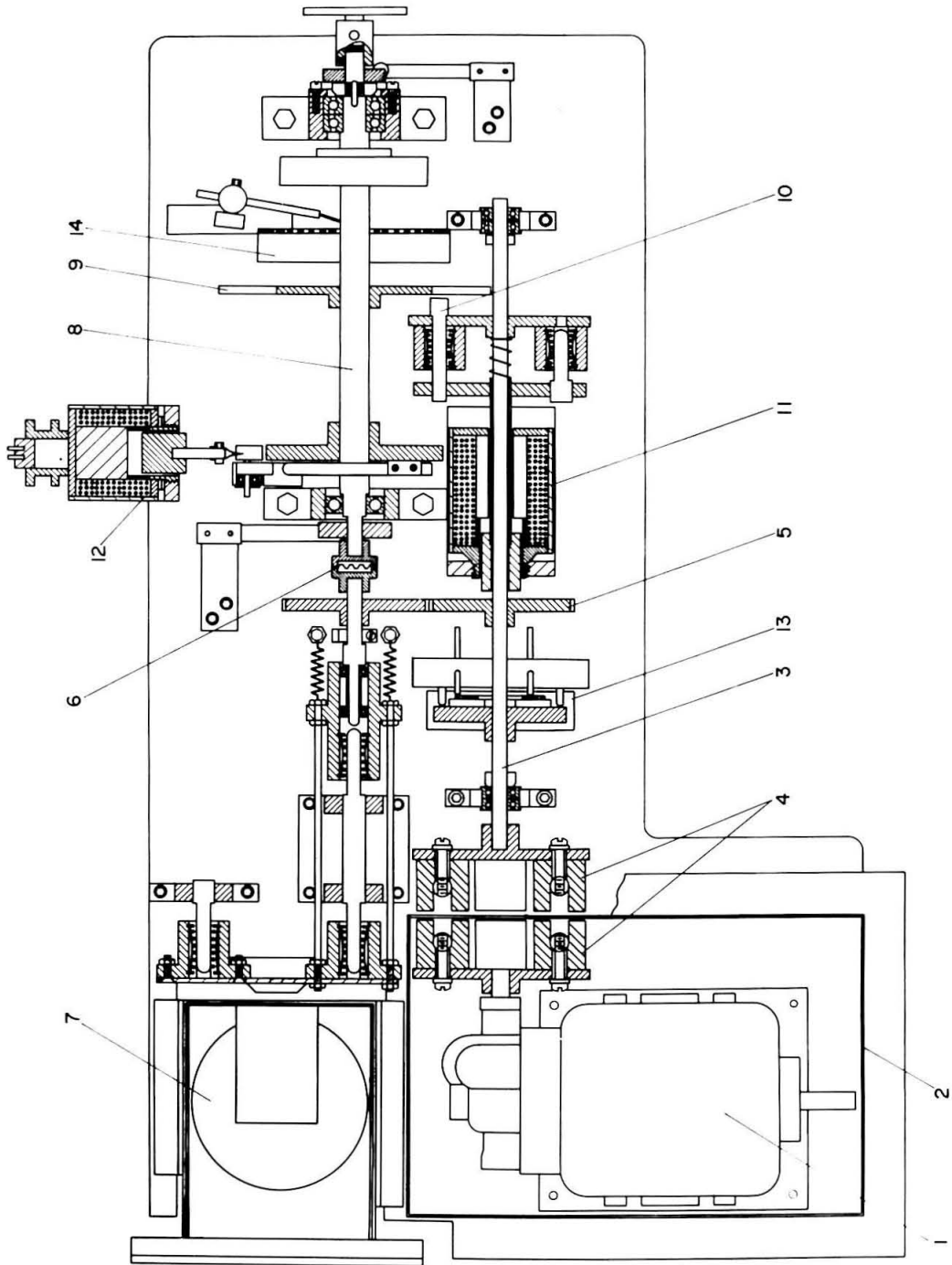


Figure 20. Schematic of diffractometer drive.

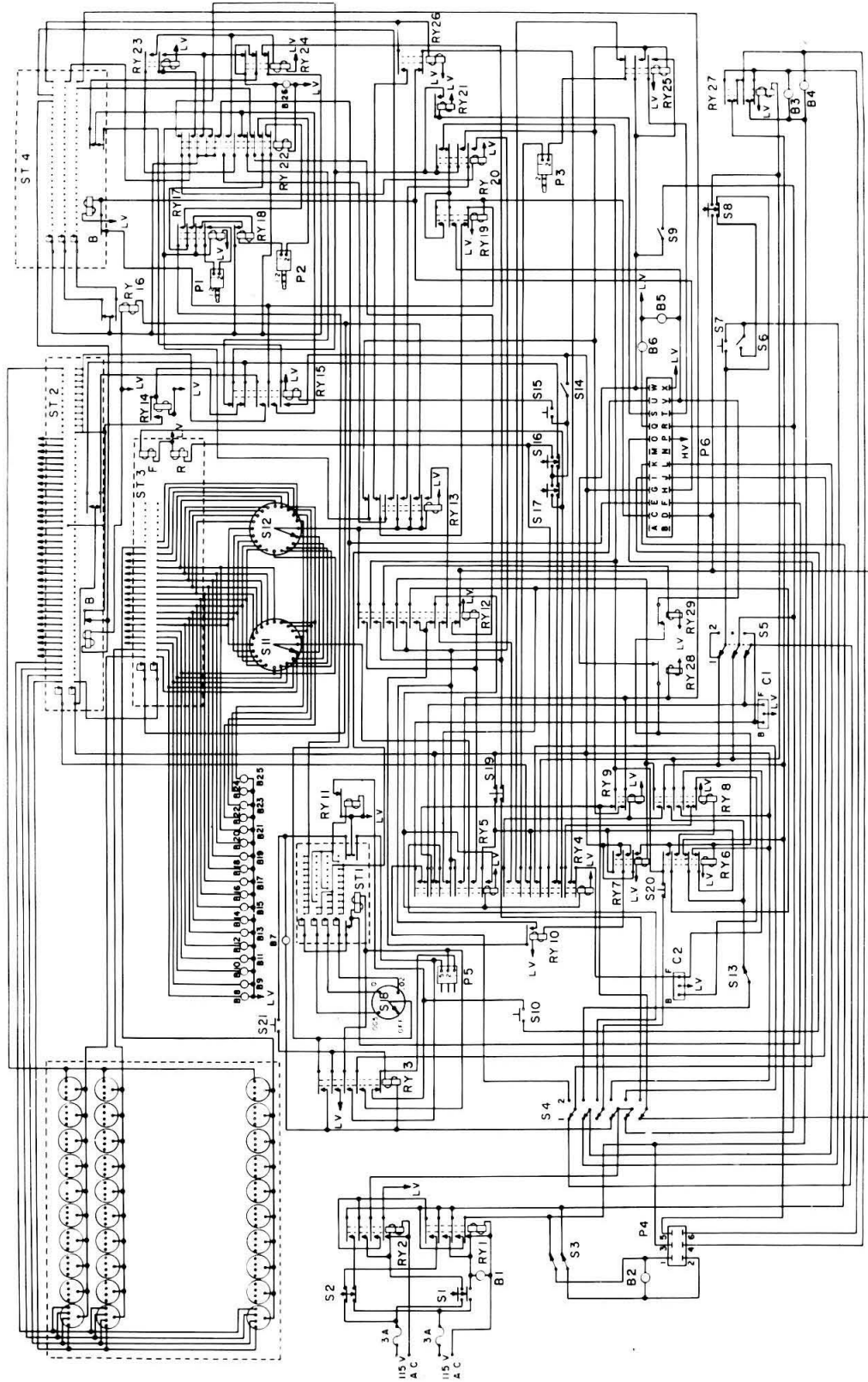


Figure 21. Schematic of diffractometer control circuit.

scanning to step scanning. A commutator switch (13) synchronizes the geneva pin solenoid with the drive shaft (3) so that the geneva pin engages and retracts at the right position. Another commutator switch (14) sends out pulses which indicate the angular position of the goniometer.

The diffractometer control circuit coordinates and controls the goniometer movements with the data recording processes. The control panel is programmed for the regions where the detector is to step scan, the angular increment to be used when step scanning, the high angle limit at which the detector is to stop and the low angle limit at which the detector is to reset itself. The regions where step scanning is to occur can be chosen to any quarter of a degree interval between 0° and 175° . The intervals are predetermined either by calculation or a continuous scan. Angular increments of 0.01° , 0.02° and 0.05° can be chosen for the step increment. Once the control panel is programmed, the experiment proceeds automatically.

3. EVALUATION OF ERRORS LIMITING THE ACCURACY OF THE DIFFRACTOMETER

The location of the center of gravity and the subsequent analysis of diffraction peaks for the accurate determination of lattice parameters are subject to both statistical and systematic errors. The statistical errors are usually treated by a least squares analysis similar to that suggested by M. U. Cohen⁽⁵³⁾. In order to apply this least squares method, it is necessary to assume a functional relationship between the systematic errors and the Bragg angle. This functional relationship requires a complete analysis of the x-ray optics. In general, a diffraction peak recorded by this parafocusing type diffractometer is asymmetrical, broadened and shifted from its theoretical 2θ value. There are two main classes of broadening -- intrinsic and instrumental. The intrinsic broadening is associated with the state of the specimen and the energy distribution of the x-rays. The natural profile of a diffraction maximum depends upon the specimen strain and distribution of crystalline size. There is no broadening due to crystalline size as long as no appreciable fraction of specimen has crystallites with a mean dimension less than 0.2 microns. This type of broadening is approximately symmetrical⁽⁵⁴⁾ and would not affect the location of the center of gravity of a diffraction peak. The broadening associated with nonuniform strain in the specimen is not symmetrical and can shift the center of gravity to higher or lower Bragg angles depending upon the state of the residual stress. Even if the residual stress is uniform, the strains associated with the different interplanar spacings will be

nonuniform due to the variation of the crystallographic elastic constants.

A characteristic line from an x-ray target is not monoenergetic, but there is a definite spread of wavelengths. This leads to an angular spread of the diffraction peak

$$\Delta\theta = \frac{\Delta\lambda}{\lambda} \tan \theta, \quad (3.1)$$

where the wavelength spread is $\Delta\lambda$. Therefore, the broadening due to wavelength spread rapidly increases as $\theta \rightarrow 90^\circ$. But again, this broadening is symmetrical with respect to the center of gravity of the wavelength spread. If the absolute values of lattice parameters are desired, care should be taken to use the wavelength corresponding to the center of gravity of a characteristic line when the locations of the diffraction peaks are represented by their center of gravity. The center of gravity of a characteristic line does not necessarily correspond to its peak value⁽⁵⁵⁾. For example, the copper $K\alpha_1$ line shows a 0.003% difference between its peak value and its center of gravity⁽⁵⁶⁾.

The parafocusing diffractometer has the following sources of instrumental broadening:

1. The use of a flat sample rather than a curved one concurrent with the focusing circle.
2. Penetration of the x-rays into the sample.
3. Vertical divergence of the x-ray beam.
4. X-ray source profile.
5. Width of the receiving slit.
6. Misalignments.

The convolutions (Faltungen) of these functions with the pure diffraction profile have been thoroughly investigated^(57, 58, 59) with the use of the superposition theorem⁽⁶⁰⁾. Only those convolutions that lead to an asymmetrical broadening, i. e., a displacement of the center of gravity, are of interest for precision lattice parameter determinations. The first two factors, the flat plate approximation and the penetration of x-rays into the sample, lead to an asymmetrical broadening and a displacement of the center of gravity towards low θ values. An analysis by A. J. C. Wilson⁽⁶¹⁾ shows that this displacement is

$$\Delta\theta = - \left[\frac{A^2}{6R^2} + \frac{1}{4\mu R} \right] \sin 2\theta + \frac{t \cos \theta}{R \left[e^{2\mu t \csc \theta} - 1 \right]} \quad (3.2)$$

where $2A$ is the illuminated length of the specimen, R is the diffractometer radius, μ is the linear absorption coefficient and t is specimen thickness. For $\mu t \gg 1$, only the first term is significant. Since the divergence of the beam limits the illuminated length of the specimen,

$$A = \frac{\alpha}{2} R \csc \theta \quad (3.3)$$

where α is the beam divergence.

The third factor, the vertical divergence of the beam, also causes an asymmetrical broadening. For this case, however, the shift of the center of gravity is towards higher θ values in the back reflections region and lower θ values in the front reflection region. An analysis by J. N. Eastabrook⁽⁵⁹⁾ shows that the center of gravity displacement is

$$\Delta\theta = - \frac{1}{48} \delta^2 \cot 2\theta \quad (3.4)$$

where δ is the overall vertical divergence angle. The derivation of the above equation is true when the vertical divergence is limited by Soller collimating slits. Although a Soller slit is employed in this instrument, the vertical divergence is mainly limited by the large ratio of the spectrometer radius to the heights of the specimen, slit and monochromator. For this instrument the vertical divergence is limited to approximately 1° .

The fourth factor, the source profile, will not shift the center of gravity if the source is symmetrical. If the source is asymmetrical, there is no shift if the deviation angle 2θ is measured from the center of gravity of the source to the center of gravity of the diffraction peak and the center of gravity of the source passes over the axis of rotation of the spectrometer. This can be shown by the following analysis. Consider a diffraction peak $f(2\theta)$ where 2θ is measured from the center of gravity of the x-ray beam about the axis of rotation of the spectrometer. The function $f(2\theta)$ is presumed to be continuous and $f(2\theta)$ and all its derivatives approach 0 as $2\theta \rightarrow \pm \infty$. If $g(\epsilon)$ is the source profile, then the convolution of the source and the diffraction peak $f(2\theta)$ is

$$F(2\theta) = \int_{-\infty}^{\infty} g(\epsilon) f(2\theta - \epsilon) d\epsilon \quad (3.5)$$

There is the auxiliary condition that

$$\int_{-\infty}^{\infty} \epsilon g(\epsilon) d\epsilon = 0. \quad (3.6)$$

The center of gravity is

$$\overline{F(z_0)} = \frac{\int_{-\infty}^{\infty} (z_0) F(z_0) d(z_0)}{\int_{-\infty}^{\infty} F(z_0) d(z_0)} \quad (3.7)$$

Substituting equation 2.13 into the above expression,

$$\overline{F(z_0)} = \frac{\int_{-\infty}^{\infty} \int_{-\infty}^{\infty} (z_0) f(z_0 - \epsilon) g(\epsilon) d\epsilon d(z_0)}{\int_{-\infty}^{\infty} \int_{-\infty}^{\infty} f(z_0 - \epsilon) g(\epsilon) d\epsilon d(z_0)} \quad (3.8)$$

Expanding $f(z_0 - \epsilon)$ in a Taylor's series

$$f(z_0 - \epsilon) = f(z_0) + \epsilon f'(z_0) + \frac{\epsilon^2}{2!} f''(z_0) + \dots, \quad (3.9)$$

equation 3.8 becomes

$$\overline{F(z_0)} = \frac{\sum_{n=0}^{\infty} \frac{1}{n!} \int_{-\infty}^{\infty} \epsilon^n g(\epsilon) d\epsilon \int_{-\infty}^{\infty} (z_0) \frac{d^n f(z_0)}{d(z_0)^n} d(z_0)}{\sum_{n=0}^{\infty} \frac{1}{n!} \int_{-\infty}^{\infty} \epsilon^n g(\epsilon) d\epsilon \int_{-\infty}^{\infty} \frac{d^n f(z_0)}{d(z_0)^n} d(z_0)} \quad (3.10)$$

Integrating by parts, integrals of the form

$$\int_{-\infty}^{\infty} (z_0) \frac{d^n f(z_0)}{d(z_0)^n} d(z_0) = 0 \quad (3.11)$$

for $n \geq 2$, and

$$\int_{-\infty}^{\infty} \frac{d^n f(2\theta)}{d(2\theta)^n} d(2\theta) = 0 \quad (3.12)$$

for $n \geq 1$.

Using equations 3.6 , 3.11 and 3.12, equation 3.10 reduces to

$$\overline{F(2\theta)} = \frac{\int_{-\infty}^{\infty} (2\theta) f(2\theta) d(2\theta)}{\int_{-\infty}^{\infty} f(2\theta) d(2\theta)} \quad (3.13)$$

or

$$\overline{F(2\theta)} = \overline{f(2\theta)}, \quad (3.14)$$

which was to be proven.

The fifth factor, the width of the receiving slit, is a symmetrical convolution and will not shift the center of gravity. However, there is the possibility that the convolution (Faltung) of a step scanning slit and the diffraction peak $f(2\theta)$ may cause a shift in the objectively determined center of gravity. For the purpose of discussion, $f(2\theta)$ is assumed to be symmetric with respect to its true center of gravity $2\theta_0$. If the center of the slit, of width W_s , coincides with $2\theta_0$ or is displaced $\beta/2$ from $2\theta_0$, where β is the step increment, then the experimentally determined center of gravity must coincide with $2\theta_0$. Simple geometrical arguments show that the maximum shift in the center of gravity occurs when the center of the slit is displaced $\pm \beta/4$ from $2\theta_0$. The order of magnitude of the maximum displacement can be estimated as follows. Let $n = 0$

denote the position of the slit when the center of the slit is displaced ϵ from $2\theta_0$. Positions of the slit corresponding to increasing values of 2θ from $2\theta_0$ are denoted by increasing positive integers and decreasing values of 2θ from $2\theta_0$ by decreasing integers. The convolution of the diffraction peak and the slit is a series of steps of intensity I_n

where,

$$I_n = \int_{2\theta_0 + \epsilon + n\beta - \frac{W_s}{2}}^{2\theta_0 + \epsilon + n\beta + \frac{W_s}{2}} f(2\theta) d(2\theta) \quad (3.15)$$

or

$$I_n \approx W_s f(2\theta_0 + \epsilon + n\beta) \quad (3.16)$$

Expanding in a Taylor's series and neglecting terms of the order of ϵ^2 , equation 3.16 becomes

$$I_n = W_s \left[f(2\theta_0 + n\beta) + \epsilon f'(2\theta_0 + n\beta) \right] \quad (3.17)$$

The center of gravity of the peak is

$$2\theta = \frac{\sum_{-n_0}^{n_0} (2\theta_0 + n\beta + \epsilon) I_n}{\sum_{-n_0}^{n_0} I_n} \quad (3.18)$$

Using equation 3.15 and the facts that

$$f(2\theta_0 + n\beta) = f(2\theta_0 - n\beta)$$

and

$$f'(2\theta_0 + n\beta) = -f'(2\theta_0 - n\beta),$$

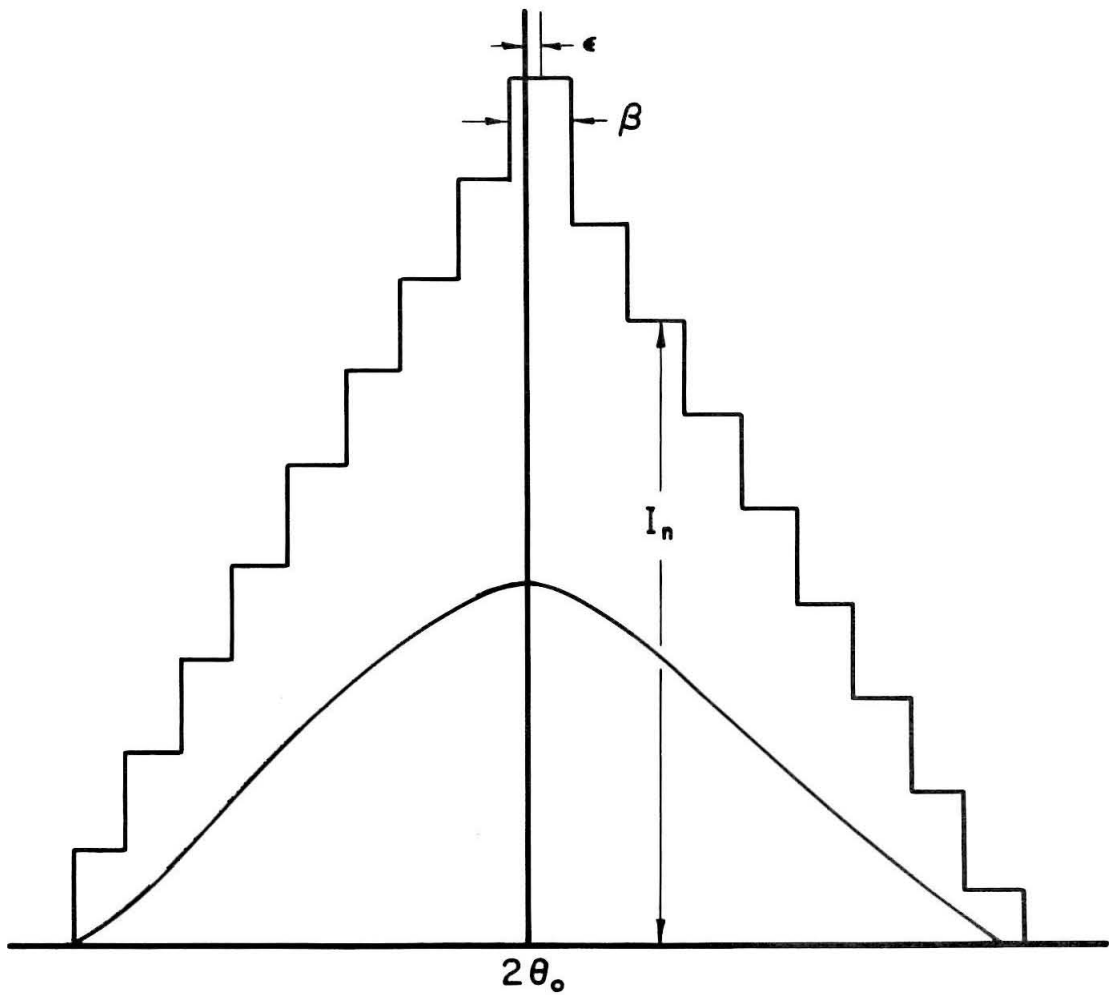


Figure 22. Convolution of a step scanning slit with a symmetrical diffraction peak.

equation 3.18 reduces to

$$\overline{\Delta 2\theta} = \epsilon \left[1 + \frac{\beta \sum_{n=1}^{n_0} n f'(2\theta_0 + n\beta)}{\frac{1}{2} f(2\theta_0) + \sum_{n=1}^{n_0} f(2\theta_0 + n\beta)} \right] \quad (3.19)$$

where $\overline{\Delta 2\theta} = (\overline{2\theta} - 2\theta_0)$. If a triangular peak is assumed, $f'(2\theta_0 + n\beta)$ is a constant

$$f(2\theta_0 + n\beta) = f(2\theta_0) \left(1 - \frac{n}{n_0 + 1} \right)$$

$$f'(2\theta_0 + n\beta) = - \frac{f(2\theta_0)}{(n_0 + 1)\beta}$$

For this case,

$$\overline{\Delta 2\theta} = \epsilon \left(\frac{1}{n_0 + 1} \right) \quad (3.20)$$

or

$$\overline{\Delta 2\theta}_{\max} = \frac{\beta}{4} \left(\frac{1}{n_0 + 1} \right) \quad (3.21)$$

Typical values which might be assumed are, $\beta = 0.05^\circ$ and $n_0 = 8$. For this case, $\overline{\Delta 2\theta}_{\max} = 0.0014^\circ = 2.4 \times 10^{-5}$ radians. For diffraction peaks where $2\theta > 45^\circ$, the maximum error in d spacings this convolution can cause is less than 1 part in 80,000.

Since the generation of x-rays is random with respect to time, the intensities measured by the step scanning procedure are subject to

the laws of statistics and the objectively determined center of gravity of a diffraction peak is subject to a statistical variation. Since the total count is fixed at each angular position, the statistics are fixed, i. e., the standard deviation in N is \sqrt{N} , and the probable error in N is $67/\sqrt{N}\%$, where N is the total number of counts accumulated. The effect the statistical variation of intensities has on the displacement of the center of gravity of a diffraction peak can be analyzed as follows. Again consider a diffraction peak $f(2\theta)$ with its center of gravity located at $2\theta_0$. The center of the scanning slit is assumed to coincide with $2\theta_0$ when the slit is in the position denoted by $n=0$. Positions of the slit corresponding to increasing values of 2θ from $2\theta_0$ are noted by position integers and decreasing values by negative integers. The stepping interval is β and the slit width is W_s . The convolution of the diffraction peak and the slit is a series of steps of intensity I_n^0 as illustrated in Figure 23.

$$I_n^0 = \int_{2\theta_0 + n\beta - \frac{W_s}{2}}^{2\theta_0 + n\beta + \frac{W_s}{2}} f(2\theta) d(2\theta) \quad (3.22)$$

$$I_n^0 \approx W_s f(2\theta_0 + n\beta) \quad (3.23)$$

Let the experimentally measured values of intensity be denoted by I_n .

$$I_n = I_n^0 (1 - k_n) \quad (3.24)$$

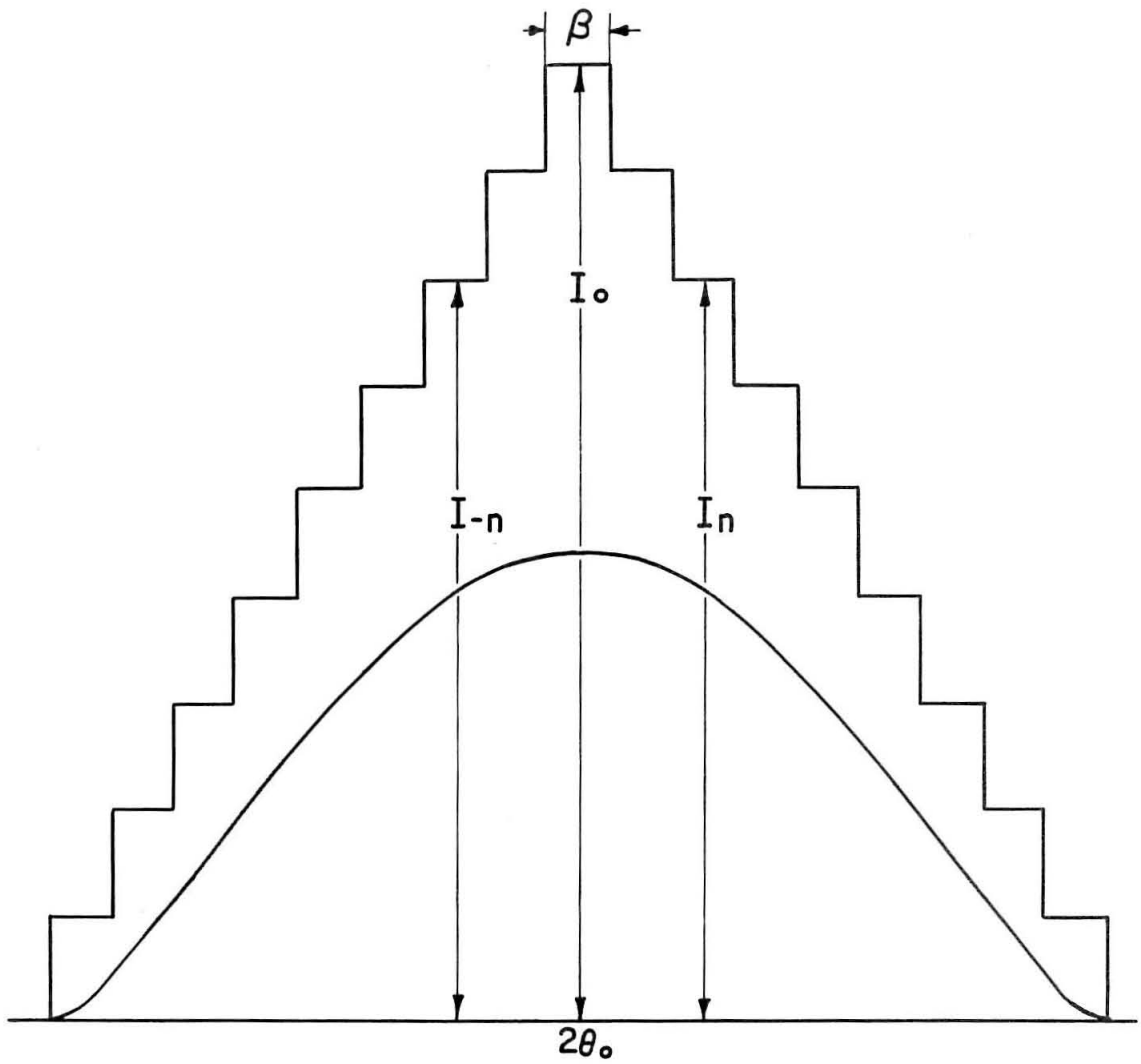


Figure 23.

where k_n is the error in the n^{th} reading and I_n^0 is the true intensity.

The center of gravity of the peak is

$$\bar{2\theta} = \frac{\sum_{-n_0}^{n_0} (2\theta_0 + n\beta) I_n}{\sum_{-n_0}^{n_0} I_n} \quad (3.25)$$

If the diffraction peak is again assumed to be symmetrical, $I_n = I_{-n}$, by using equation 3.24 and simplifying, equation 3.25 reduces to

$$2\theta = 2\theta_0 - \frac{\beta \sum_1^{n_0} n I_n^0 (k_n - k_{-n})}{I_0 + 2 \sum_1^{n_0} I_n^0} \quad (3.26)$$

Now k_n is a statistical error in intensity and should bear no relation to n . If $\pm k$ is the maximum error expected in an intensity determination, then

$$-2k \leq k_n - k_{-n} \leq 2k \quad (3.27)$$

If N counts are accumulated at each angular position, then the standard deviation of the sum or difference between any two readings is $\sqrt{2N}$. Therefore, the probable value of $k_n - k_{-n}$ is $\pm .67/\sqrt{2N}$. The probable error in 2θ , $\Delta\bar{2\theta}$, is

$$\Delta\bar{2\theta} = \pm \beta \left(\frac{.67}{\sqrt{2N}} \right) \frac{\sum_1^{n_0} n I_n^0}{I_0 + 2 \sum_1^{n_0} I_n^0} \quad (3.28)$$

To estimate the order of magnitude of $\Delta\bar{2\theta}$, a triangular diffraction peak is again assumed.

$$I_n = I_0 \left(1 - \frac{n}{n_0 + 1} \right) \quad (3.29)$$

For this case

$$\Delta\bar{2\theta} = \pm \frac{\beta n_0}{6} \left(\frac{.67}{\sqrt{2N}} \right) \left[\frac{n_0 + 2}{n_0 + 1} \right] \quad (3.30)$$

Typical values which might be assumed are

$$\beta = 0.05^\circ$$

$$n_0 = 8$$

$$N = 6400$$

For this case, $\Delta\bar{2\theta} = 4.4 \times 10^{-4} = 7.7 \times 10^{-6}$ radians. This is much too small to introduce any error in the determination of lattice parameters.

The last factor which can affect the location of the center of gravity of a diffraction peak is the diffractometer misalignments. There are six alignments that can affect the peak shape or peak location. These are:

1. The setting of the zero position.

2. The center of gravity of the beam does not pass over the axis of rotation.
3. The face of the specimen is off the axis of rotation.
4. The face of the specimen, the receiving slit and the source are not parallel.
5. The centers of the specimen, receiving slit and source are not in the same horizontal plane.
6. The 2-to-1 angular setting between the detector and the specimen is incorrect.

The zero setting of the spectrometer can be determined as accurately as the location of any diffraction peak by scanning over the primary x-ray beam and determining the location of its center of gravity. Therefore, this alignment should not introduce any systematic error. If, however, the zero position is not accurately determined, this leads to an error of $\Delta\theta = \text{constant}$.

If the center of gravity of the beam does not pass over the axis of rotation, there is again a constant displacement of the locations of the center of gravities of the diffraction peaks. Simple geometrical considerations show that this placement in θ is equal to the angle between the line joining the source to the axis of rotation and the trace of the center of gravity of the x-ray beam. The procedure used to minimize this misalignment is to find the trace to the detector of the line joining the axis of rotation with the source by independently rotating a vertical wedge about the axis of rotation. Then adjust the primary beam so its center of gravity coincides with this trace. The combination of the zero

position and the center of gravity not passing over the axis of rotation errors is $\Delta\theta = \text{constant} = \eta$. (3.31)

The displacement of a diffraction peak due to the specimen being off the axis of rotation has been theoretically⁽⁶¹⁾ and experimentally investigated⁽³⁴⁾. The peak displacement is

$$\Delta\theta = \frac{s}{R} \cos \theta \quad (3.32)$$

where s is the displacement of the specimen off the axis towards the source and R is the diffractometer radius.

Due to the fact that the above expression is linear with respect to s , a vertical rotation of the specimen with respect to the source does not displace the center of gravity of a diffraction peak, but only broadens the peak. The value of s to use in equation 3.32 is obviously the distance from specimen to the axis of rotation measured at half the specimen height. A rotation of the receiving slit relative to the source also does not displace the center of gravity but only broadens the peak.

If the centers of the source, specimen and receiving slit are not in the same horizontal plane, the vertical divergence error is increased and must be taken into account by equation 3.4. Care must be taken in this alignment since the error in θ goes as the divergence angle squared.

If the plane of the specimen does not make equal angles with the source and the detector, the center of gravity of the peak is shifted. It is reported that if the plane of the specimen makes an angle $\theta + \gamma$ with the source and the detector makes an angle of 2θ with the source, the expression⁽⁶²⁾

$$\frac{\frac{1}{3} \left[\left(\frac{a}{2} \right)^2 \sin 2\theta \right]}{\sin^2 \theta - \gamma^2} \quad (3.33)$$

should replace the first term of equation 3.2 previously derived by A. J. C. Wilson. The above expression 3.33 is incorrect. First, it is off by a factor of 1/2 as can be shown by letting $\gamma \rightarrow 0$ and next, in its derivation it neglects the penetration of the x-ray beam into the sample and the unequal lengths of irradiated specimen on each side of the axis of rotation. When these two factors are included, the following expression should be added to Wilson's equation 3.2:

$$\Delta\theta \approx \frac{5}{3} \gamma \left(\frac{a}{2} \right)^2 \cot^2 \theta + \gamma^2 \cot^2 \theta \left[\left(\frac{a}{2} \right)^2 \left(\frac{\cot \theta}{3} - \tan \theta \right) + \frac{\sin 2\theta}{4\mu R} \right] \quad (3.34)$$

This equation was derived by following Wilson's analysis and altering the x-ray path length in the specimen and the limits of integration as the sample is rotated a small angle, γ , from its prescribed angle. The sample is also assumed to be infinite in thickness ($\mu t \gg 1$) and the irradiated length of the sample is limited by the beam divergence α . For a 1° beam and γ equal to 1° , the above expression could not introduce an error of more than one part in a half million, for $\theta > 45^\circ$, in a lattice parameter determination.

Differentiating Bragg's law, the relative error in d is

$$\frac{\Delta d}{d} = -\cot \theta \Delta\theta \quad (3.35)$$

Combining equations 3.2, 3.3, 3.4, 3.31 and 3.32, equation 3.35, for $\mu t \gg 1$, reduces to

$$\frac{\Delta d}{d} = \frac{a^2}{12} \cot^2 \theta + \frac{\cos^2 \theta}{2\mu R} + \frac{\delta^2}{96} (\cot^2 \theta - 1) - \gamma \cot \theta + \frac{\alpha}{R} \cos \theta \cot \theta \quad (3.36)$$

All of these terms, except the one corresponding to the vertical divergence of the x-ray beam, tend to zero as $\theta \rightarrow 90^\circ$. The vertical divergence term increases to $-\frac{\delta^2}{96}$ as $\theta \rightarrow 90^\circ$. For this diffractometer, $\delta \approx 1^\circ$, therefore, the maximum error contribution of the vertical divergence is one part in 360,000 as $\theta \rightarrow 90^\circ$, which can be neglected. By substituting realistic values for the constants in equation 3.36, it is obvious that the last two terms, which represent misalignment, are the most significant.

There are two other corrections that should be considered. The deviation angle for a Bragg reflection is measured by the number of revolutions the worm, which drives the main gear, has been turned away from the zero position. This angle, as measured by the number of revolutions of the worm, does not necessarily correspond to the true angle the detector makes with the primary x-ray beam, due to tooth and eccentricity errors in the worm gears and eccentricity errors in the bearings. The usual procedure for calibrating worm gears is very difficult, but the mathematics involved is relatively simple. A new method involving a simple experimental procedure but an involved mathematical treatment was studied. The solution of the analytical equations of this new method could be obtained in a closed form. The procedure, which is discussed in the Appendix can be used to calibrate all the errors of a worm gear system, and should be applied after complete assembly. An interference between the detector and monochromator has made the calibration of the diffractometer worm gears impossible at the present time.

The last systematic error which does not extrapolate out as $\theta \rightarrow 90^\circ$ is the refraction correction. This correction is not simple, because it depends on shapes of the grains in the material being investigated; i. e., the correction is a function of the angle the x-ray beam makes with the grain surface normals at the points of entering and leaving the grain. For a solid flat sample, as is used in this type of instrument, with a moderately high absorption coefficient, the correction is very closely approximated by that of a flat grain surface parallel to the crystallographic reflecting planes. This correction is so small (the order of one part in 50, 000 to 100, 000), that it is only necessary to divide the apparent lattice parameter by the index of refraction⁽⁶³⁾.

$$a_{\text{corrected}} = \frac{a_{\text{observed}}}{1 - \delta} \quad (3.37)$$

where

$$\delta = \frac{Ne^2 \lambda^2}{2\pi mc^2} \quad (64) \quad (3.38)$$

N is the number of electrons per cubic centimeter, e and m are the charge and mass of the electron.

4. EXTRAPOLATION FUNCTIONS FOR THE DIFFRACTOMETER METHOD

The angular dependence of the systematic errors, neglecting the vertical divergence, can be very closely represented by a four parameter equation, i. e., equation 3.38.

$$\frac{\Delta d}{d} = A \cot^2 \theta + B \cos^2 \theta + C \cot \theta + D \cot \theta \cos \theta \quad (4.1)$$

A least squares analysis of the data, using the above equation, would require the solution of five simultaneous linear equations for a one parameter crystal or six simultaneous equations for a two parameter crystal. The work involved is not necessarily reduced by the use of an electronic computer because of the similarity of some of the terms in equation 4.1 in the region where the extrapolation is carried out ($\theta > 45^\circ$). In view of this complication, the least squares analyses previously reported in the literature have used either the $\cos^2 \theta$ or the Nelson-Riley extrapolation function for lattice parameter determinations. The justification for the use of these functions is that they closely approximate the systematic errors in the back-reflection region. (The third term of equation 4.1 was never considered.) However, the approximate extrapolation function does not extrapolate to the same value the exact function does. The error introduced by the approximate function can be analyzed in the following manner. For the purpose of discussion, assume a cubic material, therefore

$$\frac{\Delta a}{a} = \frac{\Delta d}{d} = f_0(\theta) \quad (4.2)$$

where $f_0(\theta)$ is the true systematic variation of $\Delta d/d$. Assume $\Delta d/d$ behaves as $-K_1 f_1(\theta)$, where $f_1(\theta)$ contains no arbitrary constants and

$$f_1(\theta) \rightarrow f_0(\theta) \rightarrow 0 \quad \text{as } \theta \rightarrow \frac{\pi}{2}$$

A least squares fit is now made against $-K_1 f_1(\theta)$, where the systematic error in a , Δa is determined by $f_0(\theta)$. From equation 4.2

$$a_i = a_0 [1 - f_0(\theta_i)] \quad (4.3)$$

where a_0 is the true lattice parameter and a_i is the determined lattice parameter corresponding to a diffraction peak at θ_i . The straight line to be fitted is

$$a = a_{01} [1 + K_1 f_1(\theta)] \quad (4.4)$$

where a_{01} is the extrapolated value of the lattice parameter corresponding to the extrapolation function $f_1(\theta)$. The normal equations are

$$\sum^n a_i = \sum^n a_{01} + a_{01} K_1 \sum^n f_1(\theta_i) \quad (4.5)$$

$$\sum^n a_i f_1(\theta_i) = a_{01} \sum^n f_1(\theta_i) + a_{01} K_1 \sum^n [f_1(\theta_i)]^2 \quad (4.6)$$

Substituting equation 4.3 into the above equations and solving for a_{01} , the following expression is obtained

$$a_{01} = a_0 \left\{ \frac{\sum^n 1-f_0(\theta_i) \sum^n [f_1(\theta_i)]^2 - \sum^n f_1(\theta_i) \sum^n [1-f_0(\theta_i)] f_1(\theta_i)}{n \sum^n [f_1(\theta_i)]^2 - \left[\sum^n f_1(\theta_i) \right]^2} \right\} \quad (4.7)$$

Therefore, the relative error in a_0 introduced by using the approximate function is

$$\frac{\Delta a_0}{a_0} = \frac{\sum^n f_0(\theta_i) \sum^n [f_1(\theta_i)]^2 - \sum^n f_0(\theta_i) \sum^n f_1(\theta_i)}{n \sum^n [f_1(\theta_i)]^2 - \left[\sum^n f_1(\theta_i) \right]^2} \quad (4.8)$$

Using equation 4.1 the above equation can be rewritten as

$$\frac{\Delta a_0}{a_0} = \alpha_1 A + \beta_1 B + \gamma_1 C + \delta_1 D \quad (4.9)$$

where

$$\alpha_1 = \frac{\sum^n \cot^2 \theta_i \sum^n [f_1(\theta_i)]^2 - \sum^n \cot^2 \theta_i f_1(\theta_i) \sum^n f_1(\theta_i)}{n \sum^n [f_1(\theta_i)]^2 - \left[\sum^n f_1(\theta_i) \right]^2}$$

$$\beta_1 = \frac{\sum^n \cos^2 \theta_i \sum^n [f_1(\theta_i)]^2 - \sum^n \cos^2 \theta_i f_1(\theta_i) \sum^n f_1(\theta_i)}{n \sum^n [f_1(\theta_i)]^2 - \left[\sum^n f_1(\theta_i) \right]^2}$$

$$\gamma_1 = \frac{\sum^n \cot \theta_i \sum^n [f_1(\theta_i)]^2 - \sum^n \cot \theta_i f_1(\theta_i) \sum^n f_1(\theta_i)}{n \sum^n [f_1(\theta_i)]^2 - \left[\sum^n f_1(\theta_i) \right]^2} \quad (4.10)$$

$$\delta_1 = \frac{\sum^n \cot \theta_i \cos \theta_i \sum^n [f_1(\theta_i)]^2 - \sum^n \cot \theta_i \cos \theta_i f_1(\theta_i) \sum^n f_1(\theta_i)}{n \sum^n [f_1(\theta_i)]^2 - \left[\sum^n f_1(\theta_i) \right]^2}$$

Due to the inverse trigometric behavior of θ_i and the nature of the terms in the sums, no simple method could be found for summing the above series for $f_1(\theta)$ equal to either $\cos^2 \theta$ or the Nelson-Riley function. To determine the order of magnitude and nature of the above coefficients, it was decided to evaluate them for a specific material and radiation. Lead was chosen because of its large unit cell and with copper radiation this material has a larger than usual number of back reflection lines. This would probably underestimate the usual values of α_1 , β_1 , γ_1 and δ_1 . Table 4.1 summarizes the results for values of α_1 , β_1 , γ_1 and δ_1 for angles greater than and including the corresponding 2θ value. The results are also shown graphically in Figures 24-27. The order of magnitude of $\Delta a_0/a_0$ can be determined by estimating the values of A, B, C and D in equation 4.1. Referring to equation 3.38, typical values for this diffractometer might be

$$\begin{aligned} A &= 2 \times 10^{-5} \\ B &= 1 \times 10^{-5} \\ C &= \pm 1 \times 10^{-4} \\ D &= \pm 1 \times 10^{-4} \end{aligned} \tag{4.11}$$

The values for B and D would probably be higher for commercially available diffractometers. Using the above values, Table 4.2 shows

Table 4.1

hkl	2θ	cos ² θ				1/2 ($\frac{\cos^2 \theta}{\sin \theta} + \frac{\cos^2 \theta}{\theta}$)			
		α ₁	β ₁	γ ₁	δ ₁	α ₁	β ₁	γ ₁	δ ₁
620	159.63	--	-	--	--	--	--	--	--
600	442	138.07	0	0.114	-0.002	-0.000	0.004	0.122	0.002
531	134.07	-0.006	0	0.117	-0.003	-0.001	0.004	0.126	0.002
440	123.37	-0.015	0	0.131	-0.007	-0.004	0.009	0.149	0.003
511,333	107.93	-0.045	0	0.148	-0.020	-0.014	0.021	0.186	0.006
422	99.35	-0.070	0	0.152	-0.030	-0.023	0.029	0.203	0.007
420	88.20	-0.119	0	0.150	-0.047	-0.041	0.042	0.222	0.010
331	85.43	-0.146	0	0.147	-0.057	-0.051	0.048	0.229	0.011
400	77.00	-0.203	0	0.136	-0.076	-0.074	0.060	0.241	0.012
222	65.23	-0.345	0	0.108	-0.118	-0.139	0.086	0.259	0.015
311	62.13	-0.451	0	0.086	-0.149	-0.178	0.100	0.268	0.017
220	52.23	-0.681	0	0.038	-0.207	-0.284	0.128	0.280	0.019
200	36.13	-1.512	0	-0.110	-0.372	-0.739	0.200	0.299	0.025
111	31.27	-2.397	0	-0.252	-0.526	-1.070	0.236	0.304	0.026

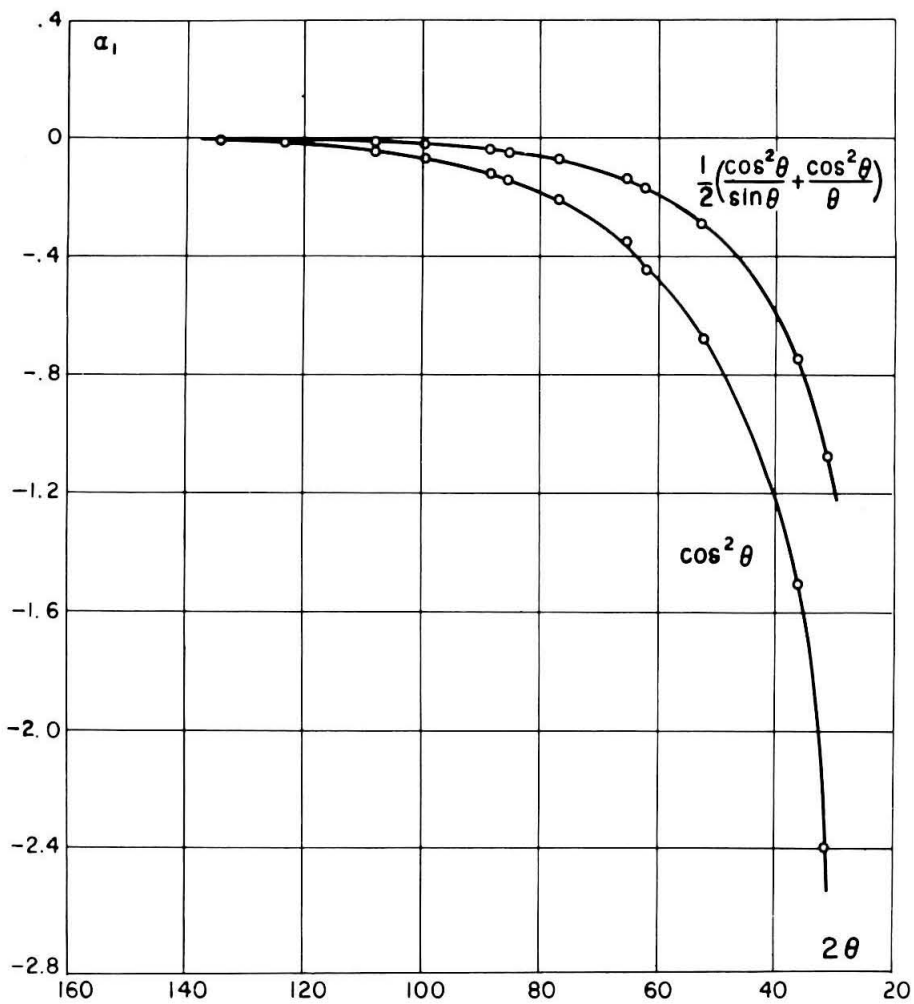


Figure 24.

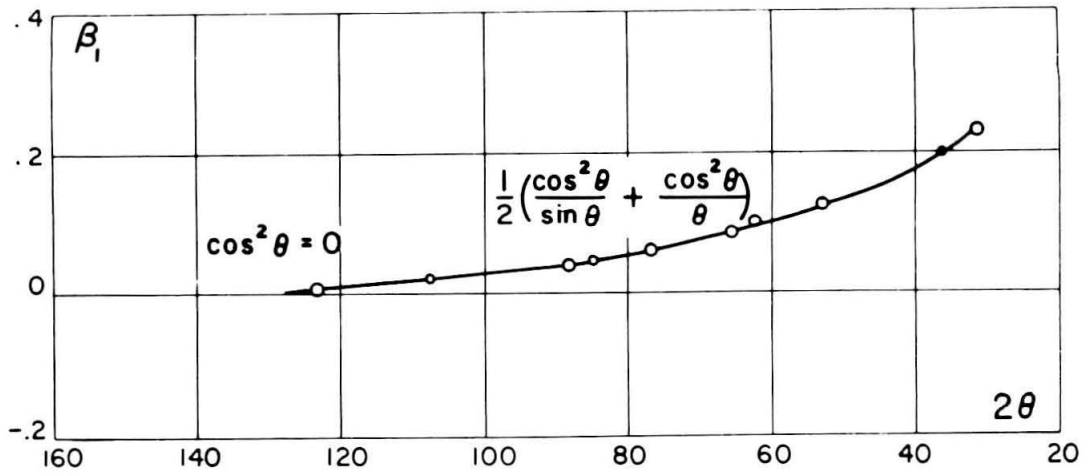


Figure 25.

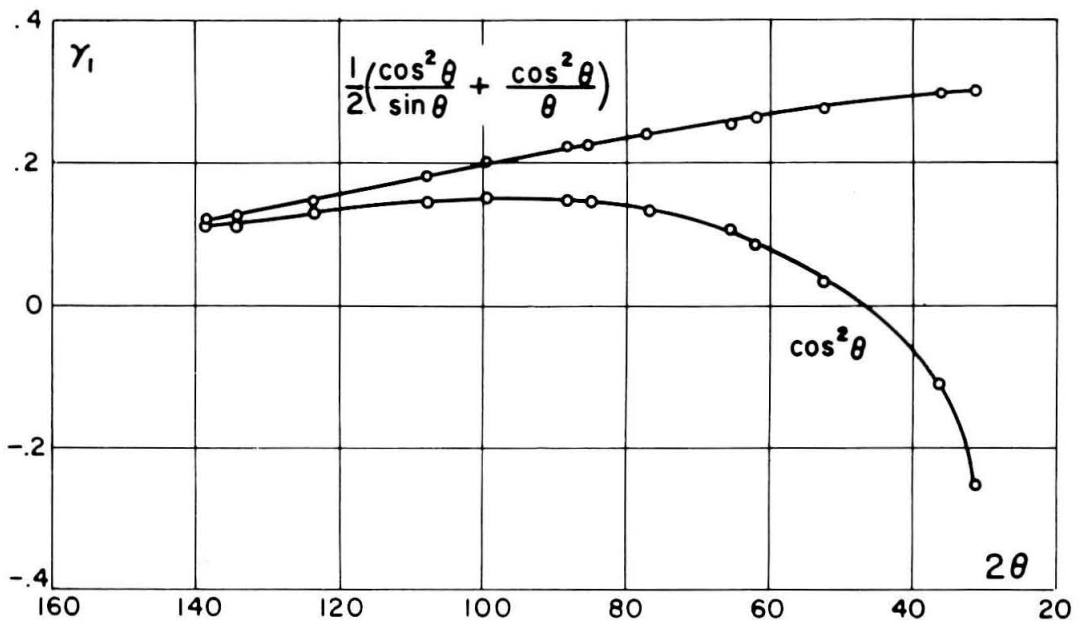


Figure 26.

the maximum relative error in a_0 when $\cos^2 \theta$ or the Nelson-Riley function is used instead of the exact function (assuming the equation 4.1 represents the nature of the exact function).

Table 4.2

$$\Delta a_0 / a_0 \times 10^5$$

2θ	$\cos^2 \theta$	$1/2 \left(\frac{\cos^2 \theta}{\sin \theta} + \frac{\cos^2 \theta}{\theta} \right)$
159.63	--	--
138.07	-1.17	-1.23
134.07	-1.21	-1.28
123.37	-1.41	-1.52
107.93	-1.77	-1.93
99.35	-1.96	-2.12
88.20	-2.21	-2.35
85.43	-2.33	-2.45
77.00	-2.53	-2.62
65.23	-2.95	-2.93
62.13	-3.25	-3.10
52.23	-3.81	-3.43
36.13	-5.64	-4.52
31.27	-7.53	-5.20

These results are shown graphically in Figure 28. Several other functions and combinations of functions of θ , such as $\cot^2 \theta$, $\cot \theta \cos \theta$, $\cot \theta + \cot \theta \cos \theta$, $(\cot \theta + \cos \theta)^2$, etc., were tried to see if a better one could be found. Many of these gave approximately the

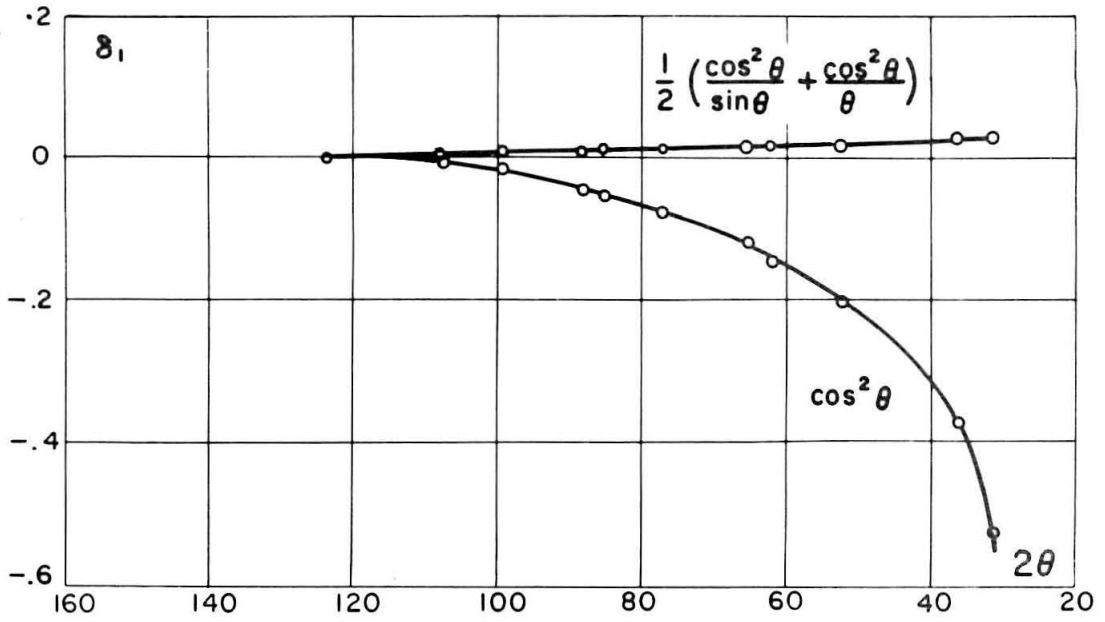


Figure 27.

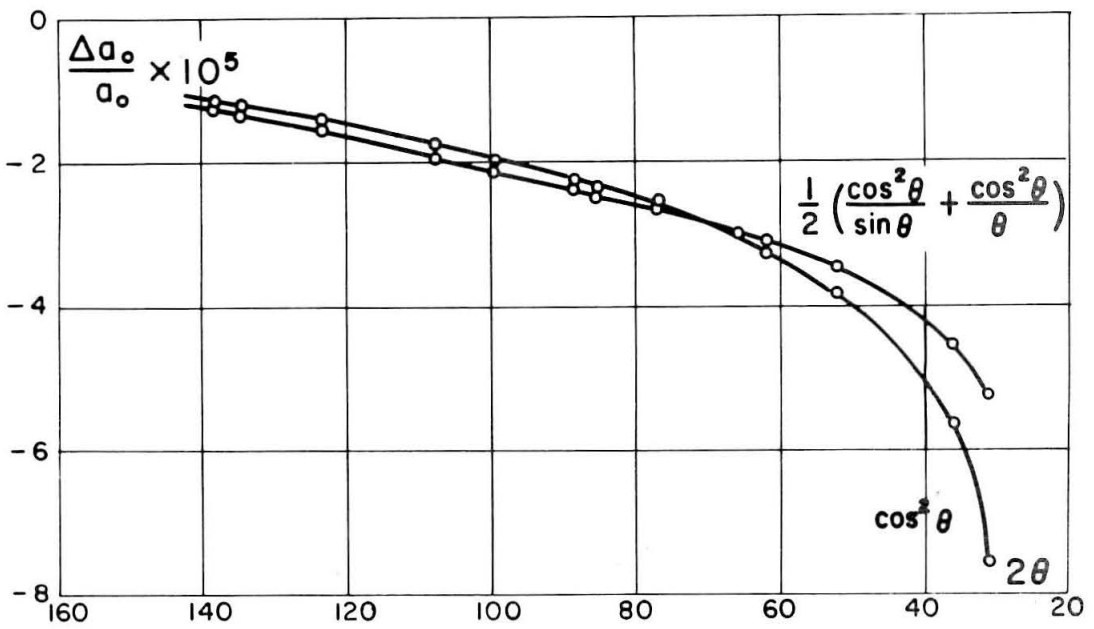


Figure 28. Relative error for the approximate extrapolated value of a_0 as a function of the included diffraction lines.

same results as the $\cos^2 \theta$ and the Nelson-Riley function. However, none could be found which would appreciably improve the relative error in the extrapolated value of a .

A remaining possibility to improve the nature of the extrapolation function would be to make it a two parameter function rather than a one parameter function. For this case $\Delta d/d$ is assumed to behave as

$$\frac{\Delta d}{d} = -K_2 f_2(\theta) - K_3 f_3(\theta) \quad (4.12)$$

Again $f_2(\theta)$ and $f_3(\theta)$ contain no arbitrary constants and

$$f_2(\theta) \rightarrow f_3(\theta) \rightarrow f_0(\theta) \rightarrow 0 \quad \text{as } \theta \rightarrow \frac{\pi}{2}$$

The linear regression to be fitted is

$$a = a_{02} \left[1 + K_2 f_2(\theta) + K_3 f_3(\theta) \right] \quad (4.13)$$

The normal equations are

$$\begin{aligned} \sum_{i=1}^n a_i &= n a_{02} + a_{02} K_2 \sum_{i=1}^n f_2(\theta_i) + a_{02} K_3 \sum_{i=1}^n f_3(\theta_i) \\ \sum_{i=1}^n a_i f_2(\theta_i) &= a_{02} \sum_{i=1}^n f_2(\theta_i) + a_{02} K_2 \sum_{i=1}^n [f_2(\theta_i)]^2 + a_{02} K_3 \sum_{i=1}^n f_2(\theta_i) f_3(\theta_i) \\ \sum_{i=1}^n a_i f_3(\theta_i) &= a_{02} \sum_{i=1}^n f_3(\theta_i) + a_{02} K_2 \sum_{i=1}^n f_2(\theta_i) f_3(\theta_i) + a_{02} K_3 \sum_{i=1}^n [f_3(\theta_i)]^2 \end{aligned} \quad (4.14)$$

Substituting equation 4.3 into the above equation and solving for a_{02} , the following expression is obtained:

$$a_{02} = a_0 \left[1 - \frac{\gamma \sum_{i=1}^n f_0(\theta_i) - \eta \sum_{i=1}^n f_0(\theta_i) f_2(\theta_i) + \kappa \sum_{i=1}^n f_0(\theta_i) f_3(\theta_i)}{n\gamma - \eta \sum_{i=1}^n f_2(\theta_i) + \kappa \sum_{i=1}^n f_3(\theta_i)} \right] \quad (4.15)$$

where

$$\begin{aligned} \gamma &= \sum_{i=1}^n [f_2(\theta_i)]^2 \sum_{i=1}^n [f_3(\theta_i)]^2 - \left[\sum_{i=1}^n f_2(\theta_i) f_3(\theta_i) \right]^2 \\ \eta &= \sum_{i=1}^n f_2(\theta_i) \sum_{i=1}^n [f_3(\theta_i)]^2 - \sum_{i=1}^n f_2(\theta_i) f_3(\theta_i) \sum_{i=1}^n f_3(\theta_i) \\ \kappa &= \sum_{i=1}^n f_2(\theta_i) f_3(\theta_i) \sum_{i=1}^n f_2(\theta_i) - \sum_{i=1}^n [f_2(\theta_i)]^2 \sum_{i=1}^n f_3(\theta_i) \end{aligned} \quad (4.16)$$

From equation 4.15 it follows that the relative error in the extrapolated value of the lattice parameter introduced by using the above linear regression is

$$\frac{\Delta a_0}{a_0} = \frac{\gamma \sum_{i=1}^n f_0(\theta_i) - \eta \sum_{i=1}^n f_0(\theta_i) f_2(\theta_i) + \kappa \sum_{i=1}^n f_0(\theta_i) f_3(\theta_i)}{n\gamma - \eta \sum_{i=1}^n f_2(\theta_i) + \kappa \sum_{i=1}^n f_3(\theta_i)} \quad (4.17)$$

Assuming equation 4.1 represents the exact nature of the systematic errors, equation 4.17 can be written as:

$$\frac{\Delta a_0}{a_0} = \alpha_2 A + \beta_2 B + \gamma_2 C + \delta_2 D \quad (4.18)$$

where

$$a_2 = \frac{\gamma \sum \cot^2 \theta_i - \eta \sum \cot^2 \theta_i f_2(\theta_i) + \kappa \sum \cot^2 \theta_i f_3(\theta_i)}{n\gamma - \eta \sum f_2(\theta_i) + \kappa \sum f_3(\theta_i)}$$

$$b_2 = \frac{\gamma \sum \cos^2 \theta_i - \eta \sum \cos^2 \theta_i f_2(\theta_i) + \kappa \sum \cos^2 \theta_i f_3(\theta_i)}{n\gamma - \eta \sum f_2(\theta_i) + \kappa \sum f_3(\theta_i)}$$

(4.19)

$$\gamma_2 = \frac{\gamma \sum \cot \theta_i - \eta \sum \cot \theta_i f_2(\theta_i) + \kappa \sum \cot \theta_i f_3(\theta_i)}{n\gamma - \eta \sum f_2(\theta_i) + \kappa \sum f_3(\theta_i)}$$

$$\delta_2 = \frac{\gamma \sum \cot \theta_i \cos \theta_i - \eta \sum \cot \theta_i \cos \theta_i f_2(\theta_i) + \kappa \sum \cot \theta_i \cos \theta_i f_3(\theta_i)}{n\gamma - \eta \sum f_2(\theta_i) + \kappa \sum f_3(\theta_i)}$$

After careful scrutinization of the behavior of the above coefficients with judiciously chosen values of $f_2(\theta)$ and $f_3(\theta)$, three extrapolation functions were found which would yield much better results than either $\cos^2 \theta$ or the Nelson-Riley function. These are

$$F_1(\theta) = -K_2 \cot \theta - K_3 \cot \theta \cos \theta \quad (4.20)$$

$$F_2(\theta) = -K_2 (\cot^2 \theta + \cos^2 \theta) - K_3 (\cot \theta + \cot \theta \cos \theta) \quad (4.21)$$

$$F_3(\theta) = -K_2 \cot \theta - K_3 \cot^2 \theta \quad (4.22)$$

Although all three of these are better than the single parameter functions previously discussed, the best one to use is really governed

by the geometry of the diffractometer. By examining the values of α_2 , β_2 , γ_2 and δ_2 listed in Table 4.3 for the above functions, it can be seen that $F_1(\theta)$ is best for the long radius and small beam angle diffractometer (which is the case for this instrument), while $F_3(\theta)$ is best for the large beam angle diffractometer ($\alpha > 2^\circ$). $F_2(\theta)$ is a compromise function which yields good results for both types of diffractometers and is probably best for the general case. Figures 29-32 show the dependence of the coefficients α_2 , β_2 , γ_2 and δ_2 on including all reflections above a certain Bragg angle. Figure 33 shows the maximum relative error in lattice parameter $\Delta a_0/a_0$ assuming the values in equation 4.11. For comparison the previously determined values for $\cos^2 \theta$ and the Nelson-Riley function are plotted on the corresponding graphs.

Table 4.3

20	$F_1(\theta) = -K_2 \cot \theta - K_3 \cot \theta \cos \theta$				$F_2(\theta) = -K_2 (\cot^2 \theta + \cos^2 \theta) - K_3 (\cot \theta + \cot \theta \cos \theta)$				$F_3(\theta) = -K_2 \cot \theta - K_3 \cot^2 \theta$			
	α_2	β_2	γ_2	δ_2	α_2	β_2	γ_2	δ_2	α_2	β_2	γ_2	δ_2
159.63	-	-	0	0	-	-	-	-	0	-	0	-
138.07	-	-	0	0	-	-	-	-	0	-	0	-
134.07	-	-	0	0	-	-	-	-	0	-	0	-
123.37	0.026	-0.011	0	0	-	-	-	-	0	-	0	-0.004
107.93	0.042	-0.029	0	0	0.031	-0.031	0.005	-0.005	0	-0.042	0	-0.024
99.35	0.061	-0.037	0	0	0.040	-0.040	0.008	-0.008	0	-0.052	0	-0.033
88.20	0.104	-0.060	0	0	0.060	-0.060	0.018	-0.018	0	-0.074	0	-0.050
85.43	0.123	-0.067	0	0	0.066	-0.066	0.022	-0.022	0	-0.080	0	-0.056
77.00	0.186	-0.089	0	0	0.080	-0.080	0.034	-0.034	0	-0.098	0	-0.075
65.23	0.357	-0.139	0	0	0.094	-0.094	0.058	-0.058	0	-0.123	0	-0.109
62.13	0.439	-0.160	0	0	0.095	-0.095	0.063	-0.063	0	-0.126	0	-0.116
52.23	0.683	-0.209	0	0	0.085	-0.085	0.083	-0.083	0	-0.121	0	-0.125
36.13	1.496	-0.311	0	0	0.040	-0.040	0.111	-0.111	0	-0.117	0	-0.205
31.27	1.899	-0.349	0	0	0.018	-0.018	0.120	-0.120	0	-0.102	0	-0.221

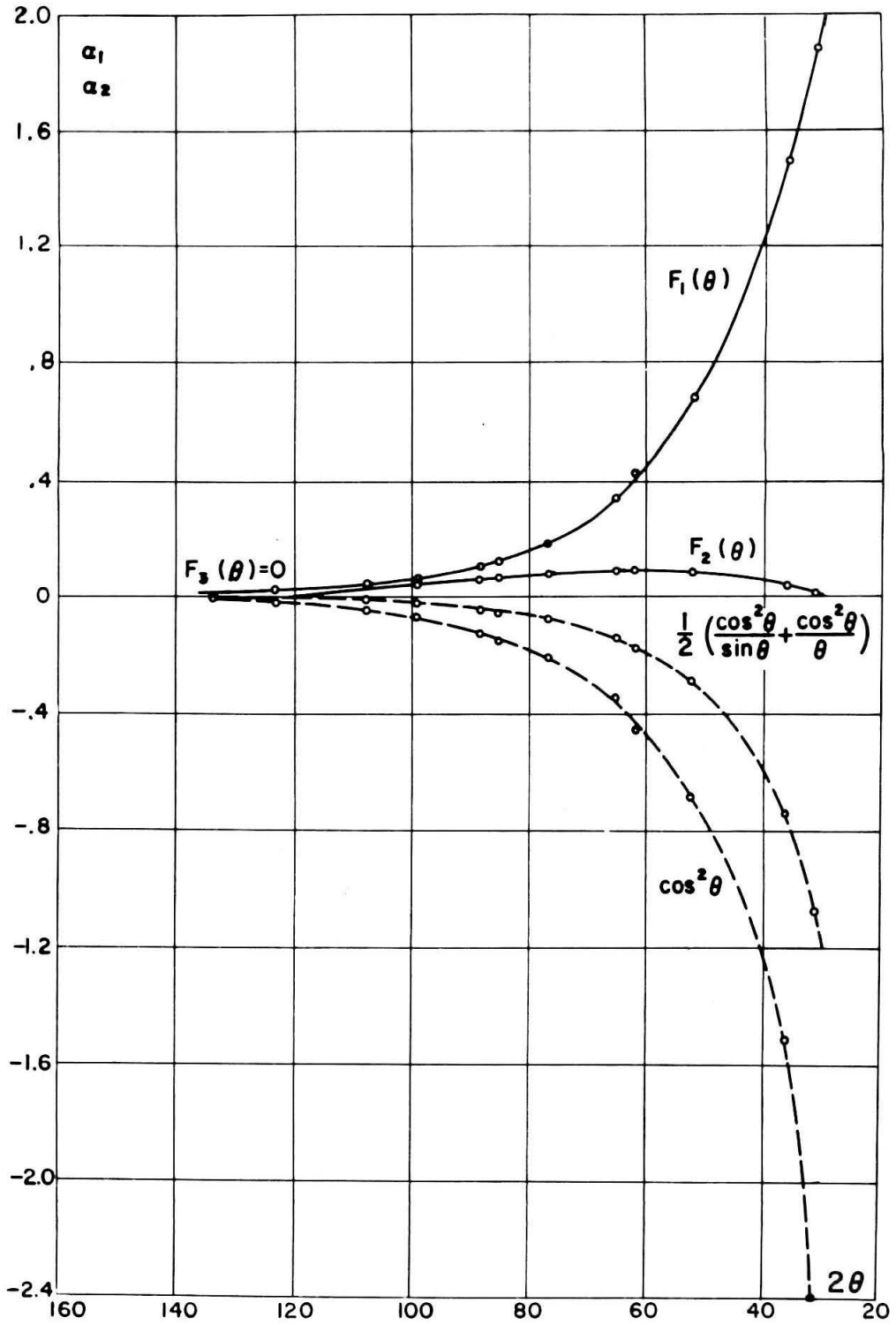


Figure 29.

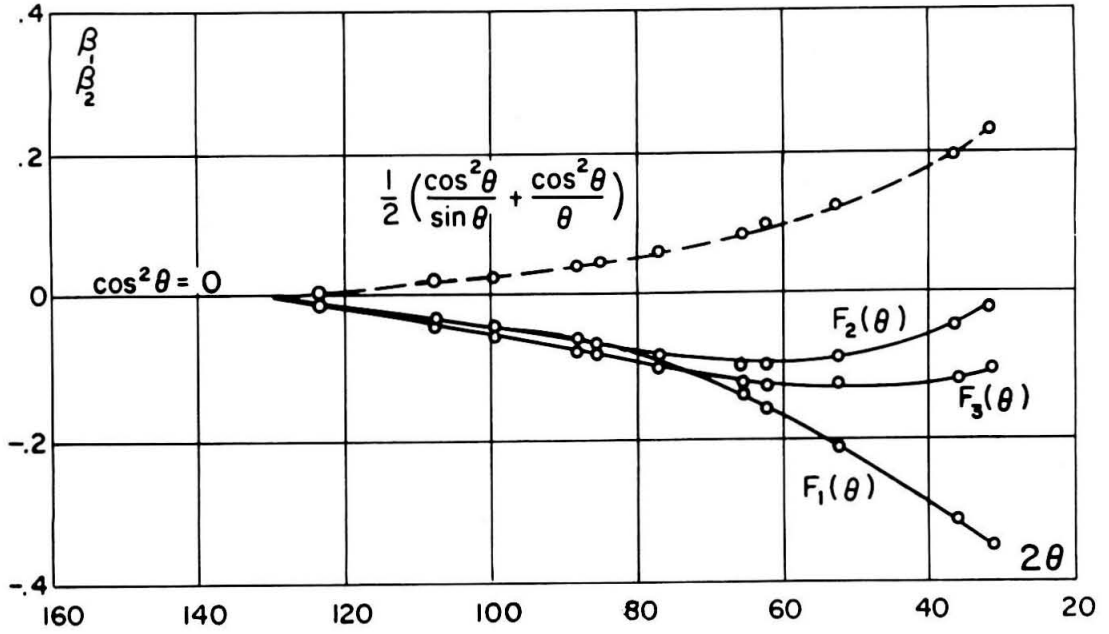


Figure 30.

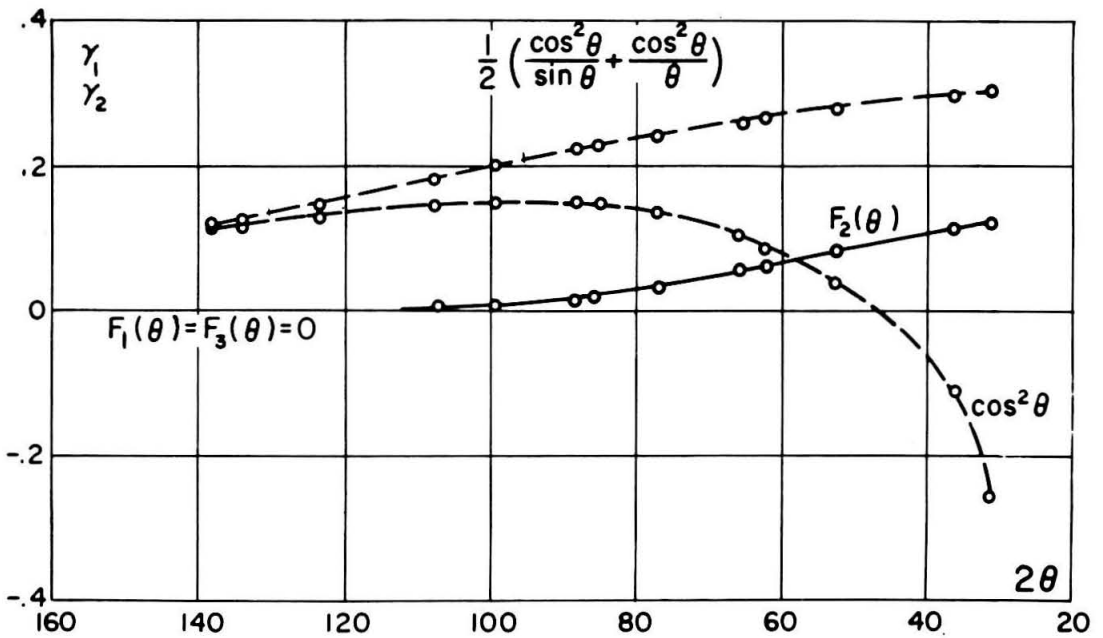


Figure 31.

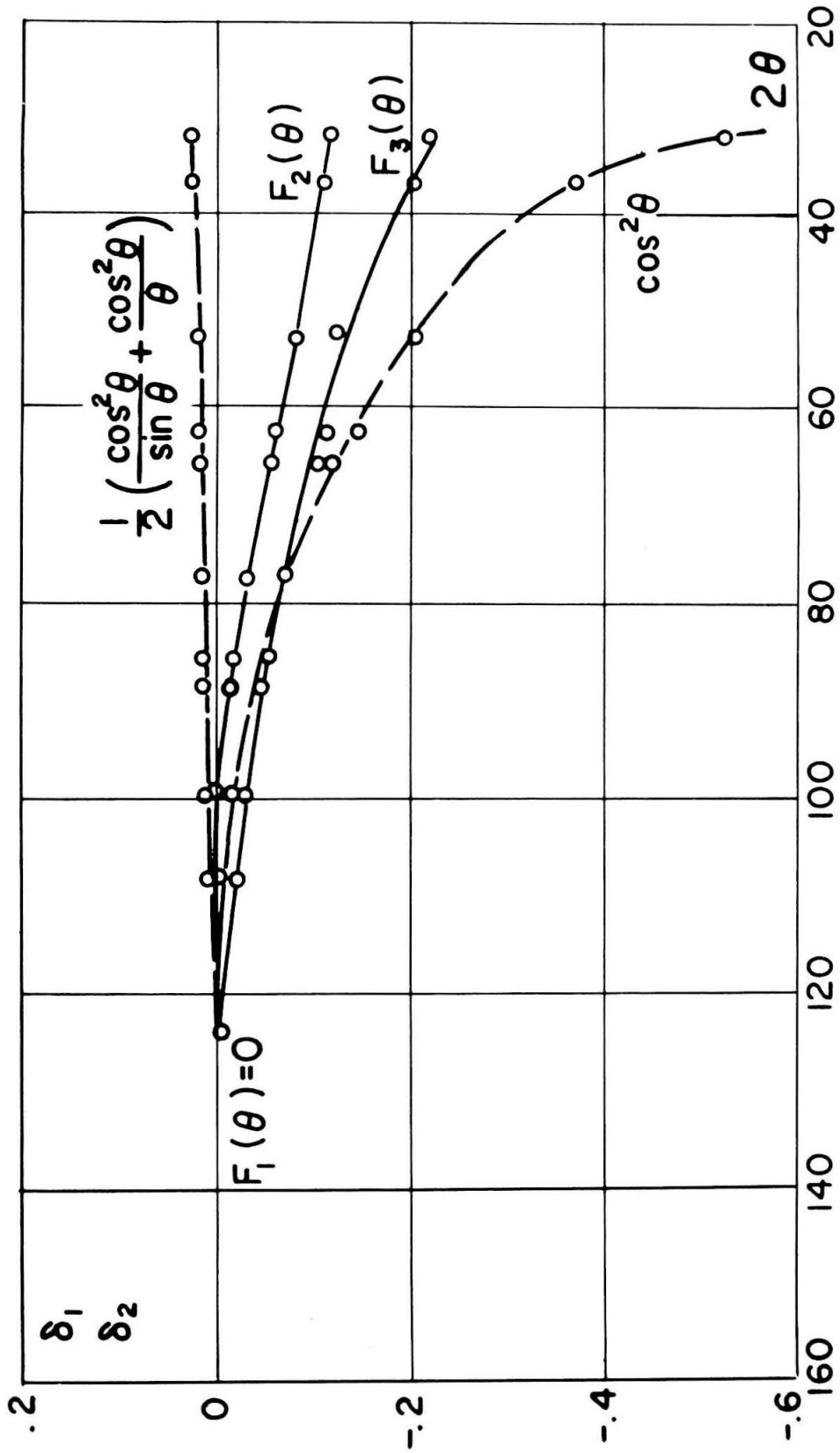


Figure 32.

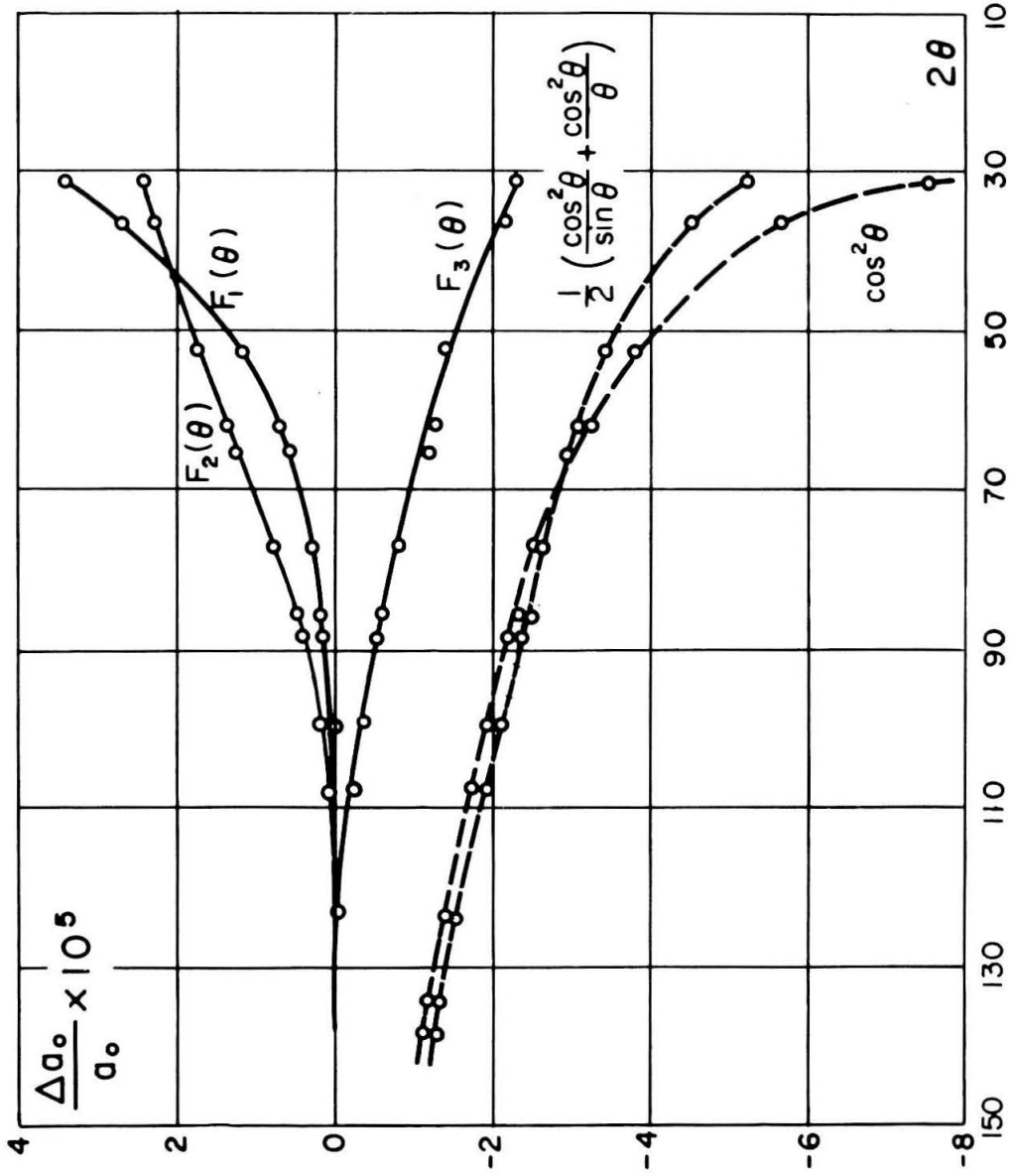


Figure 33. Relative error for the approximate extrapolated value of a_0 as a function of the included diffraction lines.

5. EXPERIMENTAL PROCEDURE AND RESULTS

The performance of the diffractometer and its associated electronics were checked by measuring the thermal expansion of chemically pure silver. The location of the seven highest angle diffraction peaks, between room temperature and 420°C , were measured by pre-count step scanning. The results of the experiments showed that the systematic errors of the diffractometer are so small, or cancel one another out, that almost any reasonable extrapolation function can be used for determining lattice parameters.

A typical extrapolation of the five highest angle reflections, with the sample at 420°C , against the Nelson-Riley function is shown in Figure 34. The straight line was determined by a least square fit using Cohen's method. The standard deviation from this line is 0.00015A , which means the probable error is one part in forty thousand. The lattice parameter at 15.6°C was determined to be $4.0853 \pm .0001\text{A}$. The measurement of Owen and Roberts⁽⁵¹⁾ on 99.95% Ag at 18°C gives a lattice parameter of 4.0854A , which is in excellent agreement with the results of this experiment. The lattice parameters that are reported in this thesis have assumed that the wavelength of tungsten $\text{L}\alpha_1$ is 1.47635A , the conversion factor from kx units to angstroms is 1.00202 and all parameters are corrected for refraction.

The results of this experiment on silver can be used to calibrate the thermocouple by cross-plotting the lattice parameter versus temperature curve of this investigation with that of previous in-

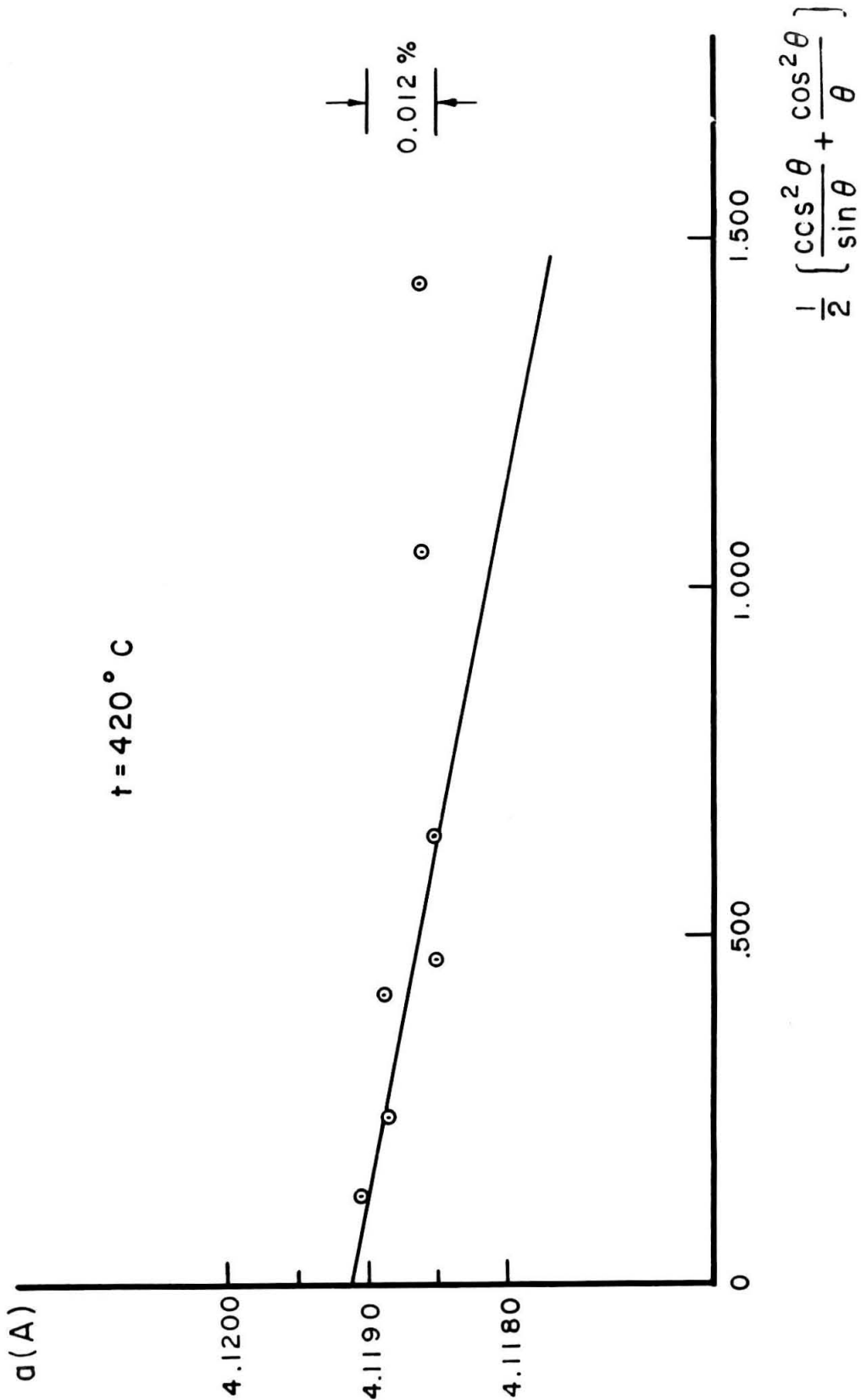


Figure 34. Extrapolation of the lattice parameter of silver (420°C) against the Nelson-Riley function.

investigators (65, 66, 67). The calibration curve is shown in Figure 35. Considering the scatter of the previous investigation data and the accuracy to which the temperature was measured, the temperature as determined from this calibration chart is within 5°C of the true temperature for temperatures less than 500°C . The extrapolation of the curve to higher temperatures is subject to the objection that the radiation-conduction heat balance may change at the higher temperatures.

The next experiment was performed on remelted iodide titanium. The material was obtained from U.S. Army Ordnance Corps, Watertown Arsenal Laboratories in the form of hot rolled plates about 4 mm thick. Small trapezoids were cut from these plates and milled on both sides to about a thickness of 2.5 mm. This insured that at least twice the depth of contamination, as determined by hardness tests, was removed. The specimens were then sealed in a quartz tube filled with helium. Care was taken to insure that the specimens did not touch the quartz and rested only on auxiliary specimen supports made of titanium. A "getter" was heated inside the tube to capture the remaining oxygen and nitrogen prior to annealing. The trapezoidal specimens were annealed 50°C above the $\alpha \rightarrow \beta$ transformation temperature for fifteen minutes and then quickly returned to room temperature. They were then riveted to a titanium specimen wheel with titanium rivets. The segments on the front face of the specimen wheel were made coplanar and normal to the wheel axis by grinding. The cold worked layer, produced by the grinding, was removed by an acid etch of equal parts of nitric acid, hydrofluoric acid and glycerin.

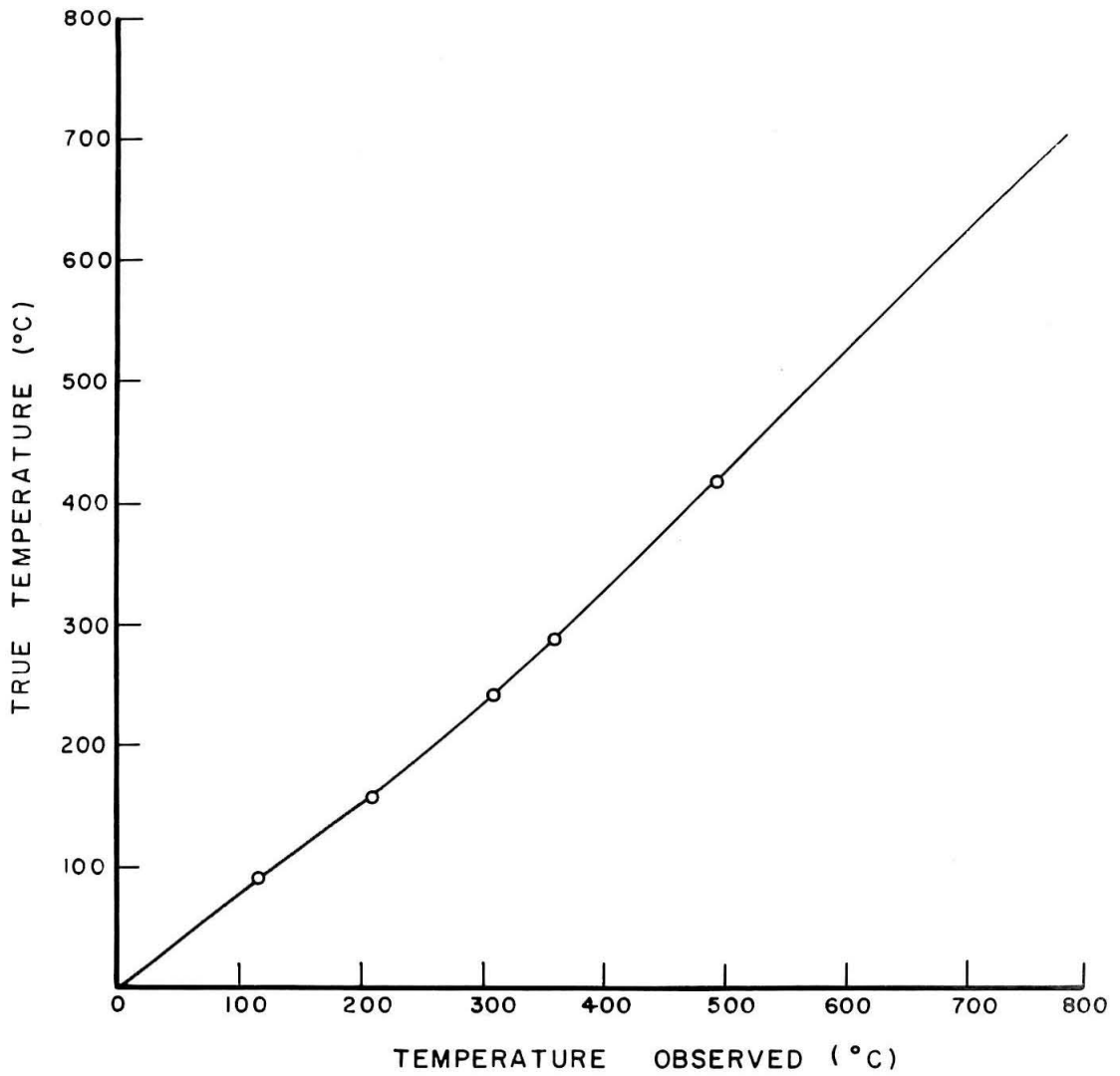


Figure 35. Calibration of the Pt-Pt 10% Rh thermocouple.

The specimen was then mounted in the diffractometer furnace and the vacuum system and argon purifying system activated. A preliminary lattice parameter measurement was made at room temperature. After three days of pumping, the titanium "getter" was heated and the specimen was then heated to 700°C for two hours as a final anneal. The room temperature diffraction pattern taken after this anneal showed no change in lattice parameters and were in good agreement with those measured by previous investigators^(68, 69, 70). The comparison between the room temperature parameters of titanium are tabulated in Table 5.1.

Table 5.1

Investigator	a (A)	c (A)	c/a
Present Investigator (20°C)	2.9496 ± 1	4.6822 ± 1	1.5874
Clark ⁽⁶⁸⁾ (25°C)	2.9504 ± 3	4.6833 ± 3	1.5873
Greiner and Ellis ⁽⁶⁹⁾ (25°C)	2.9450 ± 4	4.6845 ± 7	1.5907
Szanto ⁽⁷⁰⁾ (25°C)	2.9506 ± 5	4.6788 ± 7	1.5857

Eight of the best diffraction peaks were chosen for step scanning to shorten the data-taking time at a given temperature. The time required to complete a single temperature run was two days. The temperature variation of the lattice parameters was determined to 650°C where unfortunately a power failure during this experiment resulted in air leaking back through the pumping system and contaminating the specimen. However, enough data were taken to show

that the c/a parameter for titanium rapidly increases as the transformation temperature is approached. The results are summarized in Table 5.2 and Figure 36.

Table 5.2

Temperature (°C)	a (Å)	c (Å)	c/a
20	2.9496 ± 1	4.6822 ± 2	1.5874
113	2.9526 ± 3	4.6882 ± 5	1.5878
250	2.9558 ± 3	4.6945 ± 5	1.5882
383	2.9593 ± 3	4.7012 ± 5	1.5886
501	2.9634 ± 4	4.7102 ± 7	1.5894
647	2.9670 ± 12	4.7314 ± 20	1.5941

The coefficients of thermal expansion perpendicular and parallel to the c-axis between 0 and 400°C are $9.41 \times 10^{-6}/^{\circ}\text{C}$ and $11.18 \times 10^{-6}/^{\circ}\text{C}$ respectively. For a random polycrystalline sample, the mean linear expansion coefficient is

$$\bar{\alpha} = \frac{2\alpha_a + \alpha_c}{3}$$

or

$$\bar{\alpha} = 10.0 \times 10^{-6}/^{\circ}\text{C}$$

The x-ray thermal expansion coefficients as determined by Spreadborough and Christian⁽³⁸⁾, and Berry and Raynor⁽³⁹⁾ are $\alpha_a = 9.55 \times 10^{-6}/^{\circ}\text{C}$, $\alpha_c = 10.65 \times 10^{-6}/^{\circ}\text{C}$, $\bar{\alpha} = 9.78 \times 10^{-6}$ and $\alpha_a = 11.25 \times 10^{-6}/^{\circ}\text{C}$, $\alpha_c = 10.19 \times 10^{-6}/^{\circ}\text{C}$ and $\bar{\alpha} = 11.25 \times 10^{-6}/^{\circ}\text{C}$, respectively.

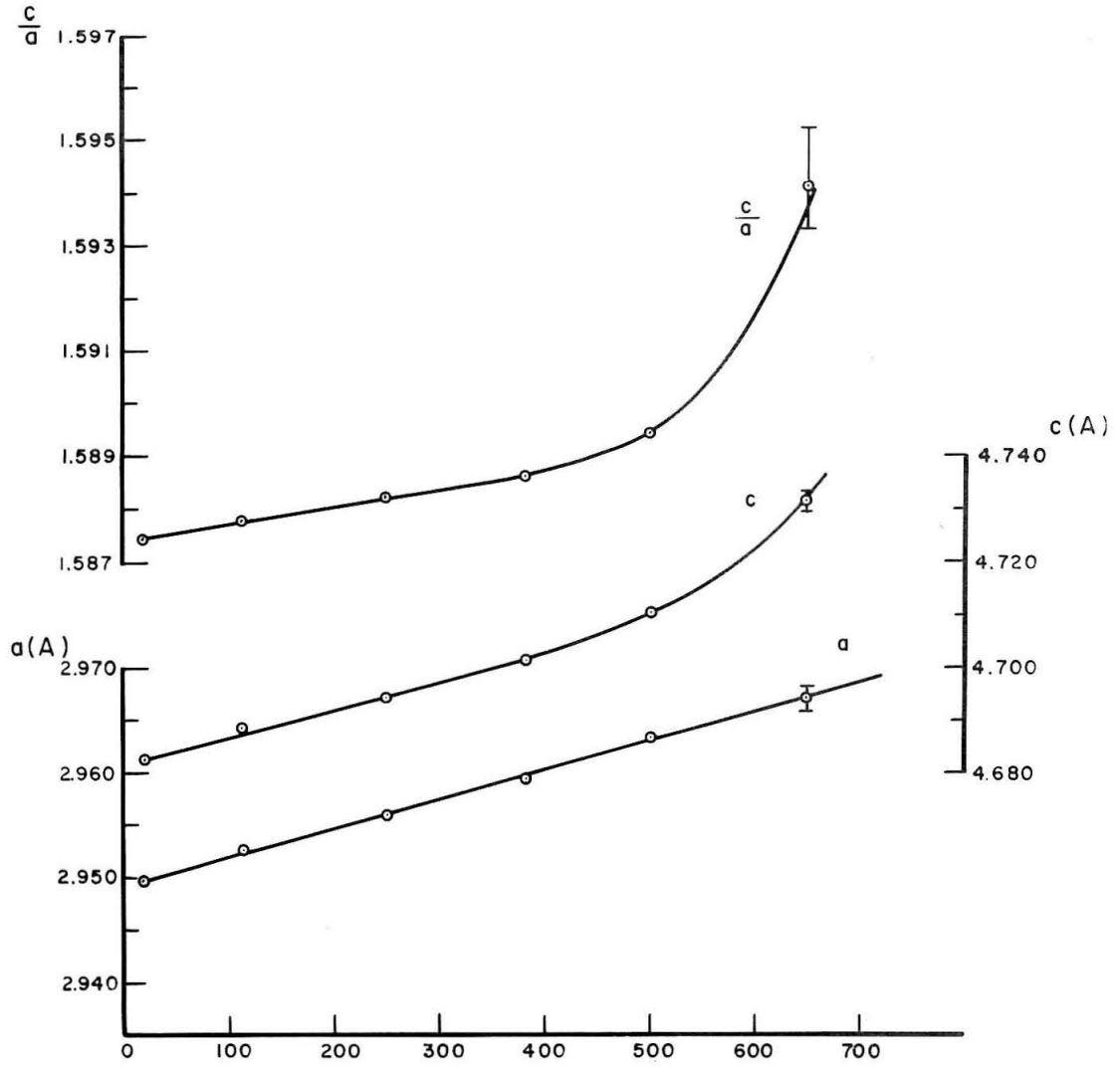


Figure 36. The thermal expansion of titanium.

PART II

**AN INVESTIGATION OF THE ALLOTROPIC
TRANSFORMATION OF TITANIUM**

6. DISCUSSION

The measurement of the temperature variation of the lattice parameters of titanium reported in the previous section, along with other experimental data, can be used to formulate a theory for the allotropic transformation of titanium. Of the sixty-three elements referred to as metals, approximately one third have allotropic transformations. In most cases the crystal structure changes, the transformation temperature and the mechanisms of transformation are well known; however, the fundamental reasons for the existence of an allotropic transformation in metals are not well known. There is little hope, at the present time, that a calculation based on first principles could yield any significant results. This is mainly because the difference in energy between different allotropic forms is the order of one per cent of the cohesive energy. The only possibility of coping with this problem is to examine the properties of the metal, formulate a model which can explain these properties and hopefully predict other properties. The model for titanium, which will be developed later, was proposed before construction of the high temperature x-ray diffractometer. According to this model, it was predicted that the c/a parameter should rapidly increase or decrease as the transformation temperature is approached. The experimental results show that the c/a actually increases.

The factor which determines the stability of one phase in preference to another is its free energy. At absolute zero there is no entropy diminution to the free energy so the crystallographic form with the lowest internal energy will be stable. For the purpose of discussion,

it is convenient to make the adiabatic approximation⁽⁷¹⁾ and consider the contributions to the free energy of the ion cores and free electrons separately.

The contribution of the ion cores to the free energy can be treated by the conventional quantum statistical treatment. In this treatment the displacement of the cores is assumed to be small so that a Taylor's expansion of the potential about the equilibrium position results in the harmonic approximation. The eigen-energies of the ion cores are then

$$E_n = (n + \frac{1}{2}) h\nu \quad (6.1)$$

The probability that a given oscillator, in thermal equilibrium, will be in the quantum state n is proportional to the Boltzmann factor $e^{-E_n/kT}$.

The partition function for such an oscillator is

$$f = \sum_n e^{-E_n/kT} \quad (6.2)$$

or

$$f = \frac{e^{-\frac{h\nu}{2kT}}}{1 - e^{-\frac{h\nu}{kT}}} \quad (6.3)$$

The average free energy can then be determined by the equation⁽⁷²⁾

$$\bar{F} = -kT \ln f \quad (6.4)$$

Using equation 6.3

$$\bar{F}(\nu) = \left[\frac{h\nu}{2} + kT \ln(1 - e^{-\frac{h\nu}{kT}}) \right] \quad (6.5)$$

The free energy for the ion cores is

$$F_c = \int F(\nu) \rho(\nu) d\nu \quad (6.6)$$

where $\rho(\nu)d\nu$ is the density of vibrational states between ν and $\nu + d\nu$. The integral of $\rho(\nu)d\nu$ over all possible states is subject to the restriction that it be equal to the total number of degrees of freedom for the system, i. e., for N ions.

$$\int_0^{\infty} \rho(\nu)d\nu = 3N \quad (6.7)$$

The value of $\rho(\nu)$ has been treated in a variety of ways ranging from the single frequency model of Einstein⁽⁷³⁾ to the crystal dynamics method of Born and von Kármán⁽⁷⁴⁾. For the purpose of simplicity, the following discussion will be limited to the continuum model of Debye⁽⁷⁵⁾. Under the assumption of this model

$$\rho(\nu)d\nu = \frac{9N}{\nu_m^3} \nu^2 d\nu \quad (6.8)$$

where ν_m is the upper frequency limit.

The Debye temperature is defined as

$$\theta = \frac{h\nu_m}{k} \quad (6.9)$$

With the use of equations 6.5 and 6.8, the free energy is

$$F_c = \frac{9N}{\nu_m^3} \left[\int_0^{\nu_m} \frac{h\nu^3}{2} d\nu + kT \int_0^{\nu_m} \nu^2 \ln \left(1 - e^{-\frac{h\nu}{kT}} \right) d\nu \right] \quad (6.10)$$

Using equation 6.9 and letting $x = h\nu/kT$, equation 6.10 can be written

$$F_c = 9Nk \left[\frac{\theta}{8} + \frac{T^4}{\theta^3} \int_0^{\theta/T} x^2 \ln(1-e^{-x}) dx \right] \quad (6.11)$$

Integrating by parts, the above equation reduces to

$$F_c = 3Nk \left[\frac{3\theta}{8} + T \ln(1-e^{-\theta/T}) - \frac{T^4}{\theta^3} \int_0^{\theta/T} \frac{x^3}{e^x - 1} dx \right] \quad (6.12)$$

The integral in the above expression is a common one sometimes referred to as the Debye integral and has been tabulated⁽⁷⁶⁾ for various values of θ/T . For the case where $T \ll \theta$ equation 6.12 reduces to

$$F_c \approx 3Nk\theta \left[\frac{3}{8} - \frac{T}{\theta} e^{-\theta/T} - \frac{\pi^4}{15} \left(\frac{T}{\theta} \right)^4 \right] \quad (6.13)$$

For the case when $T \gg \theta$, equation 6.12 reduces to

$$F_c \approx 3Nk\theta \left[\frac{1}{2} - \frac{1}{3} \frac{T}{\theta} + \frac{T}{\theta} \ln \left(\frac{\theta}{T} \right) \right] \quad (6.14)$$

The variation of the free energy of the ions with temperature, with the Debye assumption, is illustrated in Figure 37. The binding energy at 0°K must be added to the above expression for completeness. It is evident from the above expressions that if the free energy is predominantly governed by the ions, the Debye temperature of the high temperature phase must be less than the Debye temperature of the low temperature phase.

The cohesive energy of metals is composed of the electrostatic attraction between the free electrons and the ion cores, the repulsion between the ion cores, electron-electron interactions, and the mean kinetic energy of the free electrons. The properties of electrons outside

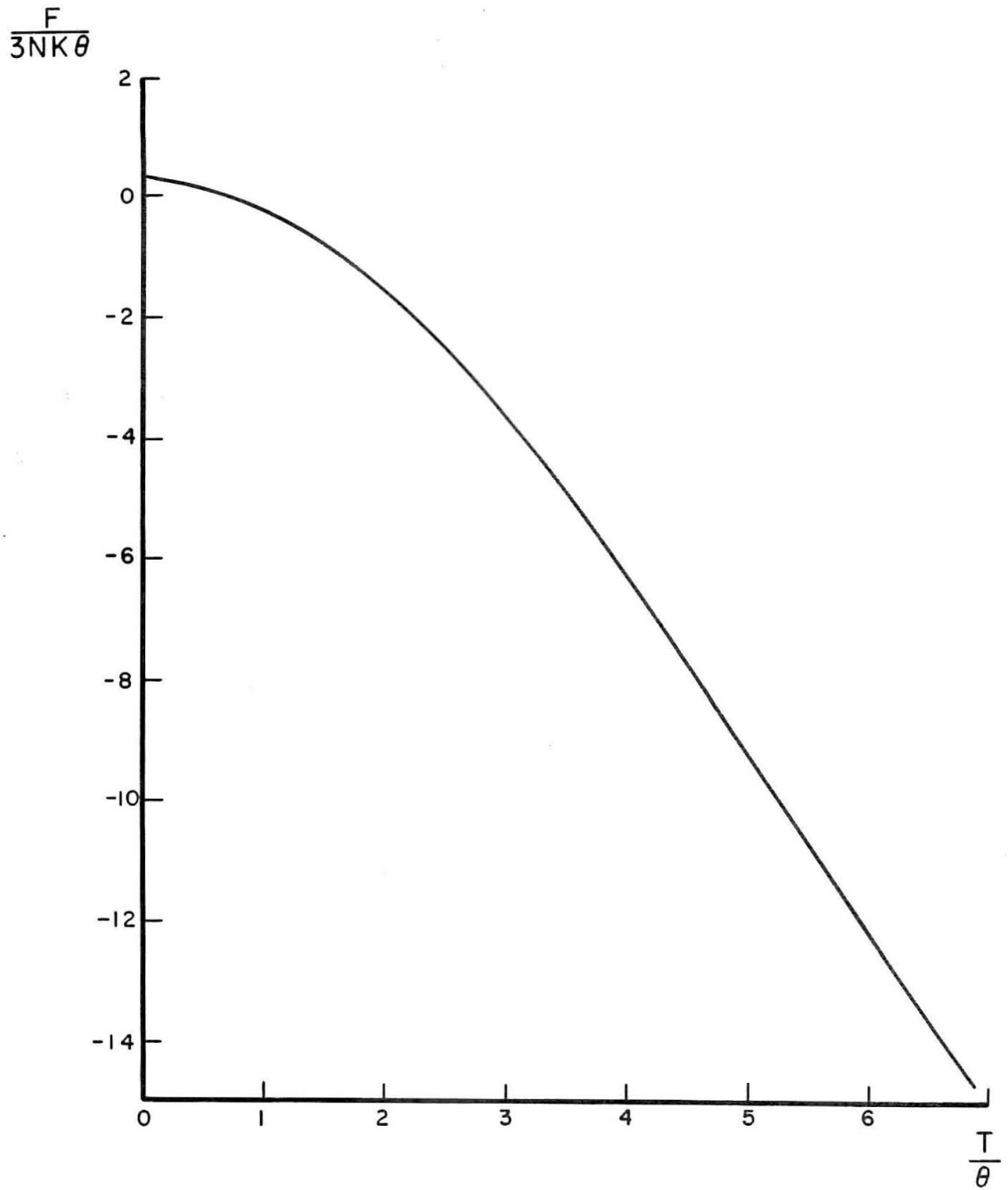


Figure 37. The temperature variation of the free energy of a Debye solid.

of the closed ion cores will be interpreted on the basis of the band theory of solids. The development of the band theory based on one electron wave functions has been discussed in numerous texts and only some of the assumptions and conclusions will be enumerated. First the interactions between electrons is neglected except that they must obey the Pauli exclusion principle. Thermodynamic equilibrium requires that the electron obey Fermi-Dirac statistics, i. e., the probability that a quantum state with energy E is occupied is

$$f_o(E) = \frac{1}{e^{(E-E_f)/kT} + 1} \quad (6.15)$$

where E_f is determined by the total number of electrons present. The wave functions of electrons in a periodic lattice are the Bloch type

$$\psi = \chi_k(\vec{r}) e^{i\vec{k} \cdot \vec{r}} \quad (6.16)$$

where $\chi_k(\vec{r})$ is a function depending in general on \vec{k} and has the same periodicity as the lattice. In the simplest case χ_k is a constant and the wave function is that of a free electron. The eigen-energies are

$$E_k = \frac{\hbar^2 |\vec{k}|^2}{2m} \quad (6.17)$$

If an electron is tightly bound to an atom, χ_k is zero everywhere in the unit cell except in the immediate vicinity of the particular atom. For this case, the dependence of the eigen-energies on k is very small. Near the bottom of the band this dependence can be represented by a formula like equation 6.17, but m is replaced by m^* , the effective mass.

Near the top of the band the energy is given by

$$E_{\vec{k}} = A - \frac{\hbar^2 |\vec{k}|^2}{2m^*} \quad (6.18)$$

For the tight binding approximation m^* is very large. Between these two extreme cases, is that of the perturbation of nearly free electrons by a periodic potential. For this case, E is not a continuous function of \vec{k} but there are values of \vec{k} for which there are gaps in energy. The regions of continuity are between concentric polyhedra in \vec{k} -space commonly referred to as Brillouin zones. The zone boundaries are entirely determined by the point and space group symmetries of the crystal lattice. In general, the zone boundaries are given by

$$\vec{g}_b \cdot \vec{k} + \pi |\vec{g}_b|^2 = 0 \quad (6.19)$$

where

$$\vec{g}_b = g_1 \vec{b}_1 + g_2 \vec{b}_2 + g_3 \vec{b}_3 \quad (6.20)$$

and \vec{b}_1 , \vec{b}_2 and \vec{b}_3 are the reciprocal lattice vectors. If any of the space or point group symmetries of the crystal lattice make the structure factor S_g equal to zero, then the corresponding energy discontinuity disappears at the zone boundary given by equation 6.10. The structure factor is

$$S_g = \sum_t e^{2\pi i \vec{g}_b \cdot \vec{s}_t} \quad (6.21)$$

where \vec{s}_t is the location of the t^{th} atom in the unit cell. Some of the general rules which govern Brillouin zones are as follows. All zones have equal volume in \vec{k} -space. This is due to the fact that a translation $\vec{k} \rightarrow \vec{k} + \vec{g}_b$ maps all zones into the first zone and a translation of this

type leaves the Bloch type wave function unaltered. It is therefore possible to neglect all zones except the first and regard the energy as a multivalued function of k . Each zone contains $2N$ states where N is the number of cells in the crystal lattice. If a reduced zone scheme is used it must be emphasized that there are not necessarily $2N$ states between energy discontinuities because the structure factor can eliminate some of the energy discontinuities across Brillouin planes. Thus there might be considerably more or less than $2N$ states between energy discontinuities depending on the space group symmetry of the crystal lattice. For titanium, which is close-packed hexagonal, $S_g = 0$ for $g_1 + 2g_2 = 3n$ and g_3 odd, where n is an integer. Neighboring zones may have overlapping energy levels. Within a zone, the surface which is formed by all the filled states up to $E(\vec{k})_{\max}$ is called the Fermi surface. In most metals, excluding the monovalent ones, the Fermi surface is not a single surface but consists of portions of surfaces belonging to different Brillouin zones. The only restriction on these surfaces is that the Fermi energy be the same. The thermal, electrical and magnetic properties of the free electrons in a metal depend only on those states which are very close to the Fermi energy. In a multi-surface metal, although the Fermi energy is the same, the contributions to the above mentioned properties from the various surfaces can be quite different.

The contribution of the electrons to the free energy for the case of one unfilled band can be evaluated with the following formula

$$F_e = U_e - T \int_0^T \frac{1}{T} \frac{dU_e}{dT} dT \quad (6.22)$$

where U_e is the internal energy per unit volume. U_e can be expressed

in terms of the density of states for one direction of spin⁽⁷⁷⁾, $N(E)$.

$$U_e = 2 \int_0^{E_f^0} EN(E)dE + \frac{1}{3} (\pi k T)^2 N(E_f^0) \quad (6.23)$$

where E_f^0 is the Fermi energy at absolute zero. Substituting the above expression into equation 6.22, the free energy per unit volume is

$$F_e = 2U^0 - \frac{1}{3} (\pi k)^2 N(E_f^0) T^2 \quad (6.24)$$

where

$$U^0 = \int_0^{E_f^0} EN(E)dE \quad (6.25)$$

The second term in equation 6.24, which represents the temperature variation of the free energy due to the electrons, is so small (the order of 10^{-8} ev/atom/ $^{\circ}K^2$) that it can have no effect on determining the stability of one phase in preference to another.

There is a possibility that an electron configuration which changes with temperature can cause the instability of a phase. This can occur by changing the overlaps between different bands or thermally exciting electrons to an empty band. Since it is believed that the model for titanium fits the case for thermal excitation, as will be justified later, only this latter case will be discussed.

The band structure of titanium is presumed to consist of three overlapping Fermi surfaces. Each of the three bands associated with these surfaces are assumed to be almost completely filled. One of these bands is very narrow with a high density of states at E_f^0 . It is this band that mainly contributes to the large cohesive energy (112 K cal/mole) of

titanium. The second band is not as narrow and also does not contribute as much to the density of states at E_f^0 as the first band. These bands are usually referred to as 3d-bands. The other band is a normal band referred to as a 4s-band. A schematic representation of this band structure is shown in Figure 38. A band structure like this would account for (1) the very high cohesive energy, which is the highest in the first transition series⁽⁷⁸⁾ (2) the high resistivity, which is thirty-three times greater than that of copper and higher than any of the elements in the first transition series, (3) the paramagnetic susceptibility, and (4) high electronic specific heat⁽⁷⁹⁾. In addition to these bands, another band is hypothesized which has an energy gap associated with a direction in \vec{k} -space.

The experimental evidence for the existence of an energy gap is deduced from the temperature variations of the c/a lattice parameter, the magnetic susceptibility and the electrical resistance. As shown in the preceding section, the c/a parameter for titanium rapidly increases as the transformation temperature is approached. This phenomenon has a very simple explanation based on an interpretation by Jones⁽⁸⁰⁾ and extended by Goodenough⁽⁸¹⁾. Jones and Goodenough have shown that in a non-cubically symmetrical lattice when the Fermi surface overlaps an energy zone in a particular direction in \vec{k} -space, the electrons in the overlapped region exert a force which expands the real lattice in the same direction as the overlap, resulting in an anisotropic strain. Evidently, for titanium, electrons are being thermally excited across the (002) Brillouin plane causing a rapid increase in the c/a parameter as the population of the upper zone becomes appreciable.

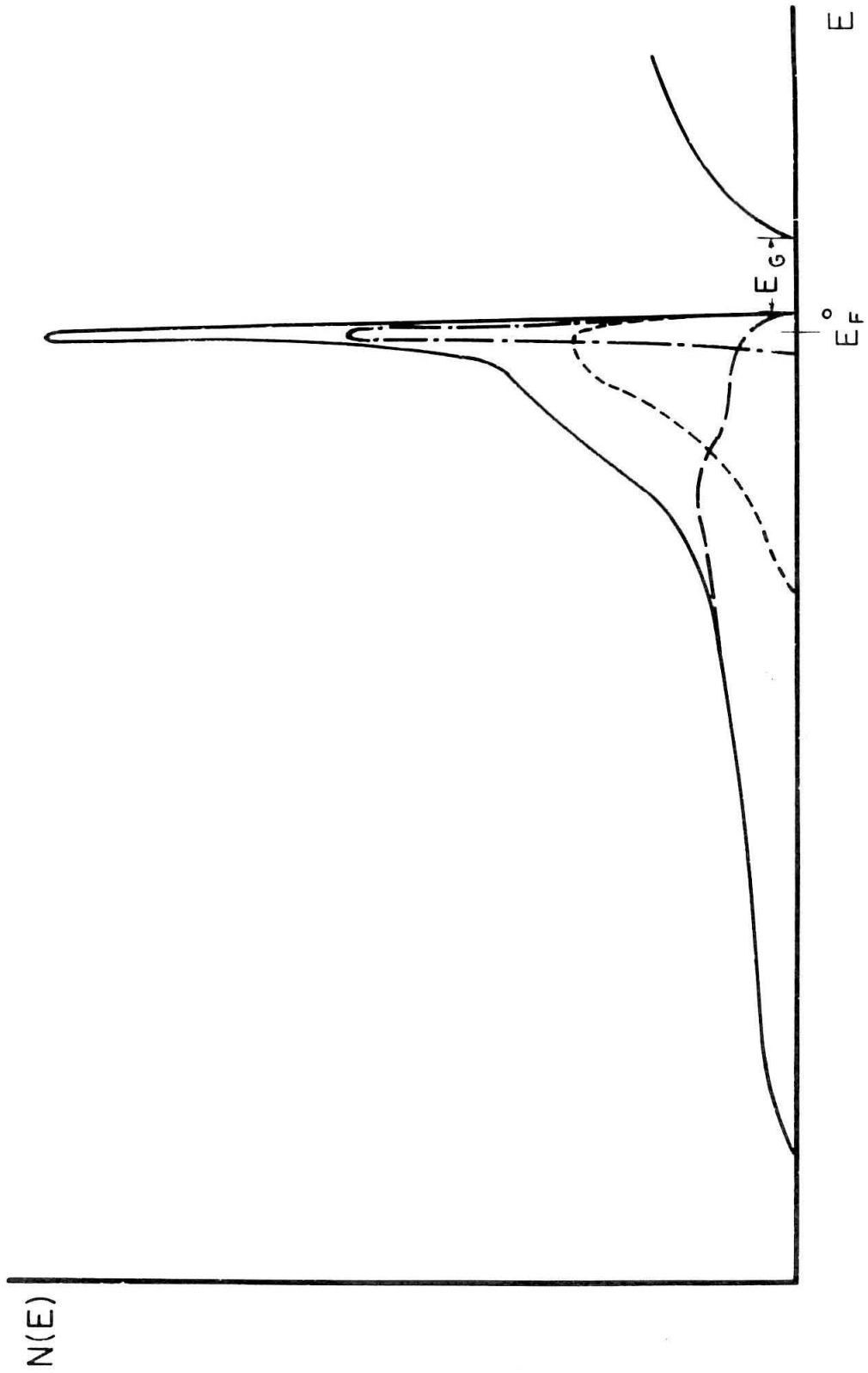


Figure 38. Schematic of proposed band structure for titanium.

The temperature variation of the magnetic susceptibility of titanium as determined by Squire and Kaufman⁽⁸³⁾ is shown in Figure 39. This behavior is similar to that of antiferromagnetic materials. However, no evidence has been found to show that titanium is antiferromagnetic. An alternate explanation, based on a single or multiple overlapped band model, would be that the density of states at the Fermi energy rapidly increased with increasing temperature. This is extremely unlikely and must be ruled out when the order of magnitude the paramagnetic susceptibility increases over its low temperature value is considered. However, if an energy gap is postulated, then the susceptibility would be the sum of the susceptibilities from the two bands. The contribution from the lower band would essentially remain constant, or slightly decrease with increasing temperature. The contribution of the upper band to the susceptibility would increase with temperature as the population of this band increased. Since the electrons in the upper band are probably not degenerate, their contribution to the susceptibility would be quite large. The uncertainty of the correlation and exchange of the electrons in the upper band make any calculation from the susceptibility data difficult.

The temperature variation of the electrical resistance as determined by Wyatt⁽⁸³⁾ is shown in Figure 40. The temperature variation of the electrical resistance with temperature is expected to be linear^(84, 85) for $T > 0$ as long as there are not any changes in the band structure. If there is any departure from linearity, it should be in the opposite sense than shown in Figure 40, due to the creation of vacancies

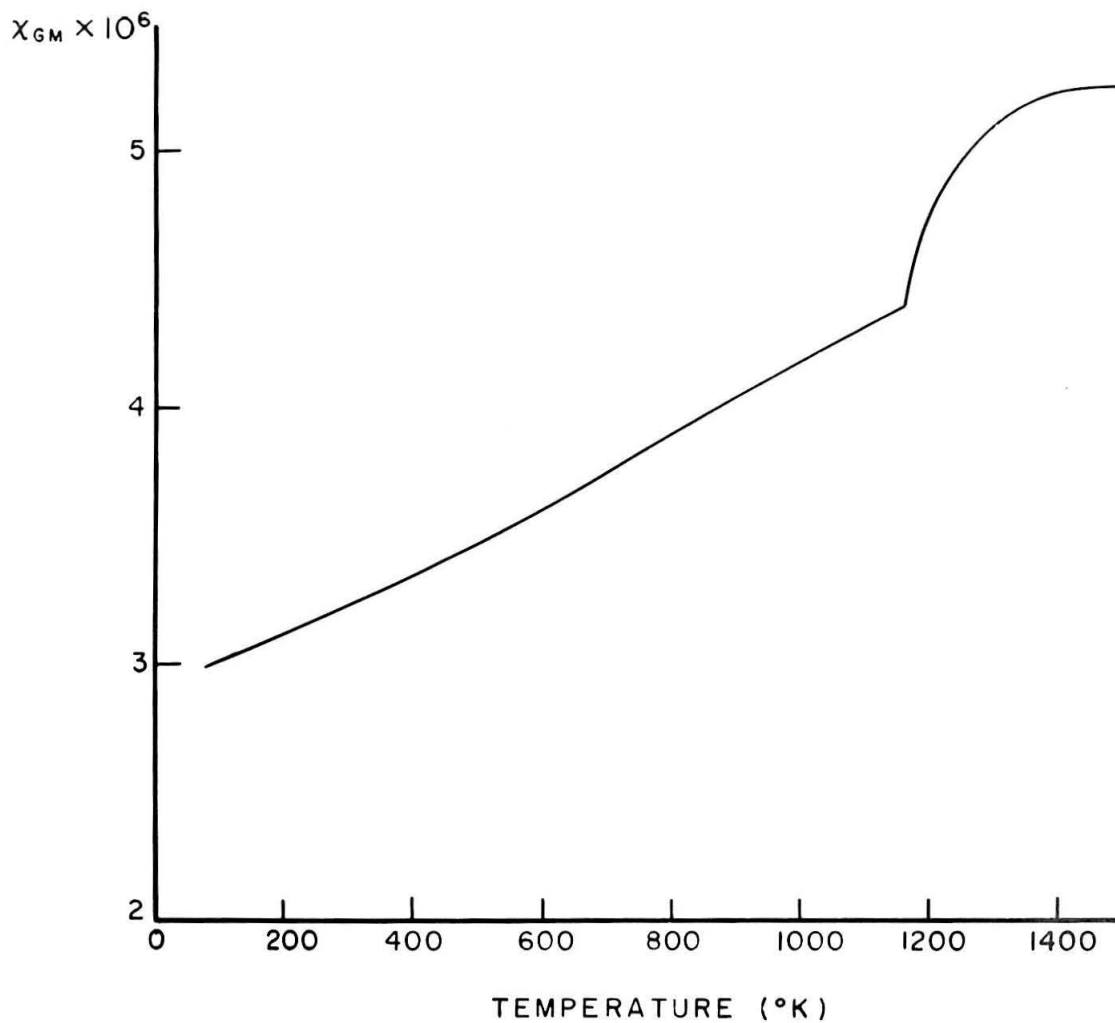


Figure 39. The temperature variation of the magnetic susceptibility of titanium (after Squire and Kaufman).

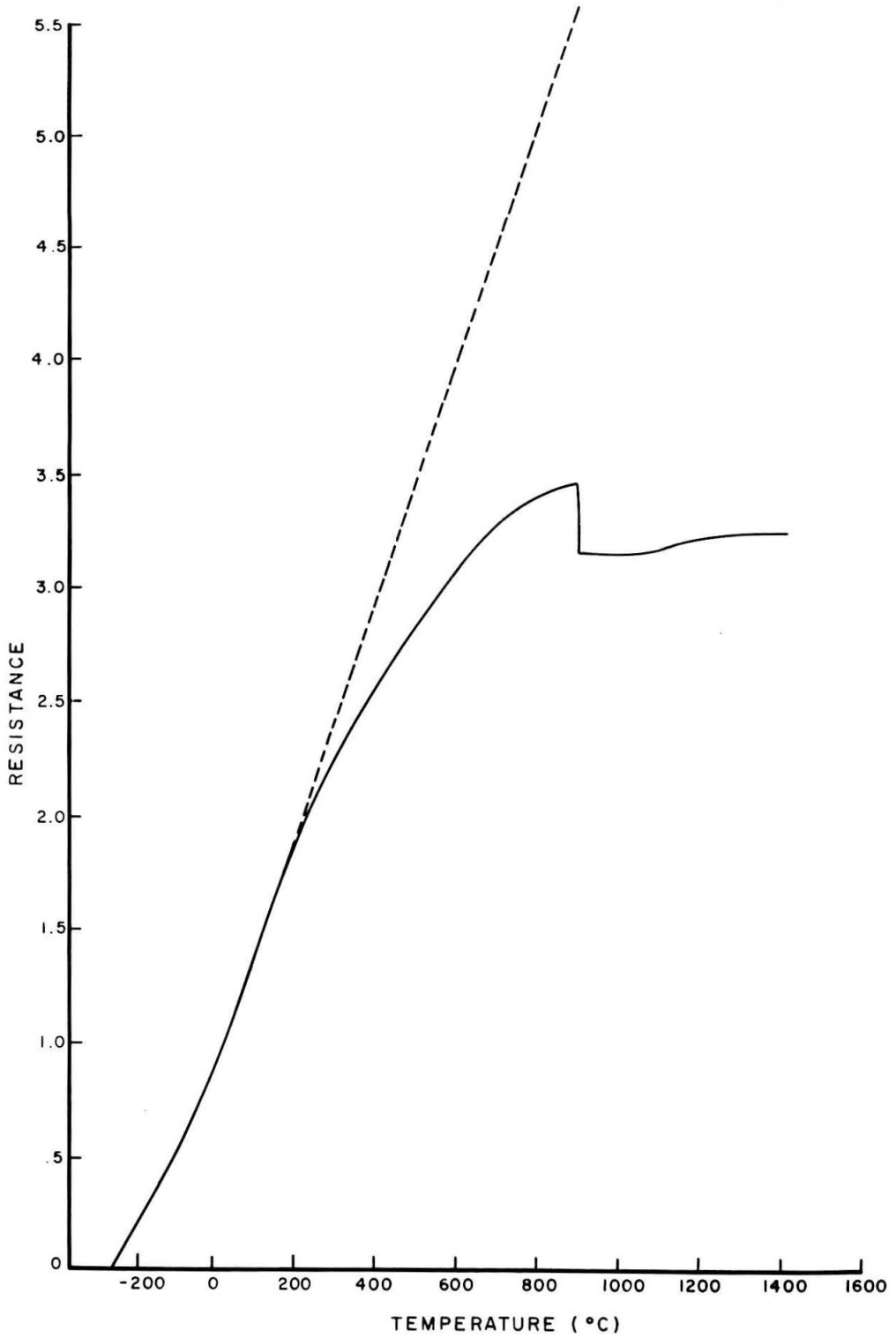


Figure 40. The temperature variation of the electrical resistance of titanium (after Wyatt).

as the temperature is increased. This apparent increase in conductivity is attributed to the increase in number of conducting states as electrons are thermally excited into the upper band.

The calculation of the free energy for this model is complicated. An estimate can be made with the following assumptions; (1) the free energy of the lower bands can be represented by equation of the type 6.24. (2) The Fermi energy is below the upper band and above the lower bands in the temperature region of interest so the electrons excited into the upper band can be approximated by Maxwell-Boltzmann statistics. (3) The number of electrons per unit volume excited to the upper band, referred to as n_j , is much greater than the number of vacant states in the lower bands at absolute zero. (4) The change in cohesive energy by removing an electron from a surface in the lower bands, where i refers to the surface, is denoted by V_j^i and is assumed to be independent of the number of electrons excited to the upper band. With these assumptions, the internal energy per unit volume is

$$U_e = \sum_i \left[2U_i^0 + \frac{1}{3} (\pi kT)^2 N_i(E_f^0) \right] + n_j \left[E_g + \frac{3}{2} kT \right] + \sum_i n_j^i V_j^i \quad (6.26)$$

where E_g is the gap energy and n_j^i is the number of electrons excited to the upper band from the i^{th} surface.

The free energy of this band model for titanium can be expressed in terms of the thermodynamic potential, Ω , of the system.

$$F_e = U_e + T \left(\frac{d\Omega}{dT} \right) \quad (6.27)$$

The thermodynamic potential of a Fermi gas is⁽⁸⁶⁾

$$\Omega = -kT \sum_n \ln \left[1 + e^{(E_f - E_n)/kT} \right] \quad (6.28)$$

or

$$\Omega = -kT \left\{ \sum_i 2 \int N_i(E) \ln \left[1 + e^{(E_f - E)/kT} \right] dE + 2 \int N_j(E) \ln \left[1 + e^{(E_f - E)/kT} \right] dE \right\} \quad (6.29)$$

where $N_i(E)$ represents the density of states in the lower bands and $N_j(E)$ the density of states in the upper band for one direction of spin.

Using the above expression for Ω and equation 6.28, equation 6.27 can be simplified to

$$F_e = (n_j + \sum_i n_i) E_f - \Omega + \sum_i n_j^i V_j^i \quad (6.30)$$

If $E_f > E$ for the lower bands and $E_f < E$ for the upper band, equation 6.29 can be simplified to

$$\Omega \approx -kT \left[2 \sum_i \int N_i(E) \frac{(E_f - E)}{kT} dE + 2 \int N_j(E) e^{(E_f - E)/kT} dE \right] \quad (6.31)$$

or

$$\Omega \approx -E_f \sum_i n_i + 2 \sum_i U_i - n_j kT \quad (6.32)$$

Substituting the above expression into equation 6.30, the free energy per unit volume is

$$F_e \approx 2 \sum_i U_i + n_j(E_f - kT) + \sum_i n_j^i V_j^i \quad (6.33)$$

For titanium it is assumed that V_j^i for an electron removed from the d-bands to the upper band is positive, while for the s-band V_j^i is nearly zero.

The number of electrons excited to the upper band and the Fermi energy can be estimated by equating the number of electrons in the lower bands at $T = 0$ to the number of electrons distributed between the upper and lower bands at $T \neq 0$. That is

$$2 \sum_i \int N_i(E) dE = 2 \sum_i \int \frac{N_i(E) dE}{e^{(E-E_f)/kT} + 1} + 2 \int \frac{N_j(E) dE}{e^{(E-E_f)/kT} + 1} \quad (6.34)$$

Since the number excited to the upper band is small, the denominator in the above integrals will be nearly unity in the lower bands and very large in the upper band. If E is taken to be zero at the top of the lower bands, the above equation reduces to

$$\sum_i \left[- \int_{-E_f^0}^0 N_i(E) dE + e^{-E_f/kT} \int_{-\infty}^0 N_i(E) e^{E/kT} dE \right] = e^{E_f/kT} \int_{E_g}^{\infty} N_j(E) e^{-E/kT} dE \quad (6.35)$$

where $-E_f^0$ is the Fermi energy at $T = 0$. The integral on the left is the number of unfilled states in the lower bands at absolute zero and is assumed to be small compared to the other integrals in the temperature

region of interest. Neglecting terms in which this integral appears in powers higher than the first, the above can be solved for E_f in terms of the density of states.

$$E_f \approx \frac{1}{2} kT \ln \left[\frac{\sum_i \int_{-\infty}^0 N_i(E) e^{E/kT} dE}{\int_{E_g}^{\infty} N_j(E) e^{-E/kT} dE} \right]$$

$$-\frac{1}{2} kT \frac{\sum_i \int_{-E_f}^0 N_i(E) dE}{\left[\sum_i \int_{-\infty}^0 N_i(E) e^{E/kT} dE \right]^{1/2} \left[\int_{E_g}^{\infty} N_j(E) e^{-E/kT} dE \right]^{1/2}} \quad (6.36)$$

The number of electrons n_j , excited into the upper band is

$$n_j = 2 \int_{E_g}^{\infty} \frac{N_j(E) dE}{e^{(E-E_f)/kT} + 1} \quad (6.37)$$

or

$$n_j \approx 2 e^{E_f/kT} \int_{E_g}^{\infty} N_j(E) e^{-E/kT} dE \quad (6.38)$$

Using equation 6.36, the above expression becomes

$$n_j = 2 \left[\sum_i \int_{-\infty}^0 N_i(E) e^{E/kT} dE \right]^{1/2} \left[\int_{E_g}^{\infty} N_j(E) e^{-E/kT} dE \right]^{1/2} - \sum_i \int_{-E_f^0}^0 N_i(E) dE \quad (6.39)$$

The number of electrons excited from the i^{th} surface to the upper band,

$$n_j^i \text{ is } n_j^i = 2 \int_{-\infty}^{-E_f^0} N_i(E) dE - 2 \int_{-\infty}^0 \frac{N_i(E) dE}{e^{(E-E_f)/kT} + 1} \quad (6.40)$$

or

$$n_j^i = 2 e^{-E_f/kT} \int_{-\infty}^0 N_i(E) e^{E/kT} dE - 2 \int_{-E_f^0}^0 N_i(E) dE \quad (6.41)$$

Using equation 6.36, the above expression becomes

$$n_j^i = 2 \left[\int_{-\infty}^0 N_i(E) e^{E/kT} dE \frac{\int_{E_g}^{\infty} N_j(E) e^{-E/kT} dE}{\sum_i \int_{-\infty}^0 N_i(E) e^{E/kT} dE} \right]^{1/2} \times \left[1 + \frac{\int_{-E_f^0}^0 N_i(E) dE}{\left(\int_{E_g}^{\infty} N_j(E) e^{-E/kT} \right)^{1/2} \left(\sum_i \int_{-\infty}^0 N_i(E) e^{E/kT} dE \right)^{1/2}} - 2 \int_{-E_f^0}^0 N_i(E) dE \right]^{1/2} \quad (6.42)$$

Knowledge of the density of states in each of the bands is required for further calculations.

An estimate of E_f , n_j and n_j^i can be made by judiciously choosing values for the density of states to evaluate the preceding integrals. The density of states in the upper band, $N_j(E)$ can be assumed to be a function solely of $E - E_g$. If

$$\xi = \frac{E - E_g}{kT} \quad (6.43)$$

the integral

$$\int_{E_g}^{\infty} N_j(E) e^{-E/kT} dE = kT e^{-E_g/kT} \int_0^{\infty} N_j(\xi, kT) e^{-\xi} d\xi \quad (6.44)$$

or

$$\int_{E_g}^{\infty} N_j(E) e^{-E/kT} dE = e^{-E_g/kT} G_j(kT) \quad (6.45)$$

It is difficult to estimate the $N_i(E)$ but noting that the main contribution to the integrals involving $N_i(E)$ occur at small values of E and $N_i(E) \rightarrow 0$ as $E \rightarrow 0$, only a small error will be made by assuming

$$N_i(E) = w_i N(E_f^0) \quad E < -E_f^0 \quad (6.46)$$

and

$$N_i(E) = -\frac{w_i N(E_f^0)}{E_f^0} E \quad -E_f^0 < E < 0 \quad (6.47)$$

where w_i is the weighting value of each Fermi surface. Substituting the above expressions into equation 6.38, 6.41 and 6.36 and simplifying, the values for n_j , n_j^i and E_f reduce to

$$n_j = 2 G_j(kT) e^{(E_f - E_g)/kT} \quad (6.48)$$

$$n_j^i = 2w_i N(E_f^0) kT e^{-E_f/kT} \left[1 - \frac{E_f^0}{2kT} e^{E_f/kT} \right] \quad (6.49)$$

and

$$E_f = \frac{E_g}{2} + \frac{1}{2} kT \ln \left[\frac{N(E_f^0) kT}{G_j(kT)} \right] - \frac{E_f^0}{4} \left[\frac{N(E_f^0) kT e^{E_g/kT}}{G_j(kT)} \right]^{1/2} \quad (6.50)$$

The free energy per unit volume is obtained by substituting the above expressions into equation 6.33.

An order of magnitude calculation can be made by either determining or estimating some of the preceding parameters. The value of E_f , which is about half the gap energy (there is a temperature variation of E_f which is difficult to determine without knowing something about the density of states) can be determined from the previously mentioned apparent increase in conductivity. If the apparent increase in conductivity is denoted by $\Delta \sigma$, then

$$\Delta \sigma \propto n_j \quad (6.51)$$

or

$$\Delta \sigma \propto \sum_i n_j^i \quad (6.52)$$

Using equation 6.49

$$\ln \Delta \sigma = \frac{-E_f}{kT} + \ln A(T) \quad (6.53)$$

The second term in the above equation is assumed to vary slowly with

temperature so that a plot of $\ln \Delta \sigma$ vs. $\frac{1}{T}$ should be a straight line. Table 6.1 shows a resumé of the results using Wyatt's⁽⁸³⁾ data. R' and σ' are the resistance and conductivity if a linear law is assumed with a linear temperature coefficient of resistance of 4.95×10^{-3} ohm/ $^{\circ}$ C.

Table 6.1

Temperature $^{\circ}$ K	R	R'	σ	σ'	$\Delta \sigma$
419.9	1.600	1.600	0.6250	0.6250	0
543.2	2.106	2.211	0.4748	0.4523	.023
768.2	2.828	3.325	0.3536	0.3008	.053
1001.5	3.328	4.480	0.3005	0.2232	.077
1151.0	3.453	5.221	0.2896	0.1915	.098

A plot of $\ln \Delta \sigma$ vs. $\frac{1}{T}$ is shown in Figure 41. The reduced data from Greiner and Ellis⁽⁶⁹⁾ is also shown in the same figure. The titanium sample of Greiner and Ellis had more impurities than Wyatt's. From Wyatt's data $E_f = 0.13$ ev which would be about half the gap energy. The linearity of these curves is why the model for titanium, which explains the electron configuration that changes with temperature, was chosen to be that of thermal excitation.

The density of states, $N(E_f^0)$ can be determined by specific heat measurements at low temperatures, i. e.,

$$C = \gamma T \tag{6.54}$$

where

$$\gamma = 2/3 (\pi k)^2 N(E_f^0) \tag{6.55}$$

$N(E_f^0)$ has the value of 0.755 levels/atom/ev for titanium as determined

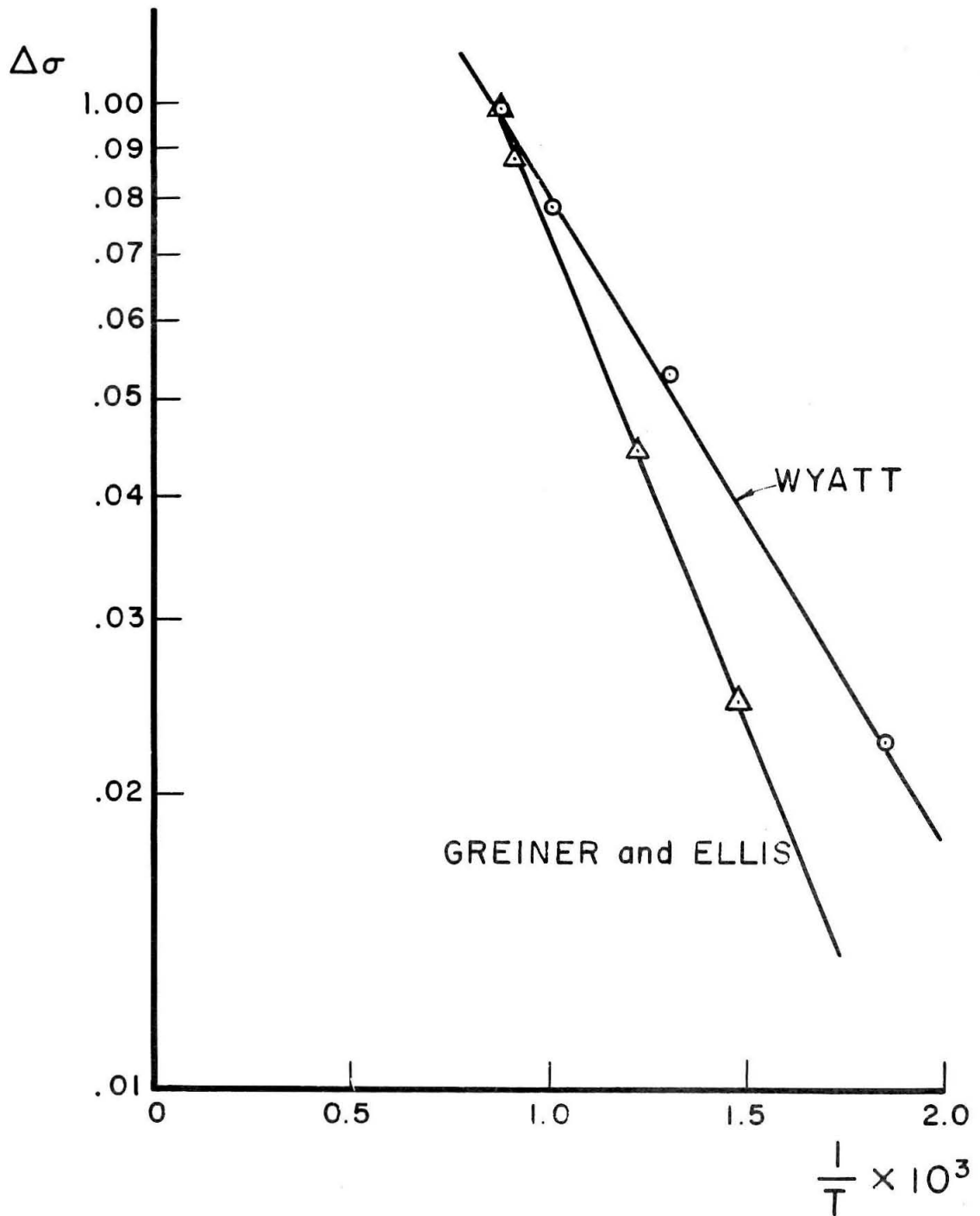


Figure 41.

by Wolcott⁽⁷⁴⁾.

An estimate of E_f^0 can be made by noting the temperature at which the resistance vs. temperature curve departs from linearity (about 420°K). From equation 6.49, the upper band occupation starts when

$$e^{-E_f/kT} = \frac{E_f^0}{2kT}$$

Solving the above equation, with $T = 420^\circ\text{K}$ and $E_f = 0.13 \text{ ev}$, the value for E_f^0 is $2 \times 10^{-3} \text{ ev}$.

The values of the other parameters will be assumed to be

$$w_1 = 0.6 \qquad V_j^1 = \frac{50}{N_0} \text{ K cal/electron}$$

$$w_2 = 0.3 \qquad V_j^2 = \frac{20}{N_0} \text{ K cal/electron}$$

$$w_3 = 0.1 \qquad V_j^3 = 0$$

where N_0 is Avogadro's number. Table 6.2 summarizes the free energy variation of the electrons with temperature using the above mentioned values. If $\theta = 360^\circ$ is taken for titanium⁽⁷⁹⁾, the net contribution of both the ions and electrons is illustrated in Figure 42.

In the preceding analysis, the Fermi energy has been assumed to be between the bands. However, it is evident from equations 6.36 and 6.50 that the Fermi energy is a function of temperature and, depending upon the nature of $G_j(kT)$, can move into the upper band. For this case, the distribution of electrons between the upper and lower

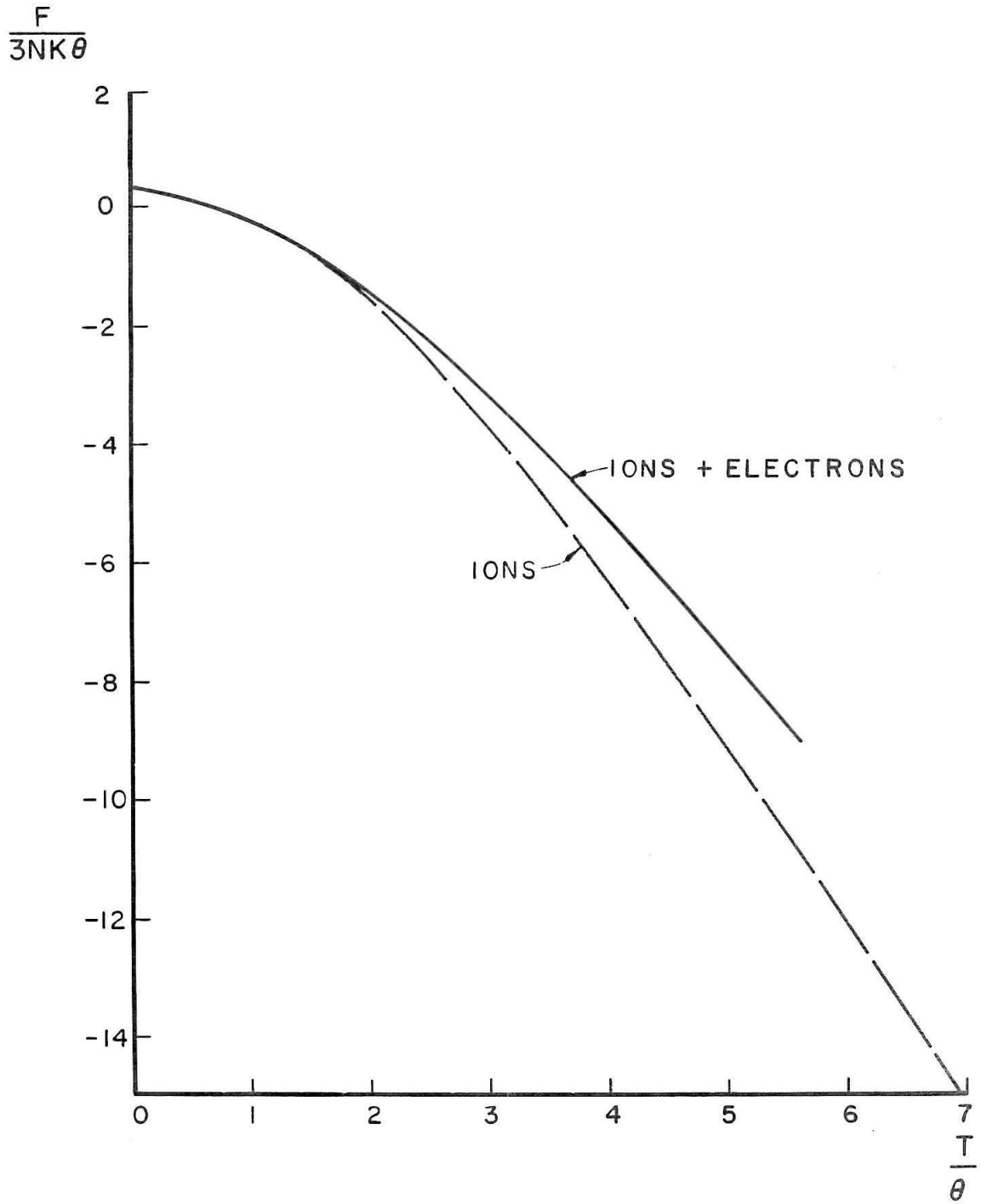


Figure 42. The temperature variation of the free energy.

Table 6.2

Temp. °K	$n_j \times 10^{-22}$	$n_j^1 \times 10^{-22}$	$n_j^2 \times 10^{-22}$	$n_j^3 \times 10^{-22}$	F_e (cal/cm ³)
400	0	0	0	0	0
600	0.027	0.016	0.008	0.003	17
800	0.081	0.049	0.024	0.008	50
1000	0.154	0.091	0.046	0.015	94
1200	0.242	0.145	0.073	0.024	148
1600	0.448	0.269	0.134	0.045	266
2000	0.682	0.409	0.205	0.068	397

bands, equation 6.35, must be corrected. It is evident that the left side of equation 6.35 is unchanged; however the right side, which represents the number of electrons in the upper band, is

$$n_j = \int_{E_g}^{\infty} \frac{N_j(E)}{e^{(E-E_f)/kT} + 1} \quad (6.56)$$

or,

$$n_j = kT \int_0^{\infty} \frac{N_j(\xi, kT)}{\frac{e^{\xi}}{z} + 1} \quad (6.57)$$

where,

$$\xi = \frac{E-E_g}{kT} \quad \text{and} \quad z = e^{(E_f-E_g)/kT} \quad (6.58)$$

If $E_f < E_g$, then z is small and the analysis is as before. However, if $E_f > E_g$ then z is large and there is a much larger contribution to the integral for small values of ξ . Therefore, if the Fermi energy exceeds the gap energy, the positive contribution to the free energy would be even greater than that shown in Figure 42.

If the upper band is considered to be normal, i. e.,

$$E_j = E_g + \frac{\hbar^2 |\vec{k}|^2}{2m_j^*} \quad (6.59)$$

where m_j^* is the effective mass, then

$$N_j(E) = \frac{2\pi(2m_j^*)^{3/2}}{h^3} (E-E_g)^{1/2} \quad (6.60)$$

Using the above relation, assuming that the m_j^* is one electron mass and the previously mentioned values for the other parameters, equation 6.35 can be solved for the temperature when $E_f = E_g$. This temperature is 880 °K which is 275 °C below the transformation temperatures of titanium.

Although the results are very approximate, it is clear from the above that the contribution of the electrons to the free energy as the temperature increases is positive. It is believed that this positive variation of the free energy added to the negative variation of the lattice ions causes the instability of the lattice and hence an allotropic transformation. The high temperature modification should have a band structure that drastically reduces the positive variation to the free energy due to the electrons. This is accomplished by reducing n_j , which means increasing E_g .

7. CONCLUSIONS

The design and construction of a vacuum high temperature x-ray diffractometer has made possible the investigation of the thermal expansion of titanium. Between 0° and 400°C , the mean coefficients of thermal expansion perpendicular and parallel to the c -axis are $9.41 \times 10^{-6}/^{\circ}\text{C}$ and $11.18 \times 10^{-6}/^{\circ}\text{C}$, respectively. For a random polycrystalline sample, the mean linear expansion coefficient is $10.0 \times 10^{-6}/^{\circ}\text{C}$. Above 400°C the c/a parameter rapidly increases as the transformation temperature is approached, which supports a preconceived idea about the band structure of titanium. This band model has assumed that the electrons at the top of the band at 0°K are on overlapping Fermi surfaces (at least three) and there is a small number of unfilled states available to the electrons (approximately $5 \times 10^{19}/\text{cm}^3$) below an energy gap associated with the c -direction in \vec{k} -space. Calculations using this model show that the electrons can give an appreciable positive contribution to the free energy as the transformation temperature is approached which can result in an instability in the low temperature crystal structure.

Although the analysis is confined to titanium, the ideas formulated about allotropic transformations can probably be extended to other metals such as zirconium, hafnium, uranium and iron.

REFERENCES

1. A. Westgren, J. Iron and Steel Inst. (1921), vol. 103, p. 306.
2. A. Westgren and A. E. Lindh, Z. Phys. Chem. (1921), vol. 98, pp. 181-210.
3. K. Becker, Z. Phys. (1927), vol. 40, pp. 37-41.
4. W. Cohn, Z. Phys. (1928), vol. 50, pp. 123-136.
5. O. Ruff and F. Ebert, Z. Anorg. Chem. (1929), vol. 180, pp. 19-41.
6. A. H. Jay, Proc. Phys. Soc. (London) (1933), vol. 45, pp. 635-642.
7. J. E. Dorn and George Glockler, Rev. Sci. Instr. (1936), vol. 7, pp. 389-390.
8. W. Hume-Rothery and P. Reynolds, Proc. Roy. Soc. (London) (1938), vol. 167A, pp. 25-34.
9. F. Schossberger, Z. Krist. (1938), vol. 98, pp. 259-265.
10. E. C. Ellwood, J. Inst. Metals (1940), vol. 66, p. 87.
11. A. J. C. Wilson, Proc. Phys. Soc. (London) (1941), vol. 14, pp. 341-343.
12. H. Esser and H. Eusterbrock, Arch. Eisenhütten (1941), vol. 14, pp. 341-343.
13. E. A. Owen, J. Sci. Instr. (1943), vol. 20, pp. 190-192.
14. M. J. Buerger, N. W. Buerger and F. G. Chesley, Amer. Mineral (1943), vol. 28, pp. 285-302.
15. F. G. Chesley, Rev. Sci. Instr. (1946), vol. 17, p. 558.
16. L. F. Connell, Rev. Sci. Instr. (1947), vol. 18, p. 367.
17. J. W. Edwards, R. Speiser, and H. L. Johnson, Rev. Sci. Instr. (1949), vol. 20, pp. 343-347.

18. J. J. Lander, Rev. Sci. Instr. (1949), vol. 20, pp. 82-83.
19. E. A. Owen, J. Sci. Instr. (1949), vol. 26, pp. 114-117.
20. E. C. Williams, J. Sci. Instr. (1950), vol. 27, pp. 154-157.
21. H. J. Goldschmidt and J. Cunningham, J. Sci. Instr. (1950), vol. 27, pp. 177-182.
22. Tervichiro Kubo and H. Akabori, J. Phys. Colloid. Chem. (1950), vol. 54, p. 112.
23. E. J. Goon, J. T. Mason and T.R.P. Gibb, Jr., Rev. Sci. Instr. (1957), vol. 20, pp. 342-344.
24. W. L. Bond, Rev. Sci. Instr. (1958), vol. 29, pp. 654-655.
25. P. Gordon, J. Appl. Phys. (1949), vol. 20, pp. 908-917.
26. R. Bethold and H. Böhm, Metallwirtschaft (1932), vol. 11, p. 567.
27. R. L. Woolley, J. Sci. Instr. (1948), vol. 25, p. 321.
28. E. G. Steward, J. Sci. Instr. (1949), vol. 26, pp. 371-372.
29. L. S. Dent and H.F.W. Taylor, J. Sci. Instr. (1956), vol. 33, pp. 89-91.
30. A. P. Wangsgard, Trans. Amer. Soc. Metals (1942), vol. 30, p. 1303.
31. L. S. Birks and H. Friedman, Rev. Sci. Instr. (1947), vol. 18, pp. 576-580.
32. A. Van Valkenberg and H. F. McMurdie, Amer. Ceram. Soc. Bull. (1947), vol. 30, p. 139.
33. H. T. Heal and H. Mykura, Metal Treatment (1950), vol. 17, p. 129; Rev. Met. (1951), vol. 48, p. 966.
34. P. Chiotti, Rev. Sci. Instr. (1954), vol. 25, pp. 683-688.
35. L. S. Birks, Rev. Sci. Instr. (1954), vol. 25, pp. 963-966.

36. G. K. Williamson and A. Moore, J. Sci. Instr. (1956), vol. 33, pp. 107-110.
37. S. W. Kennedy and L. D. Calvert, J. Sci. Instr. (1958), vol. 35, pp. 61-62.
38. J. Spreadborough and J. W. Christian, Proc. Phys. Soc. (London) (1959), vol. 74, pp. 609-615.
39. R. L. P. Berry and G. V. Raynor, Research (1953), vol. 6, pp. 21s-23s.
40. W. C. Elmore and M. Sands, Electronics (McGraw-Hill Book Co., 1949), pp. 396-400.
41. B. G. Hogg and H. E. Duckworth, Rev. Sci. Instr. (1948), vol. 19, pp. 331-332.
42. J. W. M. DuMond and H. A. Kirkpatrick, Rev. Sci. Instr. (1930), vol. 1, pp. 88-105.
43. A. R. Lang, Rev. Sci. Instr. (1956), vol. 27, pp. 17-25.
44. B. R. Banergie, Rev. Sci. Instr. (1955), vol. 26, pp. 564-565.
45. H. H. Johann, Z. Physik (1931), vol. 69, pp. 185-206.
46. C. B. Walker, Rev. Sci. Instr. (1954), vol. 25, p. 301.
47. J. W. M. DuMond, D. A. Lind, and E. R. Cohen, Rev. Sci. Instr. (1947), vol. 18, pp. 617-626.
48. J. H. Williams, Phys. Rev. (1934), vol. 45, pp. 71-75.
49. R. Hofstadter, Phys. Rev. (1948), vol. 74, pp. 100-101.
50. H. I. West, Jr., W. E. Meyerhof, and R. Hofstadter, Phys. Rev. (1951), vol. 81, pp. 141-142.

51. J. Taylor and W. Parrish, Rev. Sci. Instr. (1955), vol. 26, pp. 367-373.
52. W. Parrish and T. R. Kohler, Rev. Sci. Instr. (1956), vol. 27, pp. 795-808.
53. M. V. Cohen, Rev. Sci. Instr. (1935), vol. 6, pp. 68-74.
54. L. Alexander and H. P. Klug, J. Appl. Phys. (1950), vol. 21, pp. 137-142.
55. R. C. Spencer, Phys. Rev. (1931), vol. 38, pp. 630-641.
56. N.F.M. Henry, H. Lipson, and W.A. Wooster, Interpretation of X-ray Diffraction Photographs (London: Macmillan and Co. Ltd., 1951) p. 29.
57. L. Alexander, J. Appl. Phys. (1950), vol. 21, pp. 126-136.
58. L. Alexander, J. Appl. Phys. (1954), vol. 25, pp. 155-161.
59. J. N. Eastabrook, Br. J. Appl. Phys. (1952), vol. 3, pp. 349-352.
60. R. C. Spencer, Phys. Rev. (1939), vol. 55, p. 239; J. Appl. Phys. (1949), vol. 20, pp. 413-414.
61. A.J.C. Wilson, J. Sci. Instr. (1950), vol. 27, pp. 321-325.
62. U.W. Arndt, X-Ray Diffraction by Polycrystalline Materials, editor, H. F. Pelsler, H. P. Rooksby and A.J.C. Wilson (Inst. of Phys. London, 1955), Chap. 7.
63. A.J.C. Wilson, Proc. Cam. Phil. Soc. (1940), vol. 36, pp. 485-489.
64. W. T. Sproull, X-Rays in Practice (McGraw-Hill Book Co., 1946) p. 98.

65. E. A. Owen and E. W. Roberts, Phil. Mag. (1939), vol. 27, pp. 294-327.
66. H. Esser, W. Eilender and K. Bungardt, Arch. Eisenhütten (1938), vol. 12, p. 157.
67. W. Hume-Rothery and P. W. Reynolds, Proc. Roy. Soc. (1938), vol. A167, p. 25.
68. H. T. Clark, J. Metals (1949), vol. 1, 588-589.
69. E. S. Greiner and W. C. Ellis, Trans. AIME (1949), vol. 180, pp. 257-665.
70. I. Szántó, Acta Tech. Acad. Sci. Hung. (1955), vol. 13, pp. 363-370.
71. M. Born and J. R. Oppenheimer, Ann. Physik (1927), vol. 84, p. 457.
72. R. C. Tolman, The Principles of Statistical Mechanics (Oxford Press, 1938), p. 567.
73. A. Einstein, Ann. Physik (1911), vol. 34, pp. 170-174.
74. M. Born and T. von Kármán, Phys. Zeits. (1912), vol. 13, pp. 297-309; Phys. Zeits. (1913), vol. 14, pp. 15-19.
75. P. Debye, Ann. Physik (1912), vol. 39, pp. 789-839.
76. Landolt-Bornstein Tables (Springer-Verlag, 1927) V.1 (Suppl.) pp. 702-707.
77. A. H. Wilson, Theory of Metals (Cambridge University Press, 1953), p. 144.
78. F. Seitz, The Modern Theory of Solids (McGraw-Hill Book Co., 1940), p. 3.
79. N. M. Wolcott, Phil. Mag. (1957), vol. 2, pp. 1246-1254.
80. H. Jones, Proc. Roy. Soc. (1934), vol. A147, pp. 396-417.
81. J. B. Goodenough, Phys. Rev. (1953), vol. 89, pp. 282-294.

82. C. F. Squire and A. R. Kaufman, J. Chem. Phys. (1941), vol. 9, pp. 673-677.
83. J. L. Wyatt, J. Metals (1953), vol. 5, pp. 903-905.
84. V. Weisskopf, Am. J. Phys. (1943), vol. 11, pp. 1-12.
85. E. Gruneisen, Ann. Physik (1933), vol. 16, pp. 530-540.
86. L. D. Landau and E. M. Lifshitz, Statistical Physics (Pergamon Press Ltd., 1958), p. 153.

APPENDIX
WORM GEAR CALIBRATION

The experimental procedure for worm gear calibration requires the use of two worm gears - one of which can be a dummy gear. The gears rotate about two axes which are almost coincident. As both gears rotate in the same direction, the relative angular motion between the gears depends upon the difference of the sum of the cumulative errors in each gear. This relative rotation can be measured very accurately by the changing fringe pattern between optical flats attached to each gear or by a comparison autocollimator and a mirror attached to each gear. The optical flats technique is probably a bit too sensitive, and a relative rotation about an axis other than the one being investigated would make the fringe pattern very complicated. On the other hand, comparison autocollimators can be obtained which will measure relative rotation about a given axis with an accuracy of 0.1 of a second of arc. After measuring the relative rotation of the two gears, one gear is rotated with respect to the other gear a fixed amount, and the experiment repeated. The analysis of the experimental results follows.

Consider two worm wheels with n teeth in each gear. A worm is engaged in each gear capable of going exactly one revolution, which causes the worm gear to rotate an angle of $2\pi/n$ plus a correction. Let ${}^1\epsilon_1$ be the angular correction to be added to $2\pi/n$ when Gear 1 rotates from tooth 1 to tooth 2; ${}^1\epsilon_2$ the correction when Gear 1 rotates from tooth 2 to tooth 3, etc. The notation ${}^2\epsilon_1$ corresponds to the error in Gear 2 when Gear 2 rotates from tooth i to tooth $i+1$. When the worm

has gone through n revolutions, the worm gear must be back to its original position. Therefore

$$\sum_{i=1}^n 1\xi_i = \sum_{i=1}^n 2\xi_i = 0 \quad (\text{A. 1})$$

After j revolutions of the worm, the rotation of the worm wheels are

$$1\theta_2 = j \frac{2\pi}{n} + \sum_{i=1}^j 1\xi_i \quad (\text{A. 2})$$

$$2\theta_2 = j \frac{2\pi}{n} + \sum_{i=1}^j 2\xi_i \quad (\text{A. 3})$$

The quantity that is measured is the relative cumulative error ${}^o\eta_j$.

$${}^o\eta_j = 1\theta_j - 2\theta_j \quad (\text{A. 4})$$

or,

$${}^o\eta_j = \sum_{i=1}^j (1\xi_i - 2\xi_i) \quad (\text{A. 5})$$

Now

$$1\xi_j - 2\xi_j = [1\theta_j - 2\theta_j] - [1\theta_{j-1} - 2\theta_{j-1}] \quad (\text{A. 6})$$

Using equation A. 4, equation A. 6 becomes

$$1\xi_j - 2\xi_j = {}^o\eta_j - {}^o\eta_{j-1} \quad j \leq n-1 \quad (\text{A. 7})$$

If Gear 2 is rotated in the direction of decreasing j by k revolutions of its worm, while leaving Gear 1 stationary and the above procedure

repeated, the following expressions are obtained:

$${}^1\theta_j = j \frac{2\pi}{n} + \sum_{i=1}^j {}^1\xi_i$$

$${}^2\theta_j = j \frac{2\pi}{n} + \sum_{i=k+1}^{j+k} {}^2\xi_i$$

$${}^1\theta_j - {}^2\theta_j = k\eta_j$$

and

$${}^1\xi_j - {}^2\xi_{j+k} = k\eta_j - k\eta_{j-1} \quad j \leq n-1 \quad (\text{A.8})$$

There are $2n$ unknowns. In equation A.7 and A.8, j cannot be equal to n , since this is the same position as the starting point. Therefore, there are $2(n-1)$ linear equations from equations A.7 and A.8, and two linear equations from equation A.1, giving a total of $2n$ simultaneous linear equations to be solved. The equations are rewritten as

$$\sum_{i=1}^n {}^1\xi_j = 0$$

$$\sum_{i=1}^n {}^2\xi_j = 0$$

$${}^1\xi_j - {}^2\xi_j = \circ\eta_j(1-\delta_{jn}) - \circ\eta_{j-1}(1-\delta_{j1})$$

$${}^1\xi_j - {}^2\xi_{j+k} = k\eta_j(1-\delta_{jn}) - k\eta_{j-1}(1-\delta_{j1})$$

In the above equations δ_{jn} is the Kronecker delta. If k is chosen equal to 1, the above set of simultaneous linear equations can be solved by deduction. The solutions are

$$\begin{aligned}
 {}^1\xi_j &= {}_0\eta_j (1 - \delta_{jn}) - {}_1\eta_{j-1} (1 - \delta_{j1}) - \frac{1}{n} \sum_{i=1}^{n-1} ({}_0\eta_i - {}_1\eta_i) \\
 {}^2\xi_j &= ({}_0\eta_{j-1} - {}_1\eta_{j-1}) (1 - \delta_{j1}) - \frac{1}{n} \sum_{i=1}^{n-1} ({}_0\eta_i - {}_1\eta_i) \quad (A.9)
 \end{aligned}$$

There are various alternatives that can be made on the experimental procedure which are essentially subject to the same analysis. For instance, just one mirror can be attached to the dummy worm gear which is driven by a worm attached to the main worm gear and rotated in a direction opposite to that of the main worm gear. Then the η_j are measured relative to a stationary mirror with a comparison autocollimator. The same equations A.9 apply, but the values of j increase in opposite directions on the two gears.

Another procedure is to use three mirrors and two comparison autocollimators as shown in Figure 43. First, Mirror 2 is adjusted approximately parallel to Mirror 1. The angle read on the comparison autocollimator No. 1 is taken as its zero position. Then the main worm gear is rotated through an angle of $\alpha_1 = \frac{2\pi}{n} + \xi_1$. Mirror 3 is then adjusted approximately parallel to Mirror 1. The angle read on the comparison autocollimator No. 2 is taken as its zero position. Mirrors 2 and 3 are not moved again. The dummy gear is then rotated opposite to the direction of rotation of the main worm gear until the angle between

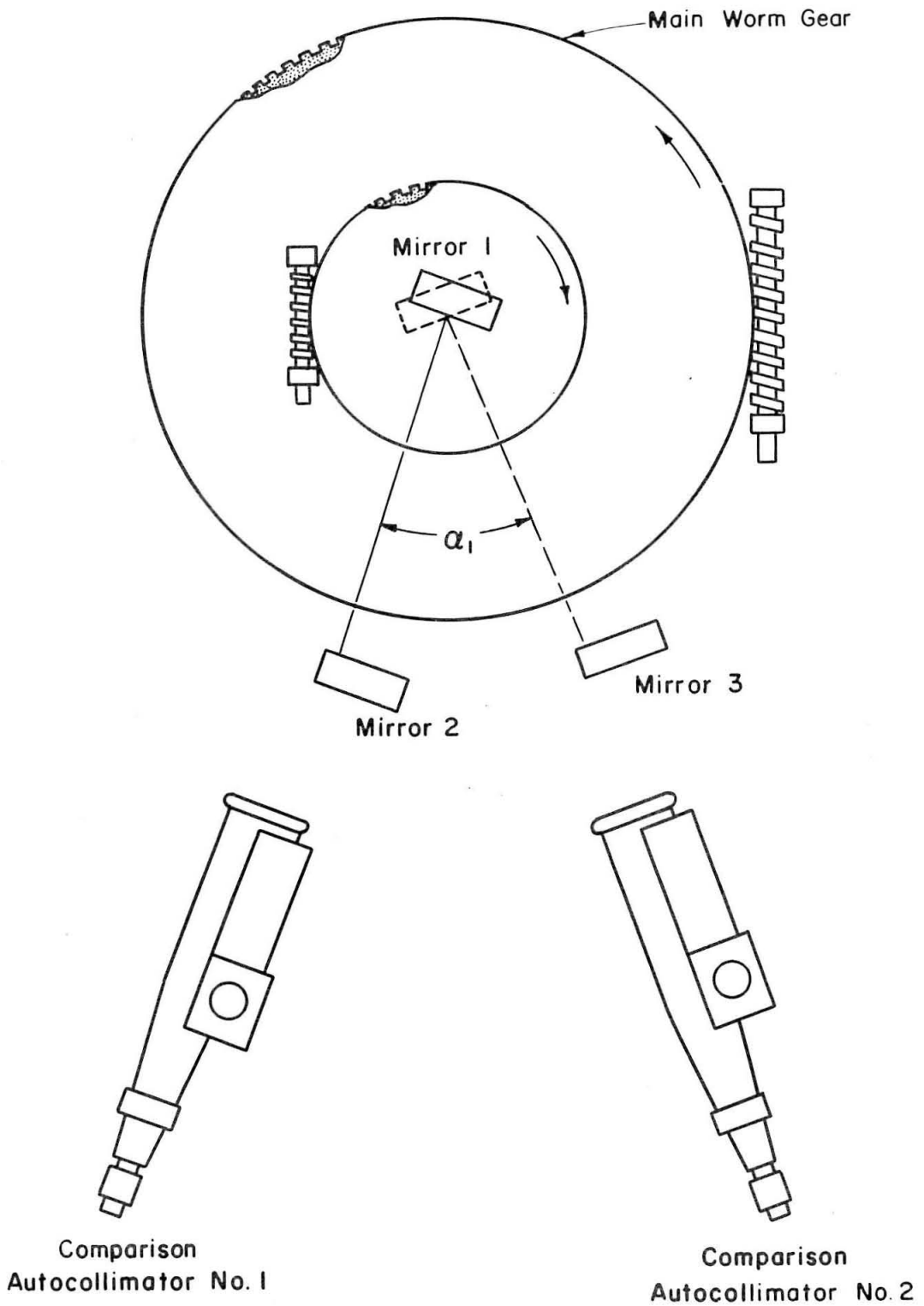


Figure 43.

Mirrors 1 and 2 correspond to the zero position of autocollimator No.

1. The main worm gear is again rotated through an angle $\alpha_2 = \frac{2\pi}{n} + \xi_2$.

The value η_2 is read on autocollimator No. 2 as the angle of deviation from its zero position. The procedure is repeated again and again until the main worm gear goes through a complete revolution.

The value of any η_j is

$$\eta_j = \alpha_j - \alpha_1 \quad (\text{A.10})$$

or

$$\eta_j = \xi_j - \xi_1 \quad 2 \leq j \leq n \quad (\text{A.11})$$

The equation A.11 and the equation

$$\sum_{j=1}^n \xi_j = 0$$

represent n simultaneous linear equations. The solutions to these equations are

$$\xi_j = \eta_j - \frac{1}{n} \sum_{j=2}^n \eta_j \quad j \neq 1$$

$$\xi_1 = -\frac{1}{n} \sum_{j=2}^n \eta_j \quad (\text{A.12})$$